

# Study of the Structure of Light, Unstable Nuclei and the Mechanism of Elastic Proton Scattering

E. T. Ibraeva<sup>a</sup>, M. A. Zhusupov<sup>b</sup>, O. Imambekov<sup>b</sup>, and S. K. Sakhiev<sup>c</sup>

<sup>a</sup>*Institute of Nuclear Physics, National Nuclear Center of the Republic of Kazakhstan, Almaty, Kazakhstan*

<sup>b</sup>*Al-Farabi Kazakh National University, Almaty, Kazakhstan*

<sup>c</sup>*Gumilev Euro-Asian National University, Astana, Kazakhstan*

**Abstract**—The review presents calculations of elastic  $p^6\text{He}$ -,  $p^8\text{Li}$ -,  $p^9\text{Li}$ - and  $p^9\text{C}$  scattering in the framework of the Glauber theory of multiple diffraction scattering at intermediate energies of 70 and 700 MeV/nucleon. The most significant result of the calculations is that we have utilized realistic three-body wave functions obtained within modern nuclear models. The relation is found between differential cross sections and inter-cluster potentials, where the nuclear wave functions are calculated. Conclusions are made concerning the types of potentials which describe most realistically the available experimental data. The method for calculation of three-body wave functions in  $\alpha$ - $n$ - $n$ -,  $\alpha$ - $t$ - $n$ -,  $^7\text{Be}$ - $p$ - $p$ -,  $\alpha$ - $t$ - $2n$ -, and  $^7\text{Li}$ - $n$ - $n$  models is described with discussion of inter-cluster potentials and the quantum-number configurations taken into consideration. It is revealed how the wave functions and the nuclear electromagnetic characteristics calculated using these wave functions depend on the choice of intercluster potentials. The derivation of matrix elements (amplitudes) of  $pA$  scattering in the framework of the Glauber approach with three-body wave functions is presented by an example of  $^6\text{He}$  nucleus. Discussing the results of calculation of differential cross sections and the analyzing power ( $A_y$ ), we established how the calculated characteristics depend on a wave-function structure and dynamics of the process determined by a Glauber operator of multiple scattering. The calculated differential cross sections and analyzing powers are compared with available experimental data and calculations by other authors performed for different formalisms, which allows us to make justified conclusions.

DOI: 10.1134/S1063779611060037

## INTRODUCTION

Discovery of exotic (neutron- or proton-excess) nuclei has posed fundamental problems to nuclear physics in relation to determination of nucleon drip line, evolution of nuclear shells, explanation of new structural formations (halo), and synthesis of super-heavy elements at accelerators and space objects.

These radioactive (unstable in  $\beta$ - and other decay channels) nuclei have been in great demand for recent decades (since 1985 [1–4]) and are widely studied in many research centers in Russia (Nuclotron, FLNR, JINR, Dubna), the United States (NSCL, MSU Michigan, ORNL Berkeley), Canada (TRIUMF, Vancouver), Germany (GSI, Darmstadt), France (SPIRAL, GANIL, SATURN-II, Saclay), CERN (ISOLDE, SPS.), Japan (SBL, RIKEN), Brazil (FSU, RIBRA, Sao Paulo), etc.

Evidence of the steady interest in exotic nuclei includes the design and construction of new facilities for studying them. The huge accelerator complex FAIR (Facility for Antiproton and Ion Research) in Darmstadt (GSI) has already been approved (with construction beginning in 2010) with heavy ion synchrotron (HIS) SIS100 [5], which will be the basic facility necessary for a complex of research programs including the electron-ion collider in the intersecting

beams ELISE (Electron-Ion Scattering) and production of exotic nuclei induced in light-ion reactions (EXL). The projects SCRIT RIBF (Self Confining Radioactive Isotope Target at Radioactive Isotopes Beam Factory) in RIKEN, Japan [6], ISF MSU (Isotope Science Facility at Michigan State University) in the United States [7], and SPIRAL-2 GANIL in France [8] are at different stages of decision-making; the construction of a new fragment separator ACCULINNA-2 at JINR (Dubna) is under discussion. At these facilities, radioactive nuclear beams with large intensity shall be obtained for use in nuclear reactions and the first electron-nuclear experiments with unstable nuclei will be carried out, making it possible to supplement and refine the data on their properties with experiments studying the scattering of proton and nuclear targets.

Currently, nucleon-stable isotopes are obtained, in which the number of neutrons is more than twice as many as the number of protons; these are  $^{40}\text{Mg}$  (12 protons and 28 neutrons) and  $^{42}\text{Al}$  (13 protons and 29 neutrons) [9]. The availability of these isotopes expands the boundary of neutron stability. Exotic nuclei play an important and sometimes dominant role in many phenomena observed in space, such as new stars, supernovas,  $\gamma$  flares and other astrophysical phenomena. It has been shown recently [10] that the

formation of the ultra neutron-excess and superheavy nuclei is possible in relativistic jets,  $\gamma$  flares, and supernova jets near the neutron star in the process of its birth. The sources creating these nuclei are nuclear reactions and reactions of synthesis in space objects.

Experimental data on nuclei near the nucleon drip line is extracted from the elastic and inelastic scattering of nuclei by the proton and heavier targets, as well as from the reactions of one- and many-nucleon transfers and Coulomb dissociation (breakup) of a light, unstable nucleus in the field of a heavier one. The most comprehensive information is gathered for integral observables such as total cross sections of elastic and inelastic scattering, reactions, and breakup. There are data on differential cross sections (DCS), angular and momentum distributions of fragments, and excitation spectra of reaction products. New experiments are aimed at measuring the polarization observables as well as at measuring different correlations (energetic, angular, and combined ones) in motion of fragments during the exotic-nuclei breakup. Kinematically complete experiments, where all fragments are recorded simultaneously and which contain the most exhaustive information on the nuclear structure and interaction dynamics, are needed for these measurements. However, detecting a large number of fragments in the kinematically complete experiments is difficult due to the (currently) low intensity of radioactive beams; therefore, there is an urgent need for constructing new facilities with the higher beam intensity.

Data on the reaction total cross sections, the interaction and charge-exchange cross sections of light and intermediate (from  ${}^4\text{He}$  to  ${}^{32}\text{Mg}$ ) exotic nuclei in their interaction with protons and the heavier targets (Be, C, Al), measured and calculated using different methods before 2000, were reviewed in [11, 12]. There, the theoretical models for calculation of these quantities are described (that of strong absorption, the macroscopic and semimicroscopic optical models, and the Glauber model). The analysis of sizes of unstable nuclei, their derivation from the measured total cross sections of interaction and reactions, as well as the effective density distributions of protons and neutrons, and the determination of the neutron skin thickness and core sizes were performed in [12].

Once Tanihata discovered the anomalously large cross section of  $p$ - ${}^{11}\text{Li}$  scattering and drawn the subsequent conclusion about the halo-like structure of  ${}^{11}\text{Li}$  nucleus [1–4], the search for nuclei with the similar structure was pursued rather intensively. However, not all neutron- and proton-excess nuclei have the halo structure. For some of them, the excess of the nucleons does not lead to the anomalous increase in sizes, only to the concentration of excess nucleons in the nucleus surface layer, which is termed “skin” (we shall call the skin-nuclei by analogy of halo-nuclei because the Russian translation of “fur coat” is related to the fur coat of virtual  $\pi$  mesons around the nucleons, while

the term “skin” is not commonly-used). The halo is the low-density distribution of valence nucleons at a certain (on the order of 0.5–0.9 fm) adequate distance from the dense (frequently  $\alpha$ -particle) core of a nucleus. The skin is the excess concentration of a single type of nucleons (neutrons or protons) in the surface region of a nucleus without substantial increase in its size. By definition [12] the skin describes the neutron (or proton) excess on the nuclear surface, while the halo describes the same excess, plus the tail from the neutron (or proton) density.

Three reviews [13–15] on neutron excess isotopes of light elements are written with somewhat different, experimental bias. The first one [13] considers methods for producing radioactive nuclei, the mechanisms of several-nucleon transfer reactions, and the feasibilities of studying the exotic nucleus structure in reactions with radioactive beams. The remaining reviews contain the accumulated experimental data that mainly include the energy spectra of neutron excess nuclei produced in transfer reactions to  $Z \leq 5$  (He, Li, Be, B) [14] and  $Z \geq 6$  (heavy isotopes of C, N, O, F, Ne) [15]. Based on the nuclear energy spectra measured and calculated using different models, conclusions are drawn about their properties. Information available by the time of writing was collected and analyzed.

The latest data on the total cross sections of exotic nuclear reactions (from He to C) during their collisions with heavy targets (Pb, U), the binding energies, and the rms charge radii, calculated in the context of Glauber formalism, are published in [16]. The densities of the standard relativistic mean field (RMF) or the densities obtained in RMF with effective Lagrangian (E-RMF) were used as input parameters. Additionally, the comparison of the calculated values is given with new experimental data for light nuclei (from  ${}^4\text{He}$  to  ${}^{11}\text{Li}$ ) [17–20] with the earlier-measured data for the heavier nuclei (up to Pb, U) [21].

The breakup reactions of  ${}^6\text{He}$  and  ${}^{11}\text{Li}$  nuclei with a two-neutron halo, in their collisions with electrons, protons, and with  ${}^{12}\text{C}$  and  ${}^{208}\text{Pb}$  nuclei were studied in detail in [22]. The calculation of nucleon densities in nuclei was performed within the microscopic multi-particle model based on hyperspherical functions, which made it possible to consistently describe the structure peculiarities of  ${}^6\text{He}$  and  ${}^{11}\text{Li}$  nuclei, in both the ground and excited states, as well as in the continuous spectrum. Cross sections, excitation spectra, momentum distribution of residuals, the energy and angular correlations of breakup fragments, and charge form factors were calculated for different mechanisms of breakup reactions: Coulomb and nuclear reactions, their combination, and the elastic and inelastic fragmentation. The microscopic four-body method in the context of the distorted wave Born approximation (DWBA), used for the calculations, allows one to consistently consider the Coulomb and nuclear dissociations, and the Coulomb-nuclear interference, as well

as recoil effects in the breakup of light nuclei. The developed calculation method may also be applied to the analysis of observables in kinematically complete experiments where various correlations in motion of fragments are measured for the extraction of data on the nuclear structure and the nature of continuous spectrum of excitations.

We shall dwell briefly on the review of models in which the nuclear structure is calculated; it is necessary for the further discussion and comparison of the results obtained from different models. For light nuclei, these are the shell model [23] and its modern modifications: the large-scale shell model (LSSM) without a core [24–27] and the cluster-orbital shell model approximation (COSMA) [28–31]; potential cluster model [32–35]; model of antisymmetrized molecular dynamics (AMD) [36–38]; different microscopic models in which the effective or free  $NN$  interactions are specified, e.g., the resonating group model (RGM) [39–44] and its approximate methods (generator coordinate method (GCM) [45] and variation stochastic method [46–52]), which simplify solving of RGM equations.

The nuclear-shell model was developed from the reasoning that provides the unified description of empirical data on nuclear systematization and makes it possible to calculate some nuclear characteristics individually for any particular nucleus. The model is based on a suggestion that the interaction of all nucleons in a nucleus with each other averaged as a result of their motion leads to the mean one-body spherically symmetric potential  $V(r)$ . In this self-consistent mean field, nucleons move in independent orbits. The many-body model of shells (MBMS) takes into account the interaction of nucleons with each other in the unfilled shell in addition to the interaction of nucleons with the mean field. These are the so-called residual interactions. The successes of the MBMS in describing the structure of light stable nuclei of  $1p$ -shell ( $A = 6–14$ ) [53] are widely-acknowledged. However, as is noted in [22], “the qualitative picture of the structure of nuclei with halo is different. It is characterized by coexistence of two nuclear subsystems: the core nucleons forming the strongly-bound nucleus and the halo nucleons moving with respect to the center-of-mass of the core and creating a cloud of rarefied nuclear matter around the core. In loosely bound systems, the potential energy of the mean field is almost completely compensated by the kinetic energy of motion of nucleons.” Therefore the standard model of shells needs modification for describing halo-nuclei. The contribution of the great number of shells is taken into consideration within LSSM, e.g., the  $g$ -matrix  $NN$  interaction with the Reid potential (Reid93) is used for  ${}^6\text{He}$  in [24] and the calculation is performed in the full  $(0 + 2 + 4 + 6)\hbar\omega$  model space. This model has an advantage in many calculations because, as compared to others, it yields the realistic exponential

asymptotic behavior of the nuclear wave functions (WFs).

In COSMA, the WFs of the bound-state and continuous spectrum are expanded in the hyperspherical basis, which allows one to calculate the three-body functions by taking into account the antisymmetrization in interchange of neutrons.

There is no initial assumption in AMD on existence of clusters, a WF of the system is described by the linear combination of Slater’s determinants with Gaussian wave packets and is a particular case of the Brink cluster WF, where each cluster is constructed from separate nucleons in the same way as a WF in the fermion molecular dynamics. The calculation of WFs for Li, Be, B, C within AMD revealed large structural changes of these isotopes with an increase in the neutron numbers. The WFs in AMD adequately reproduce the static observables, especially magnetic and electric quadrupole moments, and predict a large deformation of the neutron skin for certain isotopes.

In RGM, the WFs of the system are written as the antisymmetrized product of the subsystem WFs and their relative motion, the latter are found as a result of solving the integral equations. The oscillator or Gaussian functions in the translation-invariant shell model (TISM) serve as basis WFs in description of fragments.

The RGM algebraic version, which is based on the expansion of the WFs of the cluster relative motion into a series in functions of the oscillator basis, is actively used for the description of the structure of light neutron-excess nuclei, and for studying the role of the Pauli exclusion principle in forming WFs of the bound state and continuum for three-cluster systems and nuclear reactions with their participation [43, 44].

In GCM, the effective  $NN$  interactions are specified (phenomenological or self-consistent), which makes it possible to bypass difficulties of calculations with the realistic free  $NN$  interactions. The effective-interaction parameters are fitted to the static characteristics of stable nuclei, which is not necessarily effective for unstable nuclei. In stochastic methods, a WF of the cluster system is decomposed in the nonminimal Gaussian basis with searching for optimal components on the basis of trial-and-error method, which also simplifies solving the RGM equations.

The cluster models are the commonly-accepted method of describing the structure of light nuclei and are widely used in different formalisms. The idea of clusterization consists of the fact that nucleons in nuclei can form the stable associations named clusters which may be approximately considered as structureless particles ( $d$ ,  $t$ ,  ${}^3\text{He}$ ,  $\alpha$ , and others). A relation between the cluster and shell models and the algebraic methods applied in the theory of nuclear reactions are considered in detail in [32]. There, (as early as in the 1960s) the available powerful mathematical apparatus of genealogic expansions, Talmi transformations, generator coordinates (Jacobi’s coordinates), etc. was

successfully applied to description of cluster structures. Using group-theoretical methods, the genealogic coefficients and the reduced widths for clusters (with  $A = 1-4$ ) in TISM were calculated, the generalized Talmi transformations were derived, the technique of matrix element calculation in TISM was developed, which was applied to the description of the nuclear reactions (actual for that time): stripping ( $p, t$ ), ( $t, \alpha$ ), substitution ( $\alpha, d$ ), ( $\alpha, t$ ), quasielastic knockout ( $p, 2p$ ), ( $p, pd$ ), ( $p, p\alpha$ ), ( $\pi^+, 2p$ ) and others on light clusterized nuclei:  ${}^6,7\text{Li}$ ,  ${}^{10}\text{B}$ ,  ${}^{12}\text{C}$ ,  ${}^{14}\text{N}$ . The development of cluster ideas continued in the direction of dynamical forming of clusters, which are present in a nucleus not only in the ground state in the internal motion, but can be in excited states (the so-called de-excitation). In the process of interaction with the incoming particle, the de-excitation is removed and the cluster is formed and emitted in the ground state [33–35]. The consideration for de-excitation of virtual clusters leads to increase in the widths of form factors and an effective number of associations. Further, with account for the interference of two potential amplitudes corresponding to different Young orbital schemes [f], the potential cluster model was applied to the systems  $d + d$ ,  $d + t$ ,  $t + p$ ,  $d + p$  with the nonzero total spin  $S$  and named the supermultiplet potential model (SPM) [54]. The modern analysis of SPM is given in [55]. This potential model that takes into account the Pauli exclusion principle “creates the unified physical picture connecting different available experimental data and makes it possible to form new problems” [55], such as producing the supermultiplet scattering phase shifts and the supermultiplet cluster-interaction potentials on their basis.

The particular (but important) case of clusterization is the  $\alpha$ -clusterization, because  $\alpha$ -particle has the largest binding energy ( $E_{\text{bin}} = 28.3$  MeV) as compared to other light particles. Nuclei with the mass number  $A$ , multiple of four:  ${}^8\text{Be}$ ,  ${}^{12}\text{C}$ ,  ${}^{16}\text{O}$ ,  ${}^{20}\text{Ne}$  and others, can be most naturally treated in this model. The  $\alpha$ -cluster model of light nuclei and its applications are discussed in many works, of which we shall mention [56–58], where the  $\alpha$ -cluster model with projection (or Brink model, in which the antisymmetrization of the many-body WF is taken into account) was applied to the calculation of charge form factors of electron scattering by  ${}^{12}\text{C}$  [56],  ${}^{16}\text{O}$ ,  ${}^{24}\text{Mg}$  and others, up to  ${}^{40}\text{Ca}$  [57, 58] and successfully described the experimental data. The minima of form factors which are not described by a typical  $\alpha$ -cluster model with Gaussian functions are rather exactly reproduced in the Brink model with the symmetrized functions of nucleons up to transferred momenta  $q \sim 3 \text{ f}^{-1}$ . The enhancement of the clusterization is also shown in inelastic scattering (in comparison with the elastic scattering), when the initial nucleus goes into the excited states.

Let us also note the works of the Khar'kov group of theoreticians which has very fruitfully developed the

model ( $\alpha$ -cluster model with variance, in which the relative oscillations of  $\alpha$ -particles in the nucleus are taken into consideration) and applied it to processes of elastic and inelastic scattering of nuclei [59] in the context of Glauber theory of multiple scattering. In recent works [60, 61],  $\alpha$ -cluster model is extended to such nuclei as  ${}^9\text{Be}$ ,  ${}^{13}\text{C}$ ,  ${}^{13}\text{N}$ , under the assumption that they consist of the deformed core with the number of nucleons a multiple of four and one nucleon inside the core. The calculated rms radii and the charge form factors of these nuclei are in a good agreement with experimental values. The DCS and polarized characteristics of elastic scattering of protons by  ${}^4\text{He}$ ,  ${}^9\text{Be}$ ,  ${}^{12,13}\text{C}$ ,  ${}^{13}\text{N}$ ,  ${}^{16}\text{O}$ ,  ${}^{20}\text{Ne}$  nuclei, calculated within the theory of multiple scattering at  $E = 0.5, 0.8, \text{ and } 1.0$  GeV, also demonstrate the agreement with experiment, with  $\alpha$ -particle model with dispersion often providing the better description of the precision polarization characteristics of scattering than it is feasible in the modern, many-body shell model [60]. At present, there are calculations in the  $\alpha$ -cluster model for nuclei, consisting of seven ( ${}^{28}\text{Si}$ ) and thirteen ( ${}^{52}\text{Fe}$ )  $\alpha$ -clusters [62].

New aspects of clusterization (molecular and cluster gas-like states in light unstable nuclei) are studied within AMD [38]. For example, the gas-like and crystalline states of  $\alpha$ -clusters in excited states have been recently suggested for describing the structure of C isotopes. In particular,  $3\alpha$ -gas in  ${}^{12}\text{C}$  in  $0^+$  state attracts a broad interest in connection with the Bose-Einstein condensate in the nuclear system.

With development of computing technology, the numerical methods of solving the few-body equations are improved. At the present time, the WFs have been obtained not only for three- and four-, but also for five- and six-body nuclear systems with realistic  $NN$  interactions, three-body forces and consideration for antisymmetrization for all nucleons [63–66]. The exact microscopic WFs of few-body nuclei are computed using the quantum Monte Carlo method (MCM) [64–66] or obtained from solving Faddeev's equations [67]. The quantum MCM includes the variational MCM and the Monte Carlo Green's Function Method (MCGFM). The Monte Carlo Green's Function Method is a stochastic method systematically improving the WF, found initially using the variational MCM, in which a trial function is constructed with the specified angular momentum, parity and isospin. However, using these WFs in different formalisms is difficult due to their extreme complexity, therefore the alternative methods are developed which combine the necessary accuracy and relative simplicity that makes it possible to use them in particular calculations. These are few-body models of light nuclei with realistic potentials of nucleon–nucleon and nucleon–cluster interactions with consideration for antisymmetrization due to the Pauli exclusion principle, which are calculated using the stochastic variational method [46–52] as expansions in the Gaussian basis,

or using the hyperspherical harmonic method implemented in the COSMA code [28]. These models fruitfully develop the potential cluster model and allow one to describe properties of the ground and low-lying excited states not only for the He, Li, Be, B, and C stable light nuclei, but for their unstable isotopes as well. Thus, in the multicluster dynamical model (MDM), the WFs were constructed for the  ${}^6\text{He}$ ,  ${}^6\text{Li}$  and  ${}^9\text{Be}$  light nuclei [68, 69]. Further, in the antisymmetrized version of MDM [70–73] the method of group-theoretical analysis of contribution of exchange effects arising due to the WF antisymmetrization was developed and the significant progress was achieved in description of both static and dynamic observables (DCS, form factors and polarization characteristics) in processes of the elastic scattering of protons, electrons,  $\pi$ -mesons, the photoabsorption of pions by the  ${}^6\text{Li}$ ,  ${}^6\text{He}$ , and  ${}^9\text{Be}$  nuclei.

The absence of strong-interaction theory and exact solution to few-body problems together with “existence of physical situations in which the interaction dynamics is simplified” [22] leads to development of approximate methods for calculation of the measured quantities and extraction of data on the structure and properties of interacting nuclei, with which we shall mention the coupled channel (CC) method [74], its modern extension for the continuous spectrum (method of coupled channels with continuum discretization (CDCC) [75]), relativistic impulse approximation (RIA) [76], high-energy approximation (HEA) [77–83], optical model (OM) [84–87] with the plane (PWIA) and distorted (DWBA) waves with the optical [84] or folding potential [85–87], and theory of Glauber multiple diffraction scattering [88, 89].

The CC approach and the modified CDCC method are used for multichannel problems for small collision energies. The relativistic impulse approximation is applied at high energies; the HEA is the somewhat simplified Glauber theory variant that is based on eikonal approximation, but does not take into account the expansion of multiple scattering into a series, restricting itself, in essence, to the single scattering alone. The most widely-used are the OM and Glauber theory, which are adapted to calculating the characteristics of reactions with exotic nuclei. Each of these approximations has advantages of its own, and we shall briefly touch upon them in discussion of results when we compare values calculated in different approximations.

The macroscopic OM based on the standard phenomenological optical potential with radial dependence of Woods–Saxon appeared to be of little use for describing the scattering of light, exotic nuclei by stable targets at relatively high energies, as it is shown, e.g., in [90] for elastic  $p^6\text{He}$  scattering at 717 MeV and in [91] for  $p^{11}\text{Li}$  scattering at 800 MeV/nucleon.

New OM modifications use either the phenomenological optical potential [84], based on effective

forces of interaction between clusters and nucleons (different from the shape of the Woods–Saxon potential), or the potential calculated in the double folding model [85–87], the initial parameters of which are the matter distribution densities in the colliding nuclei and the effective  $NN$  interactions. The M3Y forces [92] based on the Paris or Reid–Elliott potential or the alternative JLM forces [93, 94] are typically used as effective  $NN$  forces. The total M3Y interaction has the exchange and direct, isoscalar and isovector components, i.e., takes into account the Pauli Exclusion Principle. The imaginary part of potential is typically introduced phenomenologically. The complex JLM interaction is based on the Brueckner–Hartree–Fock approximation, depends both on energy and density and implicitly takes into account the Pauli Exclusion Principle. It leads to the complex optical potential in double-folding models. Since it has only the central part, the spin–orbit M3Y forces are added to calculate the spin–orbit part of the optical potential. The merit of the folding model is that it directly connects the nuclear density distribution of nucleons with the total cross section of elastic scattering. However, the folding model potential needs in substantial renormalization ( $N_R = 0.6–0.7$  for  ${}^6\text{He}$  and  $N_R = 0.4–0.5$  for  ${}^{11}\text{Li}$ ) [87] in order that it successfully describes the DCS of scattering at relatively low energies (tens MeV/nucleon). In the CDCC method, it was shown [75] that the coupling of the elastic scattering channel with the low-lying channels of decay of the loosely bound channels is responsible for renormalization. When the energy of oncoming particles rises, the effect of coupled-channel breakup typically decreases and the quantity  $N_R$  tends to unity. Thus, through the quantity  $N_R$ , the analysis in the folding model can provide the estimation of the effect of coupled-channel breakup in the elastic channel.

The attractiveness of Glauber formalism [88, 89] is that (1) there are almost no free varied parameters in it (input quantities are parameters of elementary nucleon–nucleon amplitudes, which are extracted from independent experiments, and the WFs calculated with the fixed potentials of intercluster interactions); (2) it allows one to separate the scattering mechanism and nuclear structure and consider the contributions to the observable quantities both from the structure constituents (the simulated WFs) and from the scattering mechanism (determined by the operator of multiple collisions).

Since the Glauber approximation is widely-used and the range of its application increases, it is subjected to various improvements. Let us look upon several examples.

The first example is associated with the expansion of the field of Glauber formalism action which is restricted by the relatively high energies (on the order of hundreds MeV) and small scattering angles. For a correct description of experimental data obtained for

proton scattering in inverse kinematics by the  $^{11}\text{Li}$  and  $^8\text{He}$  [95] halo-nuclei at energies of 62, 68.4, and 74.5 MeV/nucleon (for  $^{11}\text{Li}$ ) and 32, 66, and 72.5 MeV/nucleon (for  $^8\text{He}$ ) and scattering angles up to  $60^\circ$ , the method was used in [96, 97], in which the amplitude is expanded into a series in inverse powers of momentum  $k^{-1}$  along the fixed direction of the mean momentum vector  $(\mathbf{k} + \mathbf{k}')/2$ . The first term of the expansion  $k^0$  coincides with Glauber approximation; the next terms  $k^{-1}, k^{-2}, \dots$  yield corrections to the eikonal, which allows one to extend the initial “classical” approximation for the region of large scattering angles. Upon calculating DCS of the  $p$ - $^{11}\text{Li}$  and  $p$ - $^8\text{He}$  scattering, it was shown that corrections for non-eikonicity decrease insignificantly the cross section at large angles ( $\theta > 40^\circ$ ) and their contribution increases with the increase of both the scattering angle and energy of the scattered particles.

The second example is concerned with the theory extension to the nucleus–nucleus collisions are more complicated than the proton–nucleus ones. Since the major part of experimental data on the structure of neutron-excess nuclei is obtained from nucleus–nucleus collisions, Glauber formalism (in the optical limit approximation when the many-body operator of scattering is substituted for the simple two-body one, taking into account only single collisions) became applied to nucleus–nucleus interactions. A new method of reconstruction of nucleus–nucleus optical potential on the basis of Glauber theory is proposed in [79–82]. Presenting the eikonal phase shift of scattering as the overlap integral of point densities of the incoming nucleus, nucleus-target, and form factor of amplitude of  $NN$  scattering, calculating it and comparing with the phenomenological expression for the phase shift specified with using the optical potential, we may find the parameters of the latter. If we compare the eikonal phase shift with the microscopic phase shift of HEA, then we can obtain the optical potential of HEA. These potentials contain only two fitting parameters normalizing their real and imaginary parts in distinction to other phenomenological and semi-microscopic potentials involving no less than four parameters. Thus, the microscopic optical potential of HEA nucleus–nucleus interaction is obtained, which reconstructs the Glauber amplitude in its optical limit. These potentials are applied to the scattering of the relatively light nuclei ( $^{13}\text{C}$  and  $^{16}\text{O}$ ) by heavy targets ( $^{28}\text{Si}$ ,  $^{54}\text{Fe}$ ,  $^{66}\text{Zn}$ ,  $^{208}\text{Pb}$ , and others) and they showed good agreement with the experimental total and DCS at energies of tens MeV/nucleon [79–82].

The third example of Glauber model modernization is presented in [98]. In this work, DCS and polarization observables are calculated for  $pd$  scattering (vector and tensor analyzing powers of proton and deuteron) at energies of 0.25, 0.44, and 1 GeV, which are compared with the exact Faddeev’s calculation

and with the experiment. The following factors were taken into account in the context of Glauber formalism: (1) spin dependence of  $NN$  amplitudes, (2)  $D$ -wave in deuteron, and (3) isospin dependence of  $NN$  amplitudes, i.e., the contribution of double charge-exchange to  $pd$  scattering. Here the spin and isospin dependences of  $NN$  amplitude are deduced from the modern analysis of phase shifts, while the deuteron WFs are obtained from two alternative models of  $NN$  forces. The modernizations have not touched the fundamentals of the original Glauber theory because it is well known to the authors “at least qualitatively that different corrections to Glauber model tend to reduce each other to a substantial degree, so it is difficult to improve the Glauber model significantly by introducing unilateral corrections” [98]. It found “the surprisingly good agreement” of polarization characteristics calculated in the modified Glauber model, obtained in the exact Faddeev’s calculation, and measured in the experiment in the forward hemisphere at  $|t| \leq 0.04$  (GeV/c) $^2$ . The conclusion of the work is that the modified form of Glauber approximation appears to be competitive as compared to the Faddeev’s calculation and quite exact within the wide angular domain even for such a loosely bound nucleus as deuteron, which is the direct consequence of domination of inelastic processes in the total  $pd$  scattering. Elastic  $nd$  scattering is studied in [99], where the total cross section and DCS are calculated in Glauber and Faddeev’s formalisms at  $E = 100$ – $2000$  MeV and after comparing results the former is preferred.

A question on the relation between the reaction mechanism and the structure of loosely bound nuclei is studied by many authors. An interesting idea is implemented in [100, 101]. Analyzing the  $\alpha^6\text{He}$  elastic scattering at  $E_{l.s.} = 19.6$  MeV, the authors associated the mechanism of reaction proceeding through exchange by dineutron (corresponding to the pole diagram) and independent (with delay) transfer of two neutrons (corresponding to the square diagram) with two different configurations of the  $^6\text{He}$  WF: dineutron and cigar-like. The contribution of the dineutron configuration to the DCS of the  $\alpha^6\text{He}$  elastic scattering leads to the occurrence of maxima at large angles ( $\theta > 60^\circ$ ), the cigar-like configuration makes the contribution to the scattering DCS, which is comparable with that of potential, in the whole angular range. Although the dineutron configuration in the  $^6\text{He}$  WF dominates over the cigar-like one (95% and 5% in the total cross section), contributions of these WF components to the backward angle cross section are comparable in magnitude. Analogous conclusions were made earlier [102–106]. For example, when studying the  $p^3\text{He}$  elastic backward scattering [102, 103], the sequential transfer of unbound  $np$ -pair (in  $^1S_0$  state, i.e., in the same state as in which a dineutron may be) makes the dominating contribution to the cross section at backward angles for all energies rang-

ing from tens of MeV to 1 GeV. When studying the  ${}^6\text{He} + {}^4\text{He}$  process at  $E = 25.1$  MeV/nucleon and the  ${}^1\text{H}({}^6\text{He}, {}^4\text{He}){}^3\text{H}$  process at  $E = 21.6$  MeV/nucleon [104–107], it was found that the dineutron configuration dominated over the cigar-like one and they both make the dominating contribution to DCS at backward angles ( $\theta > 100^\circ$ ) where the potential scattering has the value smaller by several orders of magnitude. Based on the correct determination of the contribution of the four-angle diagram to DCS, it became possible to reconstruct the WFs of the relative motion in the  $\alpha$ - $2n$ ,  $n$ - ${}^5\text{He}$ , and  $n$ - $\alpha$  channels in the ground state of the  ${}^6\text{He}$  nucleus. The distance is calculated between  $\alpha$ -particle and neutron in the cigar-like configuration:  $R_{n\alpha} = 3.8$  fm [100].

The recent measurement of momentum correlations of neutrons in the  ${}^4\text{He}({}^6\text{He}, 2\alpha)2n$  reaction of quasifree scattering of  $\alpha$ -particles, performed at the fragment-separator ACCULINNA at JINR [108], is also in a good agreement with theoretical predictions about the existence of dineutron and cigar-like components in the  ${}^6\text{He}$  nucleus.

The  ${}^6\text{Li}(\gamma, \pi^+){}^6\text{He}$  reactions [73] of charged pions with  $\gamma$ -quanta emission and reactions of transfer of one or two nucleons [101, 104, 105, 109] may serve as the useful additional study of halo structures, because they are also sensitive to the WF of the nucleus that is created in a final state. For example, it was revealed in [101], after the analysis of the  ${}^9\text{Be}(d, p){}^{10}\text{Be}$  reaction cross section, that at scattering angles below  $50^\circ$  the dominating contribution to it comes from the square mechanism of the neutron pick-up and dineutron stripping and the  ${}^{10}\text{Be}$  structure is determined by the core and ill-defined halo from one neutron. The analysis of the  ${}^{10}\text{Be}(t, p){}^{12}\text{B}$  reaction cross section has shown that the main contribution to DCS in all angle range (from 0 to  $160^\circ$ ) comes from the pole mechanism of stripping of the dineutron cluster and the  ${}^{12}\text{B}$  nucleus has halo structures, the excess neutrons form “skin” in the nucleus surface region. Thus, it is revealed that the correct determination of contributions from two mechanisms to cross sections of the  $(d, p)$  and  $(t, p)$  reactions on the  ${}^9\text{Be}$  and  ${}^{10}\text{Be}$  nuclei allows one to find the WF of relative motion  ${}^8\text{Be}-2n$ ,  ${}^{10}\text{B}-2n$ ,  $n_1-{}^8\text{Be}-n_2$ ,  $n_1-{}^{10}\text{B}-n_2$  in the ground state of the  ${}^{10}\text{Be}$ ,  ${}^{12}\text{B}$  nuclei and thus to determine their spatial structure.

This review is aimed at studying the characteristics of elastic scattering of protons by the  ${}^6\text{He}$ ,  ${}^8,9\text{Li}$ , and  ${}^9\text{C}$  nuclei at energies of 0.07 and 0.7 GeV/nucleon in inverse kinematics. Furthermore, we shall place emphasis upon the linkage between the scattering mechanism and nuclear structure, which is particularly urgent for loosely bound halo and skin nuclei.

The review consists of introduction, conclusion and two sections. The first section reviews briefly pub-

lications concerning the latest calculations of few-body WFs of nuclei in question; the method of calculation of three-body WFs is given schematically with the detailed discussion of intercluster potentials and weights of WFs in different configurations (Tables 1, 4–6, 9). The results are presented as densities of WFs and their isolines; the calculated static characteristics are summarized in Tables 2, 3, 4, 5, 7–9 together with the experimental data and calculations from other authors. The second part gives the derivation of matrix elements (amplitudes) of the  $pA$  scattering within Glauber approximation with three-body WFs by example of the  ${}^6\text{He}$  nucleus. Discussing the results of the calculation of cross sections and analyzing powers ( $A_y$ ), we tried to show how the calculated characteristics depend on the WF structure, which in turn is determined by the intercluster-interaction potentials, and upon dynamics of the process defined by Glauber operator of multiple scattering. The performed comparison of the calculated WFs and analyzing powers with the available experimental data and calculations from other authors allowed us to formulate the conclusions.

## 1. WAVE FUNCTIONS AND STATIC CHARACTERISTICS OF ${}^6\text{He}$ , ${}^8,9\text{Li}$ AND ${}^9\text{C}$ NUCLEI IN THREE-BODY MODELS

The multicluster models of light nuclei are successfully applied in calculations of different nuclear characteristics, both static and dynamic ones. The grounds for creating these models were the strong clusterization of light nuclei in some separated channels and the unsatisfactory description of the spectrum and properties for exotic nuclei in alternative models (shell model, collective model, etc.).

In this section we shall touch upon the brief description of the method for calculating WFs of the  ${}^6\text{He}$ ,  ${}^8\text{Li}$ ,  ${}^9\text{C}$ , and  ${}^9\text{Li}$  nuclei in the  $\alpha$ - $n$ - $n$ -,  $\alpha$ - $t$ - $n$ -,  ${}^7\text{Be}$ - $p$ - $p$ -,  $\alpha$ - $t$ - $2n$ -, and  ${}^7\text{Li}$ - $n$ - $n$  models, by means of solving the three-body Schrödinger equation using the stochastic variational method proposed in [46, 47]. A trial function is expanded into a series in the multidimensional nonminimal nonorthogonal basis, and its optimal parameters are found using the trial-and-error method. The stochastic approach has a number of advantages over the standard variational method: the fast convergence; introduction of many radial scales in the basis and the automatic procedure of their search; obtaining trial functions with correct asymptotics, and, in case of using Glauber basis for the WF expansion, the matrix elements of interactions can be calculated analytically, which improves the accuracy of calculations. This approach was modified by introducing the orthogonalizing pseudopotentials, allowing one to exclude contribution of the states, forbidden by the Pauli exclusion principle, to the total WF [68–73] and was successfully applied for studying the structure of nuclei with  $A = 5$  [69], 6 [73], 9 [72].

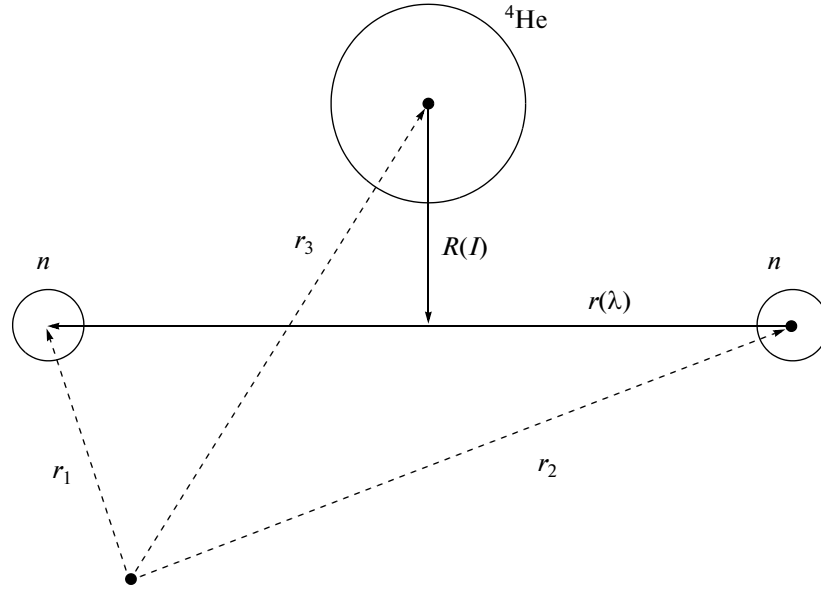


**Fig. 1.** Schematic diagram of the  ${}^6\text{He}$  nucleus in the  $\alpha$ - $n$ - $n$  model with the one-body (dashed lines) and Jacobi (solid lines) coordinates.

For description of a system of interacting clusters in a nucleus in the dynamic multicluster models, a trial function is constructed in the form of a product of internal WFs of clusters with different cluster particles configurations which are connected with intercluster Jacobi coordinates  $\mathbf{r}, \mathbf{R}$ :

$$\Psi_{i,f}^{JM_j} = \Psi_1 \Psi_2 \Psi_3 \Psi^{JM_j}(\mathbf{r}, \mathbf{R}), \quad (1.1)$$

where  $\Psi_1, \Psi_2$ , and  $\Psi_3$  are internal WFs of clusters (which are assumed to be identical to WFs of free particles);  $\Psi^{JM_j}(\mathbf{r}, \mathbf{R})$  is the WF of their relative motion. The subscript 1 denotes  $\alpha$ -particle (in the  $\alpha$ - $n$ - $n$ -,  $\alpha$ - $t$ - $n$ - and  $\alpha$ - $t$ - $2n$  models),  $n$  or  $p$  (in the  ${}^7\text{Li}$ - $n$ - $n$ - and  ${}^7\text{Be}$ - $p$ - $p$  models); subscript 2 designates  $t$  (in  $\alpha$ - $t$ - $n$ - and  $\alpha$ - $t$ - $2n$  models),  $n$  (in the  $\alpha$ - $n$ - $n$ - and  ${}^7\text{Li}$ - $n$ - $n$  models), and  $p$  (in  ${}^7\text{Be}$ - $p$ - $p$  model); subscript 3 stands for  $n$  (in the  $\alpha$ - $n$ - $n$ - and  $\alpha$ - $t$ - $n$  models),  $2n$  (in  $\alpha$ - $t$ - $2n$  model) and  ${}^7\text{Li}$  or  ${}^7\text{Be}$  (in the  ${}^7\text{Li}$ - $n$ - $n$ - and  ${}^7\text{Be}$ - $p$ - $p$  models). The coordinate  $\mathbf{r}$  describes the relative  $\alpha$ - $t$ - (in the  $\alpha$ - $t$ - $n$ - and  $\alpha$ - $t$ - $2n$  models),  $n$ - $n$ - (in the  $\alpha$ - $n$ - $n$ - and  ${}^7\text{Li}$ - $n$ - $n$  models), and  $p$ - $p$ - (in  ${}^7\text{Be}$ - $p$ - $p$  model) motion, it is conjugated by the orbital angular momentum  $\lambda$  with projection  $\mu$ ; the coordinate  $\mathbf{R}$  describes the relative motion between the  $\alpha$ - $t$ - (in the  $\alpha$ - $t$ - $n$ - and  $\alpha$ - $t$ - $2n$  models),  $n$ - $n$ - (in the  $\alpha$ - $n$ - $n$ - and  ${}^7\text{Li}$ - $n$ - $n$  models) and  $p$ - $p$ - (in  ${}^7\text{Be}$ - $p$ - $p$  model) centers of masses and the remaining cluster ( $\alpha$ ,  $n$ ,  $2n$ ,  ${}^7\text{Li}$ ,  ${}^7\text{Be}$ ), it is conjugated by the orbital momentum  $l$  with projection  $m$ . Schematic representation of the  ${}^6\text{He}$  nucleus with the one-body and Jacobi coordinates is presented in Fig. 1.

The WF of relative motion is expanded into a series in partial waves:

$$\Psi^{JM_j}(\mathbf{r}, \mathbf{R}) = \sum_{\lambda l S} \Psi_{\lambda l S}^{JM_j}(\mathbf{r}, \mathbf{R}). \quad (1.2)$$

Each partial function is factorized in the radial and spin-angular parts:

$$\Psi_{\lambda l S}^{JM_j}(\mathbf{r}, \mathbf{R}) = \Phi_{\lambda l}(r, R) F_{\lambda l S}^{JM_j}(\mathbf{r}, \mathbf{R}). \quad (1.3)$$

The WF radial part is approximated with linear combinations of Gaussian functions:

$$\Phi_{\lambda l}(r, R) = r^\lambda R^l \sum_{ij} C_{ij}^{\lambda l} \exp(-\alpha_i r^2 - \beta_j R^2). \quad (1.4)$$

Weights of the  $C_{ij}^{\lambda l}$  components are found as a result of numerical solving of the Schrödinger equation using the variational method, the  $\alpha_i, \beta_j$  coefficients are specified on the tangential grid, the initial parameters of which  $\alpha_0, \beta_0$  are varied for better reaching the energy minimum, corresponding to the nucleus ground state. The WF spin-angular part

$$F_{\lambda l S}^{JM_j}(\mathbf{r}, \mathbf{R}) = \sum_{M_L M_S \mu m} \langle \lambda \mu l m | L M_L \rangle \langle L M_L S M_S | J M_j \rangle \times Y_{\lambda \mu}(\mathbf{r}) Y_{l m}(\mathbf{R}) \chi_{S M_S} \quad (1.5)$$

is the product of Clebsch–Gordan coefficients, determining the scheme of summing the angular momenta ( $L, M_L, S, M_S, J, M_j$  are the orbital, spin, and total nuclear angular momenta and their projections), by

the spherical functions  $Y_{\lambda\mu}(\mathbf{r})$ ,  $Y_{lm}(\mathbf{R})$  and the spin function

$$\chi_{SM_S} = \sum_{m_1 m_2} \langle s_1 m_1 s_2 m_2 | SM_S \rangle \chi_{s_1 m_1} \chi_{s_2 m_2}, \quad (1.6)$$

where  $\chi_{s_1 m_1}$ ,  $\chi_{s_2 m_2}$  are the internal spin WFs of the valence particles.

The main problem of the WF calculation is a choice of intercluster-interaction potentials, because they are input parameters of the calculation and the WF quality (i.e., how exactly the static characteristics obtained using these WFs will be appropriate to the experimental data) depends on them.

### 1.1. The Wave Function of the ${}^6\text{He}$ Nucleus

The reason for the  $\alpha$ - $n$ - $n$  model of the  ${}^6\text{He}$  nucleus is as follows: (i) a small binding energy in the  $\alpha$ - $2n$  channel, which is only equal to  $E_{\alpha-2n} = 0.973$  MeV (for comparison  $E_{t-t} = 12.3$  MeV,  $E_{t-dn} = 18.6$  MeV), (ii) the spectroscopic factor of this channel close to 1 ( $S_{\alpha-2n} \sim 1$ ) [109], and also (iii) the measurement of DCS of high-energy  ${}^6\text{He}$  scattering by light nuclei; from this the incontestable proofs are derived for its well-defined clusterization to the  $\alpha$ -particle core and the two-neutron halo (or skin) [94, 110–113]. The question of whether the  ${}^6\text{He}$  nucleus structure is reduced to the  $\alpha$ - $n$ - $n$ -configuration alone is discussed in many works, of which we shall mention the latest ones [108, 109]. In [109], the cluster structure of the  ${}^6\text{He}$  ground state in the  $\alpha$ - $2n$  and  $t$ - $t$  channels is investigated in the  ${}^6\text{He}(p, t)$   ${}^4\text{He}$  transfer reaction at  $E = 25$  MeV/nucleon. The experimental data are analyzed in DWBA and with the use of the CDCC method, including the direct transfer of two neutrons and a triton and the sequential transfer of a triton ( $t = 2n + p$ ). The reaction DCS data at backward angles are reconstructed only with the spectroscopic factor  $S_{t-t} = 0.08$ , which is much less than it was theoretically predicted earlier (e.g.,  $S_{t-t} = 0.44$  in [114]). The  ${}^4\text{He}({}^6\text{He}, t\alpha)t$  and  ${}^4\text{He}({}^6\text{He}, t\alpha)dn$  reactions of quasifree scattering at  $E = 25$  MeV/nucleon at the fragment separator ACCULINNA at JINR are studied in [108]. The experimental data processing was conducted in PWIA. The effective numbers are obtained for tritons in the  $t$ - $t$  ( $N_{tt} = 0.06$ ) and  $t$ - $d$ - $n$  ( $N_{tdn} = 0.18$ ) channels. Their comparison testifies to the dominating weight of the latter configuration. The effective number of  $\alpha$ -particles, measured in the  ${}^4\text{He}({}^6\text{He}, 2\alpha)2n$  reaction in the whole energy range is equal to  $N_\alpha = 0.03$ , which is fairly small and is somewhat doubted.

We use the WFs of  ${}^6\text{He}$  nucleus obtained in [68, 71] in the three-body  $\alpha$ - $n$ - $n$  model. It supposes the inert  $\alpha$ -particle core, but completely takes into account all interactions of two valence neutrons between each other and with the core. The intercluster interaction potentials, and the considered WF configurations and

**Table 1.** The interaction potentials and the considered configurations of WFs of the  ${}^6\text{He}$  nucleus in the  $\alpha$ - $n$ - $n$  model

Potential	Model 1 [68]	Model 2 [71]
$\alpha$ - $n$	Saka–Biedenharn–Breit (SBB) [115]	Deep, with FS, split in parity of orbital angular momentum
$n$ - $n$	Reid with soft core (RSC) [116]	RSC [116]
Configuration	Configuration weight ( $P$ )	
$\lambda$ $l$ $L$ $S$		
0 0 0 0	0.957	0.869
1 1 1 1	0.043	0.298

their weights are presented in Table 1. The Saka–Biedenharn–Breit (SBB) potential [115] of Gaussian shape and the deep attracting potential with even-odd splitting of phase shifts [71] were used as  $\alpha$ - $n$ -potential. This is an improved  $\alpha$ - $n$ -potential, taking into account the Pauli Exclusion Principle more adequately and reconstructing the data on scattering the waves with the low orbital angular momentum ( $L < 3$ ). It contains the exchange Majorana component both in the central and spin-orbit terms, which leads to the even-odd splitting of phase shifts. The even-odd splitting by the orbital angular momentum approximately takes into consideration the exchange effects in the pair potential. The Reid potential with soft core (RSC) [116] was chosen as  $n$ - $n$ -potential. As a whole, the calculations showed the weak sensitivity of the results to parameters of the  $n$ - $n$ -potential.

The WF configuration is determined by combination of quantum numbers  $\lambda/l/L/S$ , where  $l$  is the angular momentum of relative motion of  $\alpha$ -particle and center-of-mass of two neutrons,  $\lambda$  is the angular momentum of relative motion of two neutrons,  $L$  and  $S$  are the total orbital and spin angular momenta of a nucleus. Since the total spin of two valence nucleons can be only 0 or 1, the condition  $L = S$  imposes a constraint on the ground-state WFs to the  $S$ - and  $P$ -configurations:  $\lambda = l = L = 0$ ,  $S = 0$  ( $S$ -wave) and  $\lambda = l = L = 1$ ,  $S = 1$  ( $P$ -wave).

On the basis of Eqs. (1.1) and (1.2), we write down the WF of the  ${}^6\text{He}$  nucleus with the total angular momentum  $J$  (for the ground state  $J^\pi = 0^+$ ,  $S = 0$ ) and its projection  $M_J$  in the  $\alpha$ - $n$ - $n$  model:

$$\Psi_{i,f}^{JM_J} = \Psi_\alpha(\mathbf{R}_\alpha) \varphi_{n1}(\mathbf{r}_1) \varphi_{n2}(\mathbf{r}_2) \sum_{\lambda l L S} \Psi_{\lambda l L S}^{JM_J}(\mathbf{r}, \mathbf{R}), \quad (1.7)$$

where  $\Psi_\alpha(\mathbf{R}_\alpha)$ ,  $\varphi_{n1,2}(\mathbf{r}_{1,2})$ ,  $\Psi_{\lambda l L S}^{JM_J}(\mathbf{r}, \mathbf{R})$  are the WFs of  $\alpha$ -particle, neutron ( $n$ ) and relative motion in the Jacobi coordinates.

The weights of the  ${}^6\text{He}$  nucleus configurations are given in Table 1. There we can be seen that the maximal contribution in the  $\alpha$ - $n$ - $n$  model is made up of

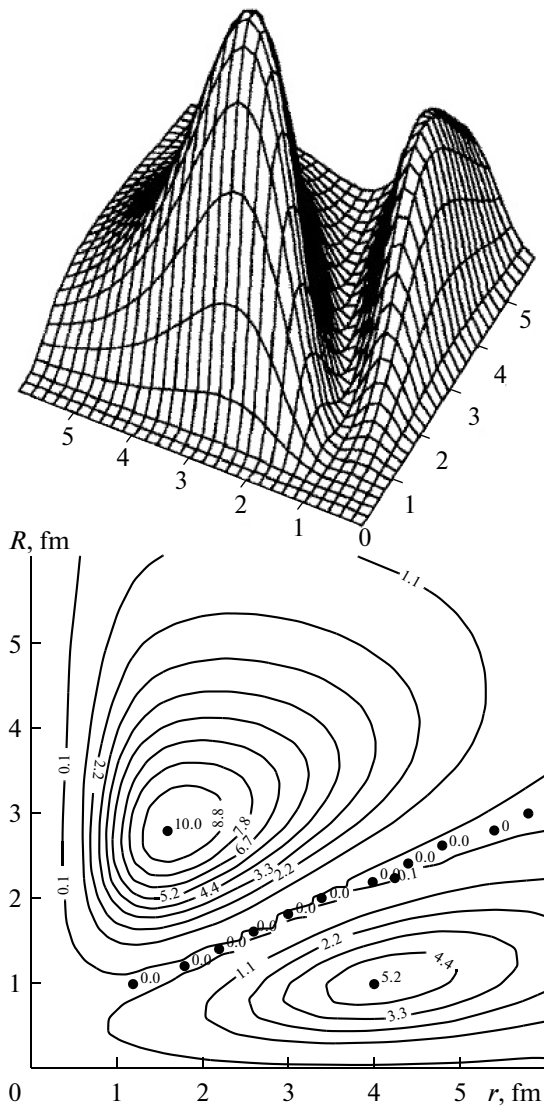


**Fig. 2.** The density profiles (at the top) and isolines (at the bottom) of WFs of the  ${}^6\text{He}$  nucleus with  $\lambda/LS = 0000$ , calculated in model 1 (Table 1) from [68].

two components, to which we restrict ourselves in the calculation:

$$\Psi_{\lambda/LS}^{JM_J}(\mathbf{r}, \mathbf{R}) = \Psi_{0000}^{JM_J}(\mathbf{r}, \mathbf{R}) + \Psi_{1111}^{JM_J}(\mathbf{r}, \mathbf{R}), \quad (1.8)$$

where

$$\begin{aligned} \Psi_{\lambda=0/l=0/L=0/S=0}^{JM_J}(\mathbf{r}, \mathbf{R}) &= \Psi_{0000}^{JM_J}(\mathbf{r}, \mathbf{R}) \\ &= \frac{1}{4\pi} \sum_{i,j} C_{ij}^{00} \exp(-\alpha_i r^2 - \beta_j R^2), \end{aligned} \quad (1.9)$$

$$\begin{aligned} \Psi_{\lambda=1/l=1/L=1/S=1}^{JM_J}(\mathbf{r}, \mathbf{R}) &= \Psi_{1111}^{JM_J}(\mathbf{r}, \mathbf{R}) \\ &= \sum_{m\mu M_L M_S} \langle 1m1\mu | 1M_L \rangle \langle 1M_L 1M_S | JM_J \rangle \\ &\times Y_{1m}(\mathbf{R}) Y_{1\mu}(\mathbf{r}) \sum_{i,j} C_{ij}^{11} r R \exp(-\alpha_i r^2 - \beta_j R^2). \end{aligned} \quad (1.10)$$

Table 1 presents the interaction potentials, the considered configurations of the  ${}^6\text{He}$  nucleus WFs in two models. The basic difference between models 1 and 2 is that the Pauli Exclusion Principle is taken into consideration in the three-body nuclear model. The procedure of taking into account the Pauli Exclusion Principle for many-nucleon systems correctly is pretty involved and is not performed here, within the used three-cluster model with projection on the forbidden states (FS). Researchers usually resort to different approximate methods: adding a hard core to the typical nucleon–nucleon or cluster–cluster interactions or introducing the operator of projection on FS into the dynamic equations. The following exclusion of these states from the WFs creates the effective repulsion at small distances between the clusters which acts as a soft core. Wave functions of the relative motion of clusters are suppressed in this region, and the higher the FS number the stronger the suppression. The Pauli Exclusion Principle in [70–73] is effectively taken into account by introducing the deep attraction potential with FS. The WFs with a node in the region of cluster overlap are characteristic of the deep attracting potentials with FS. The WFs vanishing in the cluster overlap region are characteristic for potentials with the repulsing core. The antisymmetrization effect is small for the  ${}^6\text{He}$  nucleus; therefore, as is shown in [73], it exerts almost no influence on its rms radius and other characteristics.

The parameterization of a nuclear WF in the convenient form (see (1.4)) allows one to analyze the geometric form of nuclear states so that, having seen the individual details of their structure, one could understand what influence the structure exerts on the scattering characteristics. Figures 2 and 3 (at the top) demonstrate the density profiles

$$W(r, R) = \sum_{\lambda,l} |\Phi_{\lambda,l}(r, R)|^2 r^2 R^2 \quad (1.11)$$

and isolines (Figs. 2 and 3 (at the bottom)) of WF components of the  ${}^6\text{He}$  nucleus, calculated with the SBB  $\alpha$ – $n$ -potential and the RSC  $NN$  potential (model 1) from [68]. As is seen from Fig. 2, the  $S$ -state  $\lambda/LS = 0000$  includes two geometric configurations: the dineutron  $\alpha$ – $(2n)$ - and cigar-like  $n$ – $\alpha$ – $n$ -configurations with  $\alpha$ -particle between two neutrons. These configurations are characterized by the following intranuclear distances: for the  $\alpha$ – $(2n)$  configuration  $r = 1.7$  fm and  $R = 3$  fm; for the  $(n$ – $\alpha$ – $n)$  configuration  $r = 4$  fm,  $R = 1$  fm, where  $r$  and  $R$  are the mean distances between two neutrons and between the center-of-mass of two neutrons and  $\alpha$ -particle, respectively (see Fig. 1). From the fact that in the  $\alpha$ – $(2n)$  configuration  $r = 1.7$  fm, it follows that the dineutron cluster in the nucleus is strongly compressed as compared to the free deuteron whose radius  $r_d = 4.3$  fm. The configuration  $\lambda/LS = 1111$  of the  $P$ -state is close to the

isosceles triangle with  $r = 2.3$  fm and  $R = 1.8$  fm, which rotates around the common center-of-mass of the nucleus (Fig. 3).

The calculation of the three-cluster correlation function (defined as in (1.11)) in the context of algebraic version of RGM [43] for the  ${}^6\text{He}$  nucleus (and the  ${}^8\text{He}$  nucleus) confirmed the presence of two configurations of WFs, called by the authors as triangular (similar to dineutron configuration) and linear (analogous to cigar-like configuration). The probability of revealing a nucleus in the first configuration is four times higher than that in the second one. In recent work [117], with “microscopic” consideration of geometry of Borromean nuclei, an estimation of the full geometry of two valence halo-nucleons was obtained. Analyzing  $B(E1)$  from the electromagnetic breakup of the  ${}^6\text{He}$  nucleus jointly with the analysis of the Hanbury–Brown–Twiss (HTB) correlations of two neutrons, the authors found that an angle between the valence neutrons in the  ${}^6\text{He}$  nucleus is  $83^\circ$ . These results fit the data of both [28, 29] and [43, 68, 100, 101], though WFs are calculated using different methods: on the hyperspherical basis in [28, 29], on the many-body oscillator basis in [43], on the Gaussian function basis in [68], and in DWIA [100, 101]. The calculated configurations of relative position of the clusters for the  ${}^6\text{He}$  nucleus are compared to the configuration for  ${}^8\text{He}$  [43]. It is found that the dominating configuration in  ${}^8\text{He}$  forms an isosceles triangle with an angle close to the right angle, at the vertex of which there is an  $\alpha$ -particle, and with dineutron clusters in its base, i.e., a certain configuration that is intermediate between the dineutron and cigar-like configurations takes place. A difference in geometry is explained by implementation of the Pauli Exclusion Principle: the effective repulsion between the dineutron clusters takes place in  ${}^8\text{He}$ , as a result of which they are located on the opposite sides of the  $\alpha$ -particle core; in  ${}^6\text{He}$ , the neutrons with opposing spins in the presence of the massive core form a compact dineutron (its rms radius in the nucleus is 2.52 fm, which is less than a radius of a free deuteron).

The size of a nucleus and also the distribution of nuclear matter density are the most important characteristics in determining the WF extent, nuclear potential, and one-body orbitals. At present, the laser-spectroscopic method is most accurate, in which the ultrafine structure and isotope shift of atomic transfer between two isotopes, cooled and caught in the magnetic-optical trap, are measured, from which a difference between charge radii of the investigated isotopes is determined. Based on the absolute magnitude of the charge radius  $R_{ch}^{4\text{He}} = 1.676(8)$  fm [118], measured using the spectroscopy of muonic  ${}^4\text{He}$  atoms, the rms nuclear charge radius of the  ${}^6\text{He}$  nucleus  $R_{ch}^{6\text{He}} = 2.054(14)$  fm [119] was found using laser spectroscopy. Thus-determined rms point-proton radius, which is

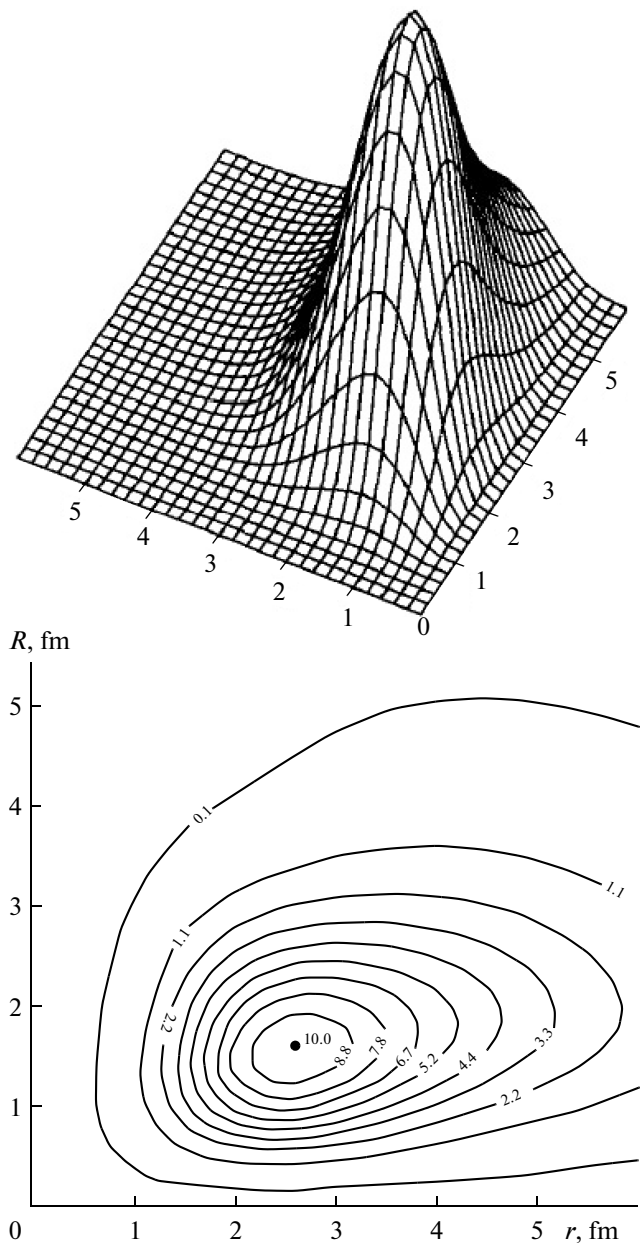


Fig. 3. The same as in Fig. 2 for the  $P$ -state with  $\lambda/LS = 1111$ .

usually referred to, has a value of  $r_p = 1.91(2)$  fm [119]. A little bit later the  $R_{ch}^{6\text{He}}$  value was refined:  $R_{ch}^{6\text{He}} = 2.068(11)$  and the charge radius of  ${}^8\text{He}$  was determined as  $R_{ch}^{8\text{He}} = 1.929(26)$  fm [120].

The comparison of the rms matter and charge radii of the  ${}^6\text{He}$  and  ${}^8\text{He}$  isotopes, performed in [120], demonstrates an interesting picture: the matter radius of  ${}^8\text{He}$  exceeds that of  ${}^6\text{He}$ , whereas its charge radius is less than that of  ${}^6\text{He}$ . The fact that  $R_m^{8\text{He}} > R_m^{6\text{He}}$  is understandable and explained by the higher number of nucleons. However, the opposite inequality for the

**Table 2.** The rms values of the matter ( $R_m$ ), neutron ( $r_n$ ), proton ( $r_p$ ), “halo” ( $r_h$ ), and core ( $r_c$ ) radii for  ${}^6\text{He}$ , extracted from experiments published in literature

No.	$R_m$ (fm)	$r_n$ (fm) $r_h$	$r_p$ (fm) $r_c$	$\delta_{np} = r_n - r_p$ (fm)	Reference
1	2.33(4)	2.59(4)	1.72(3)	0.87(6)	3, 4
2	2.30(7)	2.97(26)	1.88(12)		105
3	2.36(6)	2.97(8)	1.97(9)		121
4	2.45(10)	3.23(31)	1.88(12)		122, 123

charge radii  $R_{ch}^{8\text{He}} < R_{ch}^{6\text{He}}$  needs the explanation. The larger charge radius of  ${}^6\text{He}$  (in comparison to that of  ${}^8\text{He}$ ) is determined by its internal structure: two excess neutrons are correlated in such a manner that their location is more probable on the same side of the core (dineutron configuration) than on its opposite sides (cigar-like configuration). As a result, the  $\alpha$ -like core motion with respect to the correlated pair of neutrons smears the charge distribution over the larger volume. On the contrary, four excess neutrons in  ${}^8\text{He}$  are distributed in the more spherically-symmetrical manner in halo and the charge smearing in the core is correspondingly less, which leads to reduction in charge radius [120]. Thus, the comparison of  ${}^6\text{He}$  and  ${}^8\text{He}$  shows that the addition of the larger number of valence nucleons to the  $\alpha$ -particle core hinders the additional spatial “swelling” of the nucleus, which is determined by the charge radii ratio. The radii values extracted from the experimental data are given in Table 2.

The rms matter radius  $R_m = \sqrt{R_{rms}^2}$  can be obtained using different methods, but not all of them are in agreement with each other, leading to different results. Performing calculations within Glauber formalism, it is possible to obtain  $R_m$  both from the slope of the DCS curve and from the total cross section. These methods are matched and yield identical results.

Tanihata [3, 4] was one of the first to estimate the total matter density of  ${}^6\text{He}$  from the data on total cross sections and obtained  $R_m = 2.33(4)$  fm (Table 2). The calculation of the rms radius  $R_m$ , performed by Alkhozov from the experimental data at  $E = 0.700$  GeV/nucleon within the Glauber theory with assumption that the  ${}^6\text{He}$  nucleus density is a product of the one-body densities of nucleons, resulted in a value of 2.30 fm [110] (see Table 2). Furthermore, from the analysis of the same experimental data as in [110, 121] but with the use of four phenomenological density distributions: (1) SF (symmetrical Fermi), (2) GH (Gaussian with halo), (3) GG (Gaussian with Gauss, the first letter determines the nucleon distribution in the core, the second one denotes the same in the halo), (4) GO (Gaussian with oscillator), the rms radii of the core, halo, and the entire matter of the  ${}^6\text{He}$  nucleus have been calculated,

whose values are somewhat larger than those obtained earlier (Table 2, line 4) [122, 123].

Initially, in the experiment carried out at GSI [110, 121], the DCS was measured to  $|t| \leq 0.05$  (GeV/c) $^2$ . In the experiment [124] on measuring the DCS of protons on the  ${}^{6,8}\text{He}$  nuclei, carried out at GSI at the same IKAR facility at  $E = 0.717$  MeV/nucleon, the range of transferred momenta  $|t| \approx 0.2$  (GeV/c) $^2$  was substantially expanded. From the measured DCS with five different densities (WS (Woods–Saxon), SF, GH, GG, and GO), the radii  $R_m, r_c, r_h$  were obtained. Their averaged values for  ${}^6\text{He}$  are given in Table 2 under number 3.

The rms radii from the calculations, based on the few-body model [26, 28, 68, 71, 87, 111, 125, 126], LSSM [78], the Monte Carlo method (the variational MCM (VMCM), Green’s function (GMCM)) with realistic two- and three-body interactions [65] and in the algebraic version of RGM [43], are given in Table 3. From comparing the data obtained using different methods, we may draw the following conclusion: the calculation with the few-body WFs (three-body  $\alpha$ - $n$ - $n$ ) results in the rms radius by 0.1–0.2 fm larger than the calculation with the one-body densities performed in [1, 110]. The analysis carried out in [111] showed that the increase in radius is due to the internal compound structure inherent in the many-body WFs and their realistic (extended) asymptotics. As it is noted by the authors who performed calculations in the different three-body models with realistic or effective pair interactions [111, 123, 125], they have the common problem of energy underboundness, i.e.,  $E_{2n} = -0.4$  MeV instead of  $E_{2n}^{\text{exp}} = -0.973$  MeV [127]. Therefore, in order that the radii and binding energy should be described consistently, the shape of effective potential is varied [128], the other close channel ( $t$ - $t$ ) or the  $\alpha$ -like core polarization [50] is taken into consideration. For example, in [126], in order that the binding energy should be fitted, the Minnesota (MN) potential, used in the calculation, was renormalized with increasing the force of long-wave region, and it was named MMN (modified MN). As it was expected, the calculation using the MMN potential resulted in the decrease of  $R_m$  from 2.63 to 2.49 fm and in the  $E_{2n}$  value agreed with the experimental data.

As is seen from Table 3, the matter radius  $R_m$  and the halo/skin radius  $\delta_{np} = r_n - r_p$  calculated with the WFs of  ${}^6\text{He}$  in the MDM [68] or in AMDM [71], which we use in the further calculations, agree with both experimental value, and with calculations of other authors in few-body models. Let us also note that the antisymmetrization influences (insignificantly) the rms matter radius and skin size, as well as the binding energy of two neutrons: in both models it is underbound ( $E_{2n} = -0.14$  MeV).

**Table 3.** The rms values (in fm) of the matter ( $R_m$ ), neutron ( $r_n$ ), proton ( $r_p$ ), “halo” ( $r_h$ ), and core ( $r_c$ ) radii for  ${}^6\text{He}$ , calculated using different methods

No.	$R_m$	$r_n$ $r_h$	$r_p$ $r_c$	$\delta_{np} = r_n - r_p$	Reference	Note
1	2.54–3.75	3.39–5.84	1.6–2.0		26, 28	Few-body WF
2	2.32–2.66		1.84–2.05		83, 106	Few-body WF
3	2.43–2.44 2.44–2.61 2.36–2.46				120	Gaussian basis Hyperspherical basis Few-body WF
4	2.51 2.56 2.61				61	Cluster WF VMCM GMCM
5	2.69	2.96	2.06	0.9	42	Algebraic version of RGM
7	2.62	2.90	1.945	$R_{ch} = 2.147$	74	LSSM
9	2.56 2.63 2.49			$R_{ch} = 2.07$	121	G3RS MN MMN
10	2.43			0.74	64	MDM
11	2.44			0.8	67	AMDM

### 1.2. The Wave Function of the ${}^8\text{Li}$ Nucleus

The  ${}^8\text{Li}$  nucleus, unstable in  $\beta^-$  and in  $\beta^-2\alpha$ , decays with a lifetime of 0.838 s, is of interest for nuclear, both in and of itself and for astrophysics, because the  ${}^7\text{Li}(n, \gamma){}^8\text{Li}$  radiation-capture reaction fills the gap (at  $A = 8$ ) in the chain of thermonuclear synthesis reactions of CNO-elements in the nonstandard model of nucleosynthesis after the so-called inhomogeneous Big Bang. A rate of this reaction is important for understanding the primary synthesis of elements. It appears to be also necessary for solving the problem of high-energy solar neutrinos which are produced in the  ${}^7\text{Be}(p, \gamma){}^8\text{B}$  mirror reaction (after  $\beta$ -decay of  ${}^8\text{B}$ ). Since its cross section is not measured experimentally at low solar energies (on the order of 20 keV) due to the presence of the Coulomb barrier, then it is to be extrapolated from the cross section at the higher energies (on the order of hundreds keV). The constants required for the extrapolation (model parameters) are extracted from the well-measured (to  $10^{-3}$  eV) cross section of the  ${}^7\text{Li}(n, \gamma){}^8\text{Li}$  reaction. In [129, 130], with WFs in the  $\alpha-t-n$  model, the basic spectroscopic characteristics (the rms charge radius, the quadrupole and magnetic moments) are calculated and the total cross sections and rates of the  ${}^7\text{Li}(n, \gamma){}^8\text{Li}$  reaction are found in a range from  $10^{-5}$  keV to 1 MeV. Let us note that the energy range comprises eight orders in energy and the calculated total cross sections coincide with the experimental data available in the entire range.

The modern WFs of the  ${}^8\text{Li}$  nucleus are calculated in the three-body  $\alpha-t-n$  models with realistic potentials of intercluster interactions. The arguments in favor of the  $\alpha-t-n$  model are as follows: the smallness

of the three-body energy threshold of decay in this channel ( $E = 4.501$  MeV) with respect to other nearest three-body channels, e.g.,  ${}^6\text{Li}-n-n$  ( $E = 9.283$  MeV) or  ${}^5\text{He} + d + n$  ( $E = 11.653$  MeV); the dominating contribution (with a weight of 0.981) to the WFs of the nucleus ground state in the MBMS [52] yields the configuration with the Young scheme [431], and, as is shown in [131], this scheme corresponds to the  $\alpha-t-n$  configuration. The reaction of proton knockout from the  ${}^9\text{Be}$  nucleus may serve as another argument in favor of the  $\alpha-t-n$  model of the  ${}^8\text{Li}$  nucleus. As is known, the properties of the  ${}^9\text{Be}$  nucleus are most successfully described now in the three-body  $\alpha-\alpha-n$  model [72]. The reaction of proton knockout from the  $\alpha-\alpha-n$  system can be explained by the proton knockout from the  $\alpha$ -cluster, which should result in formation of the  ${}^8\text{Li}$  nucleus with the  $\alpha-t-n$  structure. In using the WFs of the MBMS, it is shown in [132] that the spectroscopic factor for the proton separation from the ground state of the  ${}^9\text{Be}$  nucleus has a large value of  $S = 1.07$  in good agreement with the experiment [127].

The  ${}^8\text{Li}$  nucleus and the  ${}^8\text{B}$  nucleus which is a mirror one with respect to the latter have been intensively investigated in recent decades both experimentally and theoretically. We shall dwell upon several theoretical works. The first one was [133], in which the  ${}^8\text{Li}$  nucleus was considered in the context of one of the RGM modifications (using the linear amplitude method). The  ${}^7\text{Li}-n$ ,  ${}^7\text{Li}^*-n$ ,  ${}^5\text{He}-t$ , and  ${}^5\text{He}^*-t$  two-body channels were taken into account. The main contribution to the ground and first excited states were made by the first two. The calculated energy spectrum of levels reproduced the experiment as a whole; how-

ever, the obtained WFs were not tested in the description of static electromagnetic characteristics. Moreover, the model suggested in [133] predicted the levels with negative parity, the existence of which is not yet established with certainty.

In the next work [134], the RGM algebraic version was applied in studying the  ${}^8\text{Li}$  nucleus. This approach avoided some of the drawbacks of the previous [133]; it has also the advantage that the Hamiltonian matrix elements were calculated analytically. The  ${}^8\text{Li}$  nucleus was considered as the  ${}^7\text{Li}-n$  system. The energy spectrum alone was investigated. The ground state appeared to be underbound approximately by 1 MeV; additionally, the model predicted the second excited level with quantum numbers of  $J^\pi, T = 1^+, 1$  and some other levels, experimentally unobservable; the negative-parity levels were not mentioned. The authors explained the quantitative discrepancy between the obtained spectrum and experimental data by disregarding the cluster structure of the  ${}^7\text{Li}$  nucleus, vital for resonant states of the  ${}^8\text{Li}$  nucleus, the  ${}^4\text{He}-t-n$  three-cluster channel and tensor forces.

In [135], in the RGM context, the two-body coupled channels were substituted for three-body single-channel  $\alpha-t-n$  model; however, this was a modified version of the two-body model with two channels ( ${}^7\text{Li}-n$  and  ${}^7\text{Li}^*-n$ ), where the  ${}^7\text{Li}$  and  ${}^7\text{Li}^*$  subsystems were considered as the  $\alpha t$  systems. This work was directly devoted to studying the  ${}^7\text{Li}(n, \gamma){}^8\text{Li}$  and  ${}^7\text{Be}(p, \gamma){}^8\text{B}$  reactions. The Volkov  $NN$  forces were used in the calculations; the Coulomb interaction was considered exactly. The ground state was precisely fitted though the magnetic moment was undervalued by 30%. The first excited state  $1^+$  appeared overbound by 0.7 MeV. The calculations predicted the second level  $1^+$  with an energy of 0.12 MeV, whereas the experiment yielded a value of 1.18 MeV. The well-known level  $3^+$  was not reproduced by the model; the authors associated this with disregard for the  ${}^5\text{He}-t$  channel, however the level  $0^+$  was predicted, which was not experimentally determined at the time. The calculations yielded no levels of negative parity.

In [136], the characteristics of low-lying levels, corresponding to resonances in the  ${}^8\text{Li}$  and  ${}^8\text{B}$  systems were used. The reliability of the obtained results was verified by finding the poles of the matrix of the  ${}^7\text{Li}-n$  and  ${}^7\text{Be}-p$  scattering and describing the first excited level  $J^\pi, T = 1^+, 1$ . The previously-used Minnesota forces that did not describe the first excited level were substituted for the modified Hasegawa–Nagata potential. The model failed to reproduce the two-body threshold of breakup into the  ${}^7\text{Li}-n$  and  ${}^7\text{Be}-p$  subsystems. It was found that the commonly accepted order of levels  $J^\pi, T = 2^+, 1; 1^+, 1; 3^+, 1; 1^+, 1$  was added by the state  $J^\pi, T = 1^+, 1$  with the energy  $E = 1.278$  MeV and the level width  $\Gamma_n = 0.564$  MeV, which

was located between the first excited level  $J^\pi, T = 1^+, 1$  and the level  $J^\pi, T = 3^+, 1$ .

In [137], the authors applied the shell model embedded in the continuum (SMEC) for the microscopic description of the  ${}^8\text{Li}-{}^8\text{B}$  nuclear spectrum as well as of the  ${}^7\text{Li}(n, \gamma){}^8\text{Li}$  and  ${}^7\text{Be}(p, \gamma){}^8\text{B}$  radiation-capture reactions. The coupling between channels of the continuous spectrum and the bound states takes place in the SMEC. The coupling of channels is implemented by the residual nucleon–nucleon interaction. This model allows one to self-consistently calculate the averaged potential of the  ${}^7\text{Li}-n$  interaction and the integral of overlapping of the continuous spectrum and the bound states. The energy spectrum and electromagnetic characteristics of the ground state were investigated. The ground and first excited states of the  ${}^8\text{Li}$  nucleus appeared to be underbound by 0.5 MeV. The resonant states, corresponding to the second and third excited levels, were reproduced almost exactly. The quadrupole moment of the  ${}^8\text{Li}$  nucleus appeared equal to  $Q_{\text{theor}} = 27.8$  mb (for  $Q_{\text{exper}} = 32.7(6)$  mb).

In [138], the  ${}^8\text{Li}$  and  ${}^8\text{B}$  nuclei are considered within the three-body problem on the hyperspherical-harmonic basis as the  $\alpha-t-n$  and  $\alpha-\tau-p$  systems, respectively. The authors stress that in the three-body approach, the main effects of strong deformation and dynamic polarization of a nucleus and also the effects of the core excitation are simultaneously taken into account, as distinguished from the two-body problem. At the same time, the four- and five-body configurations are only corrections to the three-body channel. The data on the  $\beta$ -decay of the  ${}^8\text{He}$  nucleus to the first excited state of the  ${}^8\text{Li}$  nucleus made it possible to estimate the contribution of the five-body configuration. It proved to be small in comparison with that for the three-body configuration. The pair interaction potentials were used in the calculations, in which the Pauli Exclusion Principle was taken into account by introducing the repulsive core. The Coulomb interaction was considered exactly rather than as a perturbation. The ground state proved to be overbound by 0.14 MeV. The first excited state differed slightly from its experimental value. The remaining levels were not considered. The magnetic moment was obtained smaller than its experimental value by 18%; the quadrupole moment, by 35%.

Almost all the works in one way or another deal with the two-body model, therefore all multiparticle effects inherent in the three-body problem drop out of consideration. In all works, except for [138], the nucleon–nucleon potential was varied, therefore there is no full consistency of calculations. In [138], the method of taking into account the Pauli Exclusion Principle by introducing the repulsive core is not quite correct because, as it is well-known at present, potentials with the repulsive core poorly describe the Cou-

lomb excitation reactions in comparison with the deep potentials containing the FSs.

**1.2.1. Choice of the intercluster interaction potentials and the considered configurations.** For description of the  ${}^8\text{Li}$  nucleus the three-body  $\alpha-t-n$  model is used with three pair  $\alpha-t$ ,  $\alpha-n$  and  $t-n$  interactions including the states forbidden by the Pauli Exclusion Principle.

The interaction Hamiltonian takes into account only central and spin-orbit forces, containing the orbital splitting, while for the  $t-n$  potential the splitting in the total spin is included. The influence of tensor interactions on the characteristics of the ground state of the  ${}^8\text{Li}$  nucleus is additionally considered. The Pauli Exclusion Principle is approximately taken into account by means of orthogonalization of the total WF to the forbidden states of pair subsystems. The Coulomb interaction is taken in our calculations exactly, which allows us to check a number of fine effects connected with the potential barrier and is particularly important in astrophysical problems. In a more rigorous approach based on the Faddeev's equations, the exact consideration for the Coulomb interaction is such an involved problem that it was performed only in isolated works.

Any physical nuclear model contains some parameters. For instance, the main input parameter in MBMS and RGM is the  $NN$  interaction. A strong sensitivity of results to the form of the  $NN$  forces is the general RGM drawback because the best results are, as a rule, achieved with  $NN$  potentials which are not the best ones. There are parameters in our model which may be conventionally divided into two types: (a) parameters of the variational basis; (b) parameters of clusters and their interactions.

The first type of parameters is chosen, as a rule, in such a manner that with the least dimensions of the basis, the WF internal and peripheral parts would be better reconstructed. Let us note that the correct description of the periphery in the MBMS and RGM is almost impossible because, although the WF internal part is correct owing to the complete antisymmetrization, the self-consistence is lost in the  $NN$  interaction due to the core removal.

The second type of parameters is fixed in such a way that the observable properties of free cluster and systems consisting of two clusters could be reconstructed most completely. Therefore the static electromagnetic characteristics of virtual clusters were chosen identical to the experimental values for free particles. Parameters of cluster interaction potentials are fitted from the condition of the most complete description of properties of the two-cluster system both in the bound state and in the state of scattering.

The interaction potentials in this model are chosen in such a manner that they would describe phase shifts of elastic scattering for waves with the small value of the relative orbital angular momentum and the characteristics of bound states of the pair subsystems

(if such are available). The deep potentials of Gaussian shape with FSs [139, 140] were mainly used as the two-body interaction potentials. For more extensive investigation, a Woods-Saxon potential was also used.

Table 4 presents the summary of potentials of intercluster interactions, used in calculations of the WFs, and the basic static characteristics of the nucleus. The model WFs of the  ${}^8\text{Li}$  nucleus were calculated with different  $\alpha-t$  potentials, because its impact on the properties of the ground state of the nucleus is stronger than that of the  $\alpha-n$  and  $t-n$  potentials.

The following potentials were used as the  $\alpha-t$  interaction.

**Models 1 and 2.** The 8-parameter potential of Gaussian shape with FSs [139] is constructed for the adequate reconstruction of both the partial scattering phase shifts split in parity of the orbital angular momentum and spin-orbit interaction and the characteristics of bound states. Additionally, the potential satisfactorily describes the electromagnetic form factors and the  $\alpha t \rightarrow {}^7\text{Li}\gamma$  radiation-capture reaction.

**Model 3.** The Buck attractive potential, whose radial part has a Gaussian form, contains two parameters and includes the spin-orbit and the Coulomb terms [141]. The potential is calculated on the basis of the double folding model, where the nucleon densities of clusters obtained from the data on electron scattering are averaged. Then the potential parameters were refined by matching them to phase shifts of scattering and characteristics of bound state. It reproduces both the known low-energy phase shift of the  $\alpha-t$  scattering and the binding energy, and the low-energy spectrum of the  ${}^7\text{Li}$  nucleus levels and basic spectroscopic characteristics of this nucleus. Here, the radial function of the ground state of the  ${}^7\text{Li}$  nucleus contains an internal node, i.e., has the form of the oscillator function  $R_{3p}(r)$ . The Buck potential reliably describes the total cross section and astrophysical  $S$ -factor for the  $\alpha t \rightarrow {}^7\text{Li}\gamma$  radiation-capture reaction.

The potentials of Gaussian shape have the advantage from the computing standpoint. Their matrix elements include the combinations of factorials and powers of Gaussian parameters. However, these potentials rapidly drop on asymptotics, and the practice showed that the potentials of Woods-Saxon shape describe better the elastic scattering data.

**Model 4.** The deep attractive potential of Woods-Saxon shape, to which the spin-orbit and Coulomb terms are added. The potential is sufficiently deep to contain the forbidden  $1p$ -state in the  $p$ -wave in addition to the allowed  $3p$ -state. The Woods-Saxon potential completely reproduces the known low-energy phase shifts of the  $\alpha-t$  elastic scattering and at the same time correctly describes the binding energy and the spectrum of low-lying state of the  ${}^7\text{Li}$  nucleus and its basic spectroscopic characteristics. The adequate description of the  ${}^7\text{Li}(\gamma, t)\alpha$  reaction of two-

**Table 4.** The interaction potentials, the considered WF configurations used in the calculations of static characteristics of the  ${}^8\text{Li}$  nucleus in the  $\alpha$ - $t$ - $n$  model; experimental data:  $R_m = 2.37(2)$  [1–3],  $2.50(6)$  [123] fm,  $E = -4.501$  MeV,  $Q = 24(2)$  [144],  $32.7(6)$  mb [145],  $\mu = 1.65\mu_0$  [146]

Potential	Model 1 [129]	Model 2 [130]	Model 3 [130]	Model 4 [130]	Model 5 [147]	Model 6 [147]
$\alpha$ - $t$	Gaussian potential, containing eight parameters [134]	The same as in model 1, with expanded basis [134]	Gaussian potential in the Buck form [136], with supersymmetric repulsive part at small distances	Standard potential of Woods–Saxon shape	The same as in model 3	The same as in model 3 including tensor interaction
$\alpha$ - $n$	Gaussian potential, split in parity of orbital angular momentum [115]					
$t$ - $n$	Gaussian potential, split in total spin [140]				The same as in model 1 including tensor interaction	The same as in model 1
Configuration	Configuration weight ( $P$ )					
$\lambda$ $l$ $L$ $S$						
1    1    1    1	1.00	0.9935	0.9880	0.9940	0.8721	0.8818
1    1    2    1		0.0015	0.0024	0.0014	0.0281	0.0712
3    1    2    1		0.0022	0.0045	0.0018	0.0580	0.0378
3    1    2    0		0.0015	0.0032	0.0016		
3    1    3    1					0.0268	
Static characteristics						
$\langle r_m^2 \rangle^{1/2}$ , fm	2.36	2.355	2.348	2.279	2.34	2.38
$E$ , MeV	-3.82	-4.267	-4.406	-4.883	-5.7	-4.657
$\mu$ , $\mu_0$	1.473	1.44	1.408	1.442	1.607	1.624
$Q$ , mb	16.55	18.45	18.94	16.69	30.75	30.36

body photosplitting [142] was achieved precisely with this potential.

The potential of the  $\alpha$ - $n$  interaction was initially chosen as the Saka–Biedenharn–Breit (SBB) potential [115], whose central part has the Gaussian shape. The SBB potential reasonably describes the basic  $P_{1/2}$  and  $P_{3/2}$  phase shifts of the  $\alpha$ - $n$  elastic scattering, and it describes the  $S$ -phase shifts up to an energy of 14 MeV with poorer accuracy. A main drawback of the SBB potential is the strong overestimating of the theoretical  $D_{5/2}$  and  $D_{3/2}$  phase shifts with respect to experiment. The improved  $\alpha$ - $n$  potential, containing the splitting of phase shifts in parity of the orbital angular momentum [70, 143], describes the  $S$  and especially  $D_{5/2}$  and  $D_{3/2}$  phase shifts more accurately than that of initial variant. The potential has one FS in the  $S$ -wave. The Coulomb term is added for the  $\alpha$ - $p$  system, which has the form of the Coulomb interaction of point proton with the Gaussian distribution of the charge with the width  $a = 1.34$  fm.

The potential of the  $n$ - $t$  interaction was chosen in the form of linear combination of the Gaussian and the repulsive exponent [140]. The exponential repulsive addition is present in order to describe the behavior of phase shifts when the total spin is zero. Such a parameterization corresponds to the strong spin dependence of the potential of the fermion interaction; moreover, it is in agreement with the virtual

exchange by deuteron that (being a boson) can be the carrier of interaction. Parameters of the  $n$ - $t$  interaction were taken the same as for  $p^3\text{He}$ , because their quantum states coincide. It should be noted that this is not a potential with a hard core, but a deep attractive potential with FSs. The potential has two forbidden  $S$ -states with the total system spin being 0 and 1. For the  $p$ - $t$  system, the Coulomb potential is added in the form of interaction of two point charges.

The procedure of the WF calculation within the variational approach consists in finding the Hamiltonian matrix-elements and further solving of the matrix problem on eigenvalues and eigenfunctions.

While choosing the basic configurations for the WF calculation, it is necessary to take into account the  ${}^7\text{Li}$ - $n$  two-cluster structure. This is caused by the fact that a neutron in the  ${}^8\text{Li}$  nucleus is loosely bound ( $E = 2.26$  MeV), while the spectroscopic factor of the  ${}^7\text{Li}$  nucleus in the  $\alpha$ - $t$  channel is almost equal to unity. The  ${}^7\text{Li}$  nucleus in the ground state has the quantum numbers  $J^\pi$ ,  $T = 3/2^-, 1/2$  [144]. In the context of the MBMS, the main contribution to the WF comes from the  $[3]^{22}P$  configuration with a weight of 0.986 [53]. Consequently, the dominating contribution to the ground state and several first excited states of the nucleus will yield the configuration with  $\lambda = 1$ . Since the parity of the  ${}^8\text{Li}$  nucleus is  $\pi = +1$ , while that of the

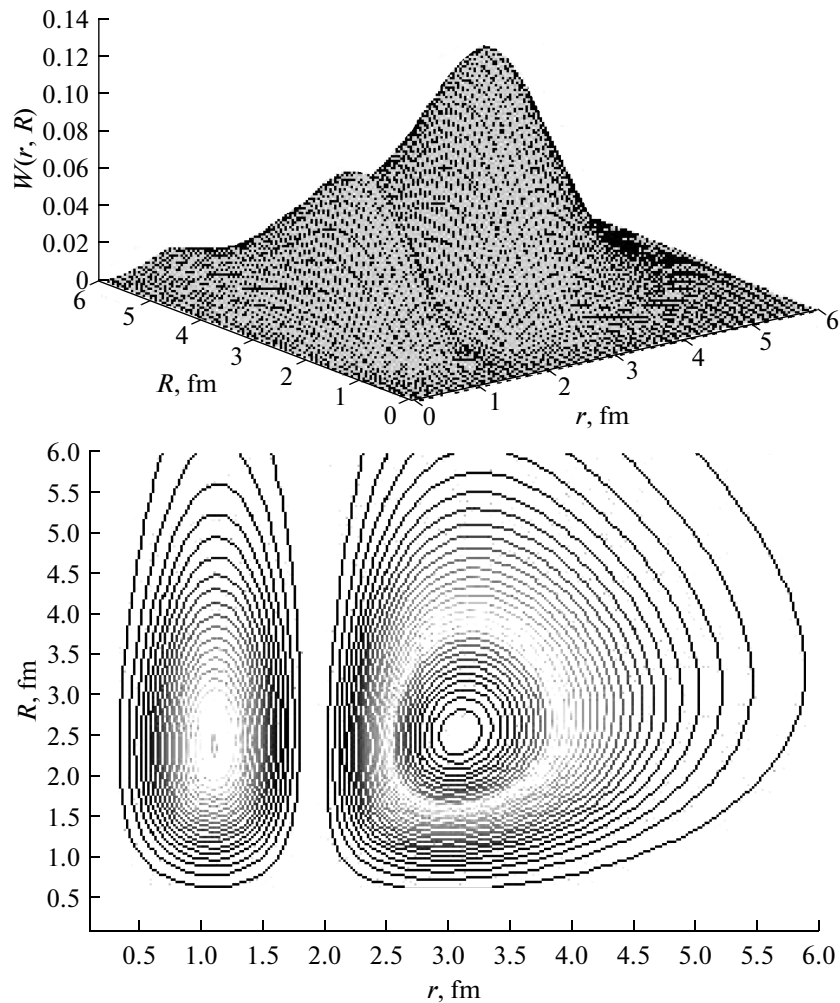


**Fig. 4.** The density profiles (at the top) and isolines (at the bottom) of WFs of the  ${}^8\text{Li}$  nucleus of configuration with  $\lambda/LS = 1111$ , calculated in model 3 (Table 4).

${}^7\text{Li}$  nucleus is  $\pi = -1$ , and a neutron is loosely bound in the  ${}^8\text{Li}$  nucleus, then  $l = 1$ ; it also follows from the fact that in the  ${}^7\text{Li} - n$  two-cluster structure there is a FS in the  $S$ -wave and the first allowable state with  $l = 1$ . Since we work in the  $LS$  coupling, in the  $t - n$  system the low-lying states in the  ${}^8\text{Li}$  nucleus have the total spin equal to unity; consequently, the spin for the basic configuration of the  ${}^8\text{Li}$  nucleus is  $S = 1$ .

The possible values of quantum numbers  $LS$  in this case are 11, 21, 20, and 31. The noticeable contribution to the total WF can be made by the configurations, whose orbital angular momenta of relative motion  $\lambda$  and  $l$  are 1 or 3 (the configuration with  $\lambda = l = 1$  is connected with the ground state in the  $\alpha - t$  and  ${}^7\text{Li} - n$  subsystems, the one with  $\lambda = 3$  is associated with the resonant state in the  $\alpha - t$  subsystem). However, we have included all possible configurations permitted by the quantum-mechanical selection rules in our calculations. Then, the configurations which make the con-

tribution less than 1% to the ground-state WF, were excluded from the further consideration.

As it should be expected, the dominating contribution to the total WF comes from the configuration with  $\lambda/LS = 1111$  ( $\lambda = 1$  is related with the ground state of the  ${}^7\text{Li}$  nucleus in the  $\alpha - t$  channel;  $l = 1$  because the  ${}^8\text{Li}$  nucleus is a  $1p$ -shell nucleus, i.e., the  $p$ -shell is filled). Contributions from the remaining configurations in total do not exceed 4% for the potentials disregarding the tensor interaction (model 1–4 in Table 4) and 10% for those taking it into consideration (models 5 and 6 in Table 4). Nevertheless, these small configurations have a substantial impact not only on nucleus characteristics, but also on the basic configuration  $\lambda/LS = 1111$ . For example, if only the configuration  $\lambda/LS = 1111$  is taken into account, the obtained quadrupole moment is 30% smaller than that for all configurations taken into consideration.

Figures 4–6 present the density profiles of radial parts of configurations (see (1.11)) depending on rela-

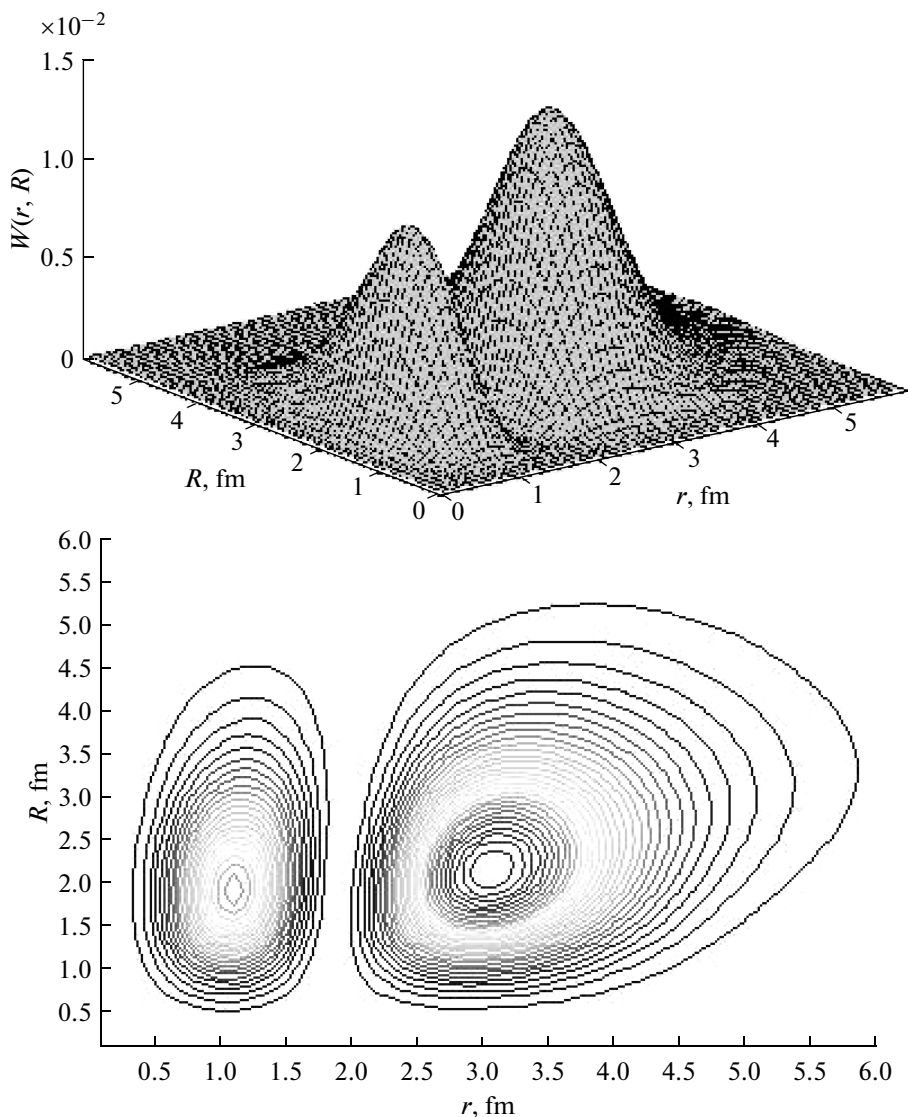


Fig. 5. The same as in Fig. 4 for configuration with  $\lambda/LS = 1121$ .

tive distances  $r, R$  for model 6 (the 3-D plots are shown at the top; isolines, at the bottom).

For the configuration with  $\lambda/LS = 1111$ , the WF in Fig. 4 has two maxima and one node at  $r = 1.766$  fm,  $R = 2.0$  fm (the radial WF of the shell type  $R_{3p}(r)$ ). In this case there is a node in the  ${}^7\text{Li}$  nucleus at  $r = 1.771$  fm for the ground state. The rms radius of the  $\alpha$ - $t$  pair in the  ${}^8\text{Li}$  nucleus  $R_m = 3.25$  fm, while in the  ${}^7\text{Li}$  nucleus  $R_m = 3.48$  fm. We may suggest that a valence neutron compresses  ${}^7\text{Li}$  inside the  ${}^8\text{Li}$  nucleus by 6.6 % in comparison with the free  ${}^7\text{Li}$  nucleus. The similar situation is observed in the  ${}^6\text{He}$  nucleus ( $\alpha$ - $n$ - $n$  model), where the configuration dominates, in which the dineutron cluster is compressed as compared to a free deuteron. There is no WF node in coordinate  $R$ , which corre-

sponds to the shell model (the radial WF of the shell type  $R_{1p}(r)$ ).

The profile of the  $\lambda/LS = 1121$  configuration in Fig. 5 is similar to the previous one. The first maximum is somewhat displaced to the nucleus center in coordinate  $R$ , while positions of the second maxima of the  $\lambda/LS = 1121$  and  $\lambda/LS = 1111$  configurations almost coincide. In coordinate  $r$ , the sharper displacement of maxima of the  $\lambda/LS = 1121$  configuration is compared to those of the  $\lambda/LS = 1111$  configuration is observed to the inside of the nucleus.

Unlike the first two profiles, the profile for the  $\lambda/LS = 3121$  configuration in Fig. 6 has one maximum at a point with the coordinates  $(r, R) = (2.5, 2.0)$  fm. This WF component at small distances from the nucleus center-of-mass is zero and drops rather fast on

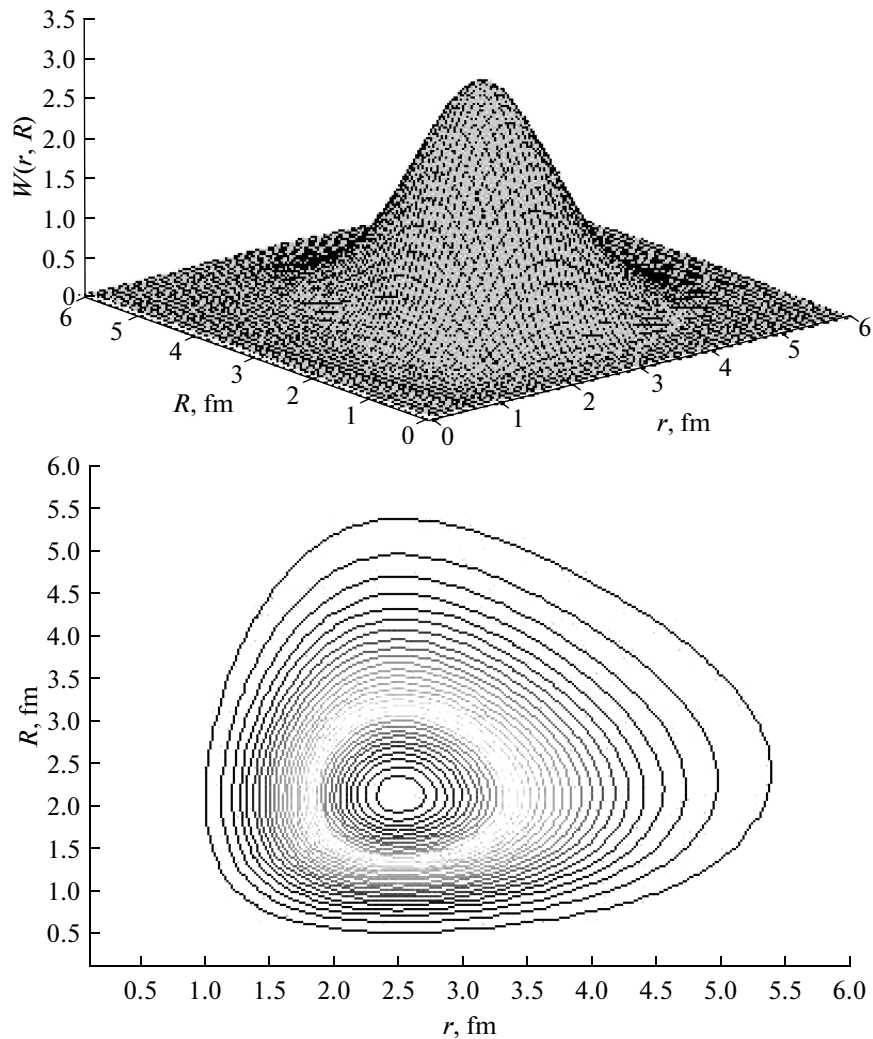


Fig. 6. The same as in Fig. 4 for configuration with  $\lambda/LS = 3121$ .

the periphery, already at  $r, R \sim 5.5$  fm. It is localized in the intermediate region of the nucleus.

**1.2.2. Calculation of static characteristics of the  ${}^8\text{Li}$  nuclei and comparison with experimental data.** The following static characteristics have been calculated with the obtained WFs: the rms charge radius, the binding energy, the quadrupole and magnetic moments (see Table 4). The values of rms radii of clusters  $R_m^\alpha = 1.71$  fm,  $R_m^t = 1.68$  fm were taken from [144]. Matrix elements from different configuration are not mixed, therefore the  $R_m$  is determined by the values of rms charge radii of clusters and by the  $\lambda/LS = 1111$  dominating configuration. The other configurations make small corrections to the value of the rms charge radius. The information on the nuclear matter distribution, extracted from the DCS measured in [123] within the diffraction theory, yielded the value  $R_m = 2.50(6)$ . The use of the charge radius data, obtained from the independent laser-spectroscopic experiments [148], made

it possible to determine both the neutron radius and the skin width  $\delta_{np} = R_n - R_p$ , which proved to be 0.52 fm and close to that calculated using the other approaches: stochastic variational method [65] and Monte Carlo method [64]. The rms radius has an approximately identical description in all models and is in agreement, within errors, with the experimental data.

The experimental value of the magnetic moment is determined with a sufficiently high accuracy. The magnetic moments of clusters  $\mu_p = +2.978643\mu_0$  and  $\mu_n = -1.913148\mu_0$  were borrowed from the experiment [146].

In the preliminary calculation variant [129], the dominating  $\lambda/LS = 1111$  configuration alone was taken into account in the WF of the  ${}^8\text{Li}$  nucleus (model 1 in Table 4). With its use, the consistent rms radius and magnetic moment were obtained; however, the authors could not reproduce correct values of the

binding energy in the channel in the ground state (it is unbound by 0.7 MeV) and of the quadrupole moment. Thus, if the basic  $\lambda/LS = 1111$  configuration alone is considered,  $Q = 16.55$  mb (model 1 in Table 4). With respect to the latter, we shall give the explanation: the value  $Q = 24(2)$  mb is given in [144], but new measurement methods increased it to  $Q = 32.7(6)$  mb [145], so that quadrupole moment, calculated in [129], is almost twice as small as the experimental value. With the purpose of improving these results, it was attempted in [130] to increase the number of the considered configurations (in particular, to include configuration with  $\lambda = 3$ , because namely in this state there is a low-energy resonance in the  $\alpha-t$  system) and to perform the calculation with three more  $\alpha-t$  potentials (variants 2–4 in Table 4), on which the properties of the ground state of  ${}^8\text{Li}$  depend stronger than on the  $\alpha-n$  and  $t-n$  potentials. However, weights of the included configurations proved to be too small (by two orders of magnitude smaller than that of the dominating  $\lambda/LS = 1111$  configuration) for the substantial influence on results of characteristic calculation, therefore this procedure yielded only the insignificant increase in the quadrupole moment. Let us note that the presence of configurations with small weight but with large orbital angular momenta can make both destructive and constructive contributions to this characteristic. Thus, the configuration with  $LS = 20$  was destructive; as it is shown in [149], it though insignificantly decreases the quadrupole moment. The inclusion of configurations with  $LS = 11$  slightly increases the quadrupole moment, it is equal to  $Q = 18.45$  and  $18.94$  mb (models 2 and 3 in Table 4). In the one-body model, the value of quadrupole moment in the  ${}^8\text{Li}$  system is directly connected with characteristics of the  $\alpha-t$  subsystem. The loosely bound chargeless neutron influences the quadrupole moment indirectly, deforming the WF of the relative motion of the  $\alpha-t$  subsystem. It is also interesting to note that in the one-body models the quadrupole moment value is proportional to the value of rms charge radius, as the matrix elements of these characteristics are equal to each other up to some factor. This is not the case in the three-body approach because the calculation is connected with taking into account many configurations, due to which the direct relation between  $Q$  and  $R_m$  disappears. Additionally, there are included configurations corresponding to resonant states of the  $\alpha-t$  subsystem, which, despite the small contribution to the total WF influence, substantially influences the quadrupole moment value.

Only in the last work [147], by means of taking into account the tensor forces in the interaction potentials, the acceptable (within 10%) agreement of the calculated quadrupole moment with experimental value (variants 5 and 6 in Table 4) was achieved. Although the tensor forces are small as compared to the central ones and exert no influence on phase shifts of elastic

scattering at low energies, they lead to mixing in orbital angular momentum, which increases the contribution of WF small components, on which depend such nuclear characteristics as the quadrupole moment and binding energy. As preliminary estimations have shown, for achieving the agreement between the calculated quadrupole moment and that of experiment, it was necessary to increase the contribution from configurations with  $LS = 21$ . At first, the calculations with the tensor interaction in the  $t-n$  subsystem were carried out, because this was the two-fermion system. The tensor interaction in the form  $V(r) = V_0 e^{-\alpha r^2} S_T$  was chosen for the calculations, where  $S_T = 3(\mathbf{S}_t \mathbf{r})(\mathbf{y}_n \mathbf{r}) - \mathbf{r}^2(\mathbf{y}_t \mathbf{y}_n)$ , is the tensor interaction operator,  $\mathbf{y}_t, \mathbf{y}_n$  are the Pauli matrices for a triton and neutron. As is seen from Table 4 (model 5), as the quadrupole moment increases, the binding energy and magnetic moment increase as well.

The tensor interaction in the  $\alpha-t$  subsystem was chosen as  $V(r) = V_0 e^{-\alpha r^2} S_T$ ,  $S_T = 3(\mathbf{S}_t \mathbf{r})(\mathbf{S}_t \mathbf{r}) - 2\mathbf{S}_t^2 \mathbf{r}^2$ ,  $S_t$  is the operator of triton spin. This form of tensor interaction is often used in the  $\hat{\alpha}-d$  interaction. As is seen in Table 4, the tensor interaction slightly changes the binding energy, whereas the quadrupole moment value is nearing its experimental value. Thus, the mere variation in the interaction potential allows one to completely describe characteristics of the  ${}^8\text{Li}$  nucleus.

As is shown in [147, 149], by varying the potential parameters  $V_0$  and  $\alpha$ , it is possible to achieve almost full coincidence of the calculated and measured  $Q$  values: at  $V_0 = -3.0$  MeV and  $\alpha = 0.11 \text{ \AA}^{-2}$  (for  $t-n$  interaction)  $Q_{\text{theor}} = 33.26$  mb. However, with these parameters the binding energy in the channel becomes  $-6.32$  MeV, which is by 1.82 MeV less than the experimental value. With account for the fact that the energy was calculated using the variational approach, this value suggests that the chosen potential is more overbound (i.e., more attractive) than it should be in reality. The most optimal description of characteristics is achieved in model 6, on which we dwell.

Based on Eqs. (1.1) and (1.2), we write down the WFs of the  ${}^8\text{Li}$  nucleus with the total angular momentum  $J$  (for the ground state  $J^\pi = 2^+, S = 1$ ) and its projections  $M_J$  in the  $\alpha-t-n$  model:

$$\Psi_{i,f}^{JM_J} = \Psi_\alpha(\mathbf{R}_\alpha) \Psi_t(\mathbf{r}_1 \mathbf{r}_2 \mathbf{r}_3) \varphi_n(\mathbf{r}_4) \sum_{\lambda LS} \Psi_{\lambda LS}^{JM_J}(\mathbf{r}, \mathbf{R}) m, \quad (1.12)$$

where  $\Psi_\alpha(\mathbf{R}_\alpha)$ ,  $\Psi_t(\mathbf{r}_1 \mathbf{r}_2 \mathbf{r}_3)$ ,  $\varphi_{2n}(\mathbf{r}_4 \mathbf{r}_5)$ ,  $\Psi_{\lambda LS}^{JM_J}(\mathbf{r}, \mathbf{R})$  are the WFs of the  $\alpha$ -particle, triton ( $t$ ), neutron ( $n$ ) and of their relative motion in the Jacobi coordinates.

Relative weights of configurations of the  ${}^8\text{Li}$  nucleus are given in Table 4. It can be seen from it that the maximal contribution to the  $\alpha-t-n$  model comes

from three components, by which we restrict ourselves in the calculation:

$$\Psi_{\lambda LS}^{JM_J}(\mathbf{r}, \mathbf{R}) = \Psi_{111}^{JM_J}(\mathbf{r}, \mathbf{R}) + \Psi_{1121}^{JM_J}(\mathbf{r}, \mathbf{R}) + \Psi_{3121}^{JM_J}(\mathbf{r}, \mathbf{R}). \quad (1.13)$$

### 1.3. The Wave Functions of the ${}^9\text{Li}$ and ${}^9\text{C}$ Nuclei

The  ${}^9\text{Li}$  and  ${}^9\text{C}$  nuclei in the ground state have the nonzero spin  $J^\pi = 3/2^-$  and among the nuclei of the  $1p$ -shell stand out because of nonstandard properties. The  ${}^9\text{Li}$  nucleus ( $\beta^-$ -unstable with a half life time of 0.18 s) is interesting as an exotic neutron-excess nucleus and as a core of the widely-investigated  ${}^{11}\text{Li}$  nucleus, when it is considered in the  ${}^9\text{Li}-n-n$  model. As it was shown in [22, 25, 31], the  $p^{11}\text{Li}$  elastic scattering is mainly determined by the proton scattering on the  ${}^9\text{Li}$  core and is barely sensitive to the low-density neutron halo extending over the limits of the  ${}^9\text{Li}$  core. The  ${}^9\text{C}$  nucleus ( $\beta^+$ -unstable with a half life time of 0.127 s) attracts substantial interest because of the large proton excess. It is interesting to note that the  ${}^8\text{B}$  nucleus, with a single excess proton, has a low energy threshold of proton separation  $E = 0.137$  MeV. The  ${}^9\text{C}$  nucleus with larger proton excess has, by the order, higher energy of proton separation  $E = 1.297$  MeV. It is obvious that clusterization and pairing of nucleons in the  ${}^9\text{C}$  nucleus compete with each other.

The accurate microscopic calculation of the WFs of the  ${}^9\text{Li}$  and  ${}^9\text{Be}$  nuclei is carried out in [64] using the quantum Monte Carlo method. The obtained many-body WFs were used in the calculation of static characteristics: binding energies, radii, quadrupole and magnetic moments, and energy spectrum of the excited states.

A density of the  ${}^9\text{Li}$  nucleus, when it is considered as a core of the widely-investigated  ${}^{11}\text{Li}$  nucleus, is typically estimated as the one-body density in the either Gaussian or oscillator form, which, although it reproduces the empirical rms radius, is insufficient in order to describe all its static characteristics. The more adequate method is the construction of the density of  ${}^9\text{Li}$  as a sum of the densities of its constituent clusters:  $\alpha$ -particle core, four neutrons in the  $p_{3/2}$ -shell with the zero spin, and a proton in the  $p_{3/2}$ -shell, as it is done in [150, 151]. The description of the rms matter radius of  ${}^9\text{Li}$  (2.32 fm) was a success, but the DCSs of proton scattering at  $E = 60$  MeV/nucleon, calculated in the optical model (taking into account the spin-orbit component of the optical potential), do not reproduce the experimental data for both  ${}^9\text{Li}$  and  ${}^{11}\text{Li}$ . It is concluded from this that the shell model with the oscillator potential describes the  ${}^9\text{Li}$  structure unrealistically.

The substantial progress in numerical methods of calculation of many-body systems is achieved as a result of using the high performance computers and development of new computational algorithms. For

example, in [49, 51, 64, 65] the WFs of the  ${}^9\text{Li}$  and  ${}^9\text{C}$  mirror nuclei are constructed in the multi-cluster  $\alpha-t-n-n$  and  $\alpha-{}^3\text{He}-p-p$  models within the stochastic variational method [49, 51] and quantum Monte Carlo method [64, 65] using the realistic two- or three-body potentials: Argonne (AV8, AV18), Urbana IX (UIX), Illinois (II1-II4). The four-cluster models of  ${}^9\text{Li}$  and  ${}^9\text{C}$  are formed by adding one nucleon to the three-cluster ones, which is their natural extension. This description automatically includes such configurations as  ${}^8\text{Li}-n$ ,  ${}^7\text{Li}-n-n$ , and  ${}^6\text{He}-t$  for  ${}^9\text{Li}$  and the appropriate mirror constituents for  ${}^9\text{C}$ . In this approach, the realistic  $NV$  forces are introduced and the solution is sought on the basis of trial functions, in which the two- and three-body correlations are taken into account. After optimization, these variational trial functions are used to input Green's functions in energy calculations using Monte Carlo method. The more complicated variational function can be constructed by including the two-body spin-orbit correlations and additional three-body correlations. However, the computation time required for taking into account these additional terms is substantial, whereas their contribution to the variational energy is relatively small. The two-body correlations are considered when the coupled differential equations are solved with the embedded variational parameters. It was found that the averaged parameters are close to the optimal ones which were used for light nuclei of the  $p$ -shell. These WFs reproduce all static nuclear characteristics, energies of the ground and nine excited states, and the cross section  $\sigma_{\text{reac}}$  of the  ${}^9\text{Li} + {}^{12}\text{C}$  reaction at 800 MeV/nucleon [65]. The model yields the total binding energy  $E = -33.7$  MeV when using the 18-parameter Argonne potential, while  $E_{\text{exp}} = -45.34$  MeV, the first excited state lies higher than the ground state by 0.7 MeV. Let us note that the 8-parameter Argonne potential describes the binding energy (for the ground state of  ${}^9\text{Li}$   $E = -36.6$  MeV [64]) somewhat better than the 18-parameter one, therefore all calculations were carried out later with the truncated 8-parameter one.

These facts indicate that even with the use of modern computers, the many-body problem cannot be solved rigorously and therefore there is room for model approaches.

In [123], the nuclear density of the  ${}^{6,8,9}\text{Li}$  isotopes is described by four phenomenological distributions in several models: SF (symmetrized Fermi), GH (Gaussian with halo), GG (Gaussian with Gauss, the first word relates to the distribution of nucleons in the core, the second one denotes the same in halo), GO (Gaussian with oscillator); all of them yield almost identically realistic values of the matter density of  ${}^9\text{Li}$  (differences are only observed for the smallest ( $r < 1$  fm) and large ( $r > 5.5$  fm) distances) and DCSs at  $E = 700$  MeV/nucleon. The difference, calculated here

**Table 5.** The interaction potentials, the considered WF configurations, and the static characteristics of the  ${}^9\text{Li}$  nucleus in the  ${}^7\text{Li}-n-n$  model obtained with them; experimental data:  $R_m = 2.44(6)$  fm [123],  $E_{7\text{Li}-n-n} = -6.096$  MeV [157],  $\mu = 3.44\mu_0$  [144, 157],  $Q = -27.4(1)$  mb [157]

Potential	${}^7\text{Li}-n-n$ model							
${}^7\text{Li}-n$	Deep attractive potential with forbidden states in the Buck <sup>a)</sup> form without exchange terms [149, 152]		Deep attractive potential with forbidden states in the Buck <sup>a)</sup> form with exchange terms with strong spin dependence [149, 152, 153]					
$n-n$	Model 1	Model 2	Model 3	Model 4				
Configuration	Volkov potential [149]	Hasegawa–Nagata potential [155] for odd waves, Afnan–Tang potential with repulsive core [156] for even waves	The same as in variant 2	The same as in variant 2				
$\lambda$	$l$	$L$	$S$	Configuration weight ( $P$ )				
0	0	0	3/2	0.025	0.051	0.984	0.654	
1	1	1	3/2	0.384	0.470	0.015	0.167	
2	2	1	3/2	0.199	0.246			
1	1	1	1/2	0.199	0.096	0.001	0.167	
2	2	1	1/2	0.103	0.050			
3	3	1	3/2	0.059	0.071			
3	3	1	1/2	0.030	0.014			
$R_m$ , fm	2.36		2.38		2.40		2.46	
$E$ , MeV	−8.89		−9.01		−6.20		−5.906	
$\mu, \mu_0$	0.93		0.94		1.31		1.33	
$Q$ , mb	−35.93		−40.0		−23.98		−27.93	

Note: <sup>a)</sup> Gaussian potential with central part  $V_0 = -46$  MeV,  $\alpha = 0.172$  fm<sup>−2</sup> for even waves,  $V_0 = -53$  MeV,  $\alpha = 0.172$  fm<sup>−2</sup> for odd waves and spin–orbit part  $V_0 = -10$  MeV.

too, between the proton and neutron radii (skin) for  ${}^9\text{Li}$  was 0.48 fm, which is in agreement with the value 0.42 fm [52], predicted in calculations using the stochastic variational method, and the value 0.53 fm [64], obtained using the quantum Monte Carlo method. For the  ${}^9\text{C}$  nucleus, the skin width calculated in [49] is 0.48 fm, which resulted from the large proton excess. Comparing the skin width predicted for other exotic nuclei (e.g., for  ${}^6,8\text{He}$ , where it reaches 0.8 fm), the authors [49] make a conclusion that the  ${}^9\text{Li}$  and  ${}^9\text{C}$  nuclei do not demonstrate the extended halo structure.

### 1.3.1. Choice of potentials of intercluster interactions and static characteristics of the ${}^9\text{Li}$ and ${}^9\text{C}$ nuclei.

For the  ${}^9\text{Li}$  nucleus, constructed in the  ${}^7\text{Li}-n-n$  model [149, 152, 153], at the heart of calculations were the pair deep  $n-n$  and  ${}^7\text{Li}-n$  potentials with FSs, the contribution of which is excluded by introduction of projectors in Hamiltonian, which creates the effective repulsion at small distances between the clusters, acting as a soft core. The applied potentials and the static characteristics calculated with them in the  ${}^7\text{Li}-n-n$  model are given in Table 5.

The potentials of  $NN$  interaction in the form of a sum of Gaussians, the same as for calculations of the structure of  ${}^6\text{He}-{}^6\text{Li}-{}^6\text{B}$  nuclei [68, 71], were used in the calculations. The Volkov potential [154] was chosen for simplicity in the first calculations. However, it did not contain the splitting in the total spin and poorly described all static characteristics, and further the Hasegawa–Nagata potential was used for odd waves [155] and the Afnan–Tang potential [156] for even waves (see Table 5).

As in the  ${}^7\text{Li}-n$  interaction, the deep attractive potential in the Buck [141] form was used, to which the exchange terms were added. The potential has one forbidden  $S$ -state. The Coulomb interaction was chosen in the standard form corresponding to either point interaction for the  $p-p$  case or the uniformly charged ball for the other interactions.

The deep attractive  ${}^7\text{Li}-n$  potential without exchange terms and two variants (1 and 2) of the  $n-n$  potential (Table 5) do not reproduce static characteristics of the  ${}^9\text{Li}$  nucleus. One of the methods for the three-body model improvement is to take into account the mixing of configurations in the nucleus (as it was

shown by the calculation for the  ${}^8\text{Li}$  nucleus, when the tensor forces were taken into consideration in the interaction potentials). Therefore the next step was the variation the  ${}^7\text{Li}-n$ -potential: the exchange terms with strong spin dependence were included in it (models 3 and 4 in Table 5). The basic configuration in this case will be  $\lambda/LS = 0003/2$ . The calculations performed with search for other configurations, distinguished from the basic one, showed that next in contribution should be the  $\lambda/LS = 1113/2$  and  $\lambda/LS = 1111/2$  configurations. However, the small admixture of states with  $\lambda/L \neq 0$  to the basic configuration does not yield the correct value of quadrupole moment (model 3 in Table 6). The correct weight distribution of the basic configuration and the additional ones is found in model 4, which resulted in the value of quadrupole moment in agreement with the experimental value.

Figures 7 and 8 show the density profiles (at the top) and isolines (at the bottom) of different components (from Table 5) for WFs of  ${}^9\text{Li}$  in of the model 6. The main peak of the state with the maximal weight  $\lambda/LS = 0003/2$  is at  $r = 2.5$  fm,  $R = 3.4$  fm, the second maximum (with the smaller amplitude) is at  $r = 4.3$  fm,  $R = 1.8$  fm (see Fig. 7). The effective WF extension (i.e., the range for which the WF does not yet become infinitesimal) in coordinate  $r$  is 6 fm, in coordinate  $R$  it is 5 fm. Here  $r$  is the coordinate of relative motion of two nucleons in  ${}^9\text{Li}$ ,  $R$  is the coordinate of relative motion of  ${}^7\text{Li}$  and the center-of-mass of two nucleons. Therefore the main maximum can be identified with the configuration when two nucleons are on the core surface close to one another (at a distance of 2.5 fm), which is similar to dineutron configuration, while the second maximum is like the figure with two nucleons are at a large distance from each other (4.3 fm), which is identified with the cigar-like configuration. The next in weight configurations  $\lambda/L = 111$  differs only in the  $S$  value ( $1/2$  и  $3/2$ ) (see Table 5), and since the value of the spin-orbit splitting is insignificant in this case (for the  $1p$ -shell), then these WF components are similar to each other and only one of them (with  $S = 1/2$ ) is given in Fig. 8. Here the WF is also localized in two maxima with the coordinates  $r = 2.3$  fm,  $R = 2.3$  fm and  $r = 4.3$  fm,  $R = 1.2$  fm; the first maximum corresponds to the component, for which all three particles are located at vertices of the triangle close to the isosceles triangle, the second maximum is appropriate to the component close to the cigar-like. This WF component in coordinate  $r$  is extended to 8 fm, whereas in coordinate  $R$  its extension is less than 4 fm, which demonstrates the large extension of the neutron matter. The difference between the  $\lambda/LS = 0003/2$  (see Fig. 7) and  $\lambda/LS = 1111/2$  (see Fig. 8) configurations is that the nucleus in the first configuration is in the dineutron state, while in the second configuration the nucleus is in the state close to the cigar-like state, to which the relation of WF density maxima corre-

**Table 6.** The interaction potentials, the considered WF configurations and their weights for the  ${}^9\text{B}$  nucleus in  ${}^7\text{Be}-p-p$  model

Potential	
${}^7\text{Be}-p$	Deep attractive potential with forbidden states in the Buck form, the same as for ${}^7\text{Li} + n$ in models 3 and 4 in Table 5
$p-p$	Hasegawa-Nagata potential [155] for odd waves, Afnan-Tang potential with repulsive core [156] for even waves
Configuration	Configuration weight
$\lambda \quad l \quad L \quad S$	
0 0 0 3/2	0.714
2 2 0 3/2	0.013
1 1 1 1/2	0.136
1 1 1 3/2	0.136

sponds: the maximum in Fig. 8, more distant from the coordinate origin, is larger in magnitude than the first maximum, while the relation of maxima in Fig. 7 is reverse. As is shown in [152], where the WF is calculated with four types of intercluster interaction potentials, only the WF that is obtained in the Buck potential, in which the spin-dependent terms are included (models 3 and 4 in Table 5), provides the most adequate description of static characteristics of the  ${}^9\text{Li}$  nucleus. The calculation with the WFs constructed with other potentials resulted in quadrupole ( $Q$ ) and magnetic ( $\mu$ ) moments, in poor agreement with experimental data [157].

Since the mirror  ${}^9\text{Li}$  and  ${}^9\text{C}$  systems differ only in the Coulomb interaction, then the same effective  ${}^7\text{Li}-n$  interaction is used in the calculation, i.e., for  ${}^9\text{C}$  the potential nuclear part is chosen the same as for  ${}^9\text{Li}$ , but with consideration for the Coulomb interaction.

Three basic  $\lambda/LS = 0003/2$ ,  $\lambda/LS = 1111/2$ , and  $\lambda/LS = 1113/2$  components of the WF of  ${}^9\text{C}$  (Table 6) are close to the analogous components of the WF of  ${}^9\text{Li}$ , which were considered above. The distinction is that the contribution from the  $\lambda/LS = 0003/2$  configuration to the WF of the  ${}^9\text{Li}$  nucleus exceeds the corresponding contribution in the  ${}^9\text{Li}$  nucleus by 5%, the contribution of the  $\lambda/LS = 1111/2$  to  ${}^9\text{Li}$  is 3% smaller than to  ${}^9\text{Li}$ . It is known that the relation of contributions from configurations is determined by nondiagonal matrix elements of Hamiltonian. The Coulomb interaction somewhat increases this overlap, which results in the larger WF localization on the periphery

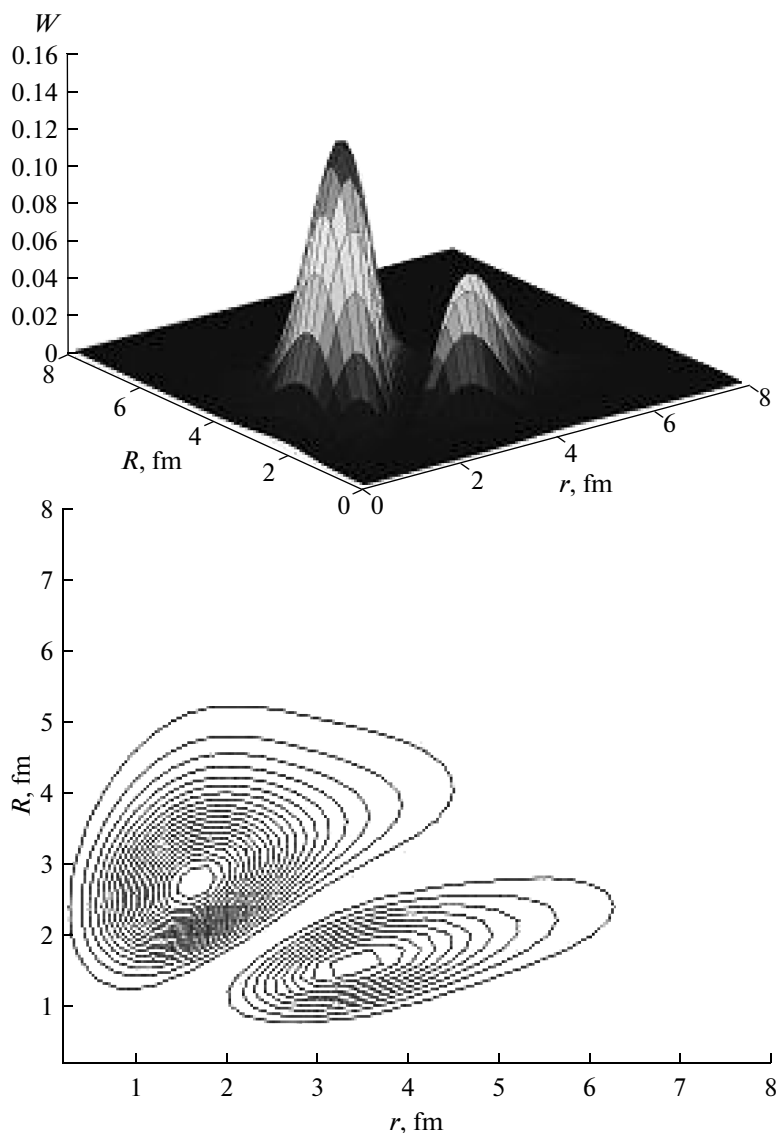


**Fig. 7.** The density profiles (at the top) and isolines (at the bottom) of WFs of the  ${}^9\text{Li}$  nucleus of configuration with  $\lambda/LS = 0003/2$  in model 6 (Table 5).

and this effect for configurations with small orbital angular momenta  $l$  and  $l$  proved to be significant.

Let us consider the component  $\lambda/LS = 2203/2$ , presented in Fig. 9. The WF density in it is concentrated in three peaks with the coordinates:  $r = 1.3$  fm,  $R = 2.3$  fm;  $r = 3.1$  fm,  $R = 2.0$  fm;  $r = 4.9$  fm,  $R = 1.0$  fm. In the first maximum, two protons are at minimal distance from one another; in the third maximum they are at maximal distance (it is most close to the cigar-like configuration). The weight of this component is small (0.013), accordingly small is its contribution to the calculation of static characteristics.

The comparison [49] of the  ${}^9\text{Li}$  density distribution in the multicluster model with that in the purely shell model, calculated in the harmonic-oscillator potential, shows that the density in the harmonic-oscillator

potential drops very fast near the nuclear surface, whereas in the multicluster model it is more extended, with the tail slowly dying out, which is also confirmed in our calculations.

The comparison of static characteristics following the results of published works for  ${}^9\text{Li}$  is presented in Table 7. It can be seen that values calculated with the four-body WFs, obtained using the stochastic variational method [49, 52] and the quantum Monte Carlo method [64], are approximately identical and close to experimental values. Our calculation with the three-body WFs [149, 152, 153] in model 1 correctly reproduces only the rms  $R_m$ ; in model 4, the agreement is achieved also for  $Q$ , but the magnetic moment is smaller than the experimental value by a factor of 2.5, which is the evidence that the contribution of the

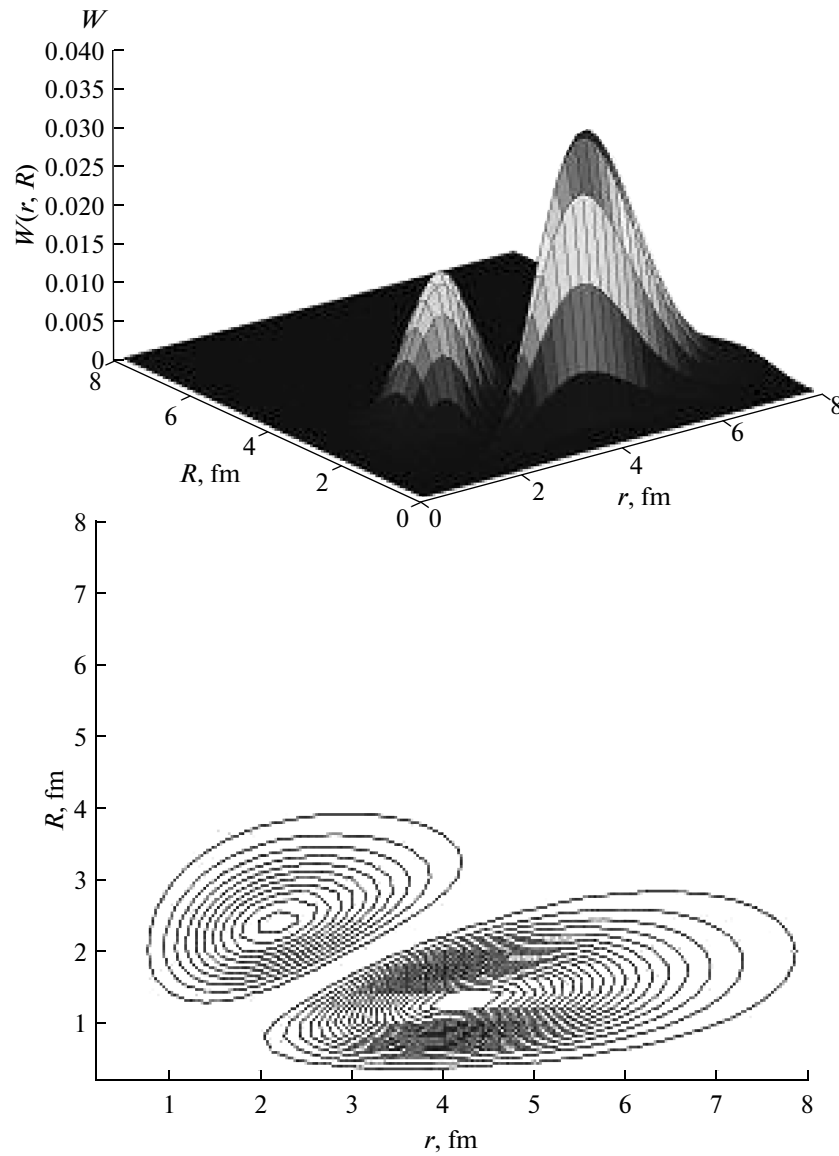


Fig. 8. The same as in Fig. 7 for configuration with  $\lambda/LS = 1111/2$ .

inside of the nucleus, though this calculation is performed with the WF, calculated in the Buck attractive potential, in which the WF does not vanish out inside the nucleus as in the potential with the repulsive core.

For the  ${}^9\text{C}$  nucleus, only  $R_m$  and  $\mu$  are experimentally measured (Table 8). The values calculated in [49] are in agreement with the experimental data; the large proton radius and quadrupole moment of this nucleus

Table 7. Characteristics of the  ${}^9\text{Li}$  nucleus according to the results of published works

Characteristics	Experiment	[49, 52]	[64] IL4	[64] AV8	[149, 152] ${}^7\text{Li} + n + n$ Model 2	[149, 152] ${}^7\text{Li} + n + n$ Model 4
$r_p$ , fm	2.18 [3] 2.24 [148]	2.10	1.94(1)	2.19(2)		
$r_n$ , fm	2.39 [3]	2.52	2.39(1)	2.72(1)		
$r_{rms}$ , fm	2.32 [3] 2.44(6) [123]	2.39			2.38	2.46
$Q$ , fm <sup>2</sup>	-2.74 [157]	-2.74	-2.5(1)	-3.1(1)	-4.0	-2.79
$\mu$ , ( $\mu_0$ )	3.44 [157]	3.43	2.54(2)	2.91(1)	0.94	1.33

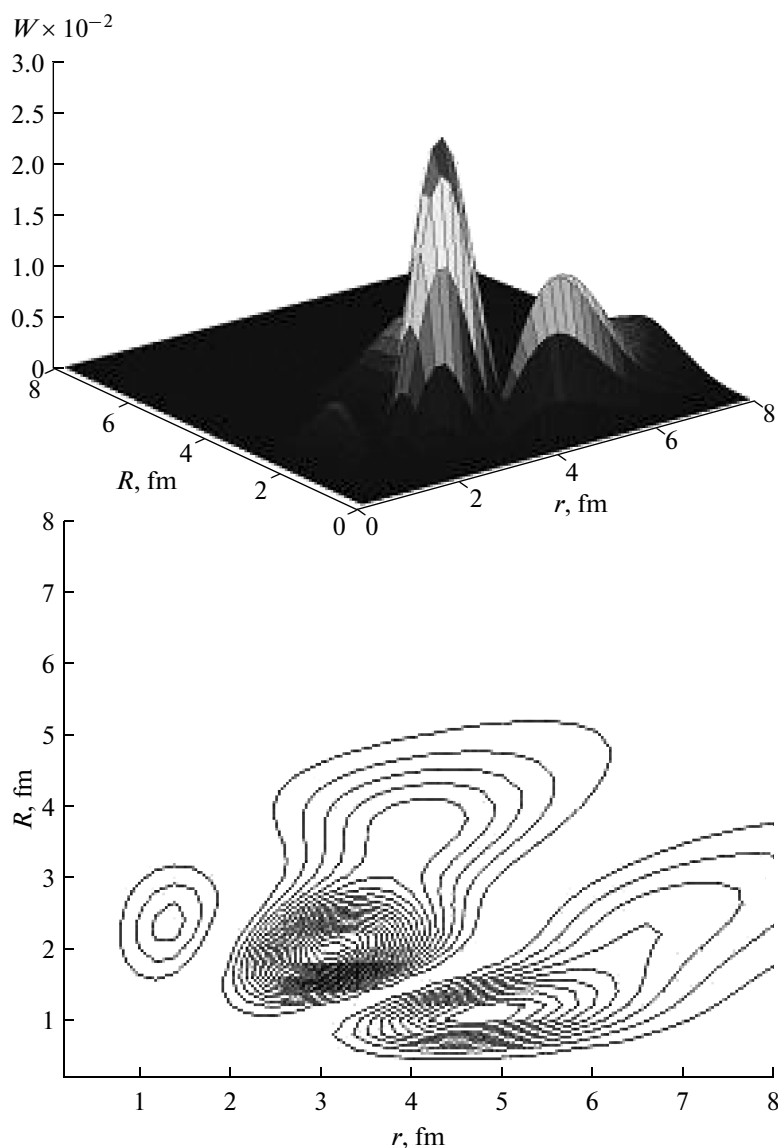


**Fig. 9.** The density profiles (at the top) and isolines (at the bottom) of WFs of the  ${}^9\text{C}$  nucleus of configuration with  $\lambda ILS = 2203/2$ .

are predicted there as well. The magnetic moment calculated in [64] with the AV8 potential is close to the experimental value, while calculated with the IL4

potential, it is twice as small. Our calculation, correctly describing  $R_m$ , underestimates the magnetic moment almost by a factor of 2.5, which is explained by the same reason as for the  ${}^9\text{Li}$  nucleus.

**Table 8.** Characteristics of the  ${}^9\text{C}$  nucleus according to the results of published works

Characteristics	Experiment [157]	[49]	[64] IL4	[64] AV8	[153]
$r_p$ , fm		2.64			
$r_n$ , fm		2.16			
$r_{rms}$ , fm	2.42	2.50			2.47
$Q$ , mb		-50.4			-31.5
$\mu$ , ( $\mu_0$ )	-1.39	-1.5	-0.70(4)	-1.08(3)	-0.6

In the three-body  $\alpha-t-2n$  model of the  ${}^9\text{Li}$  nucleus, three  $\lambda ILS$  configurations have been taken into account; however, the binding energy in the channel and the quadrupole moment are in poor agreement with experimental data (see Table 9). In this case, no reasonable variations in potential parameters could reproduce the quadrupole moment. This may be evidence that the chosen configuration is inadequate to the real structure of the  ${}^9\text{Li}$  nucleus. Let us note, however, that a weight of the  $\alpha-t-2n$  configuration in MBMS exceeds 80% [53].

In the calculations, the potentials of  $\alpha-t$  interaction of Gaussian shape [139] were applied, which were previously used for calculation of the  ${}^8\text{Li}$  nucleus structure. Since there were no data on the  $\alpha-2n$  and  $t-2n$  interactions existing, the potentials of the  $\alpha-2n$  and  $t-2n$  subsystems were constructed on the basis of the  $\alpha-n$  and  $t-n$  interactions. In order to optimize the selection of parameters of interaction potentials, we attempted to construct a potential based on the bound state of the  ${}^6\text{He}\alpha-2n$  system and the simplest folding-potential  $\alpha-(2n)$ , where the resonant WF of the  $2n$  system was used. The WFs of the  ${}^5\text{He}t-n-n$  system have been also calculated. Unfortunately, the obtained potentials did not correspond to any real systems. Therefore, at the  $\alpha-n$  and  $t-n$  interactions we applied the potentials of Gaussian shape, containing spin-orbit interaction, which were already used for calculations of the  ${}^8\text{Li}$  nucleus structure [139, 140, 149]. By varying the potential depth, we chose the following parameters:  $V_{\alpha-2n} = CV_{\alpha-n}$ , where  $2 > C > 1$  is the varied parameter.  $V_0 = -20$  MeV,  $\alpha = 0.11$  fm $^{-2}$ ;  $V_{t-2n} = CV_{t-n}$ , where  $2 > C > 1$  is the varied parameter;  $V_0 = -40$  MeV,  $\alpha = 0.38$  fm $^{-2}$  for even waves;  $V_0 = -40$  MeV,  $\alpha = 0.19$  fm $^{-2}$  for odd waves.

The wave function of the ground state of the  ${}^9\text{Li}$  nucleus has the negative parity. The clusters  $\alpha$  and  $t$  are believed unexcited and have the positive parity. Here, for the WF of dineutron with isospin  $T = 1$ , two cases are possible: either  $\tilde{L}\tilde{S}\tilde{T} = 001$  or  $\tilde{L}\tilde{S}\tilde{T} = 111$ . The preliminary WF calculations showed [149] that the energy of the state with the  $\tilde{L}\tilde{S}\tilde{T} = 001$  configuration lies below the state with  $\tilde{L}\tilde{S}\tilde{T} = 111$ . It follows from the fact that if the relative orbital angular momentum of the  $n-n$  system is 1, that the potentials of the  $\alpha-2n$  and  $t-2n$  interactions have one forbidden  $S$ -state. If the orbital angular momentum is zero, there are two forbidden states in  $S$ - and  $D$ -waves. Therefore, the calculations were carried out with usage of dineutron configurations alone with  $\tilde{L}\tilde{S} = 11$ .

Based on Eqs. (1.1) and (1.2), we write down the WFs of the  ${}^9\text{Li}$  nucleus with the total angular momentum  $J = 3/2$  and its projection  $M_J$  in the  ${}^7\text{Li}-n-n$  model:

$$\Psi_{i,f}^{JM_J} = \Psi_{7\text{Li}}(\mathbf{R}_{7\text{Li}})\varphi_n(\mathbf{r}_1)\varphi_n(\mathbf{r}_2) \sum_{\lambda L S} \Psi_{\lambda L S}^{JM_J}(\mathbf{r}, \mathbf{R}), \quad (1.14)$$

where  $\Psi_{7\text{Li}}(\mathbf{R}_{7\text{Li}})$ ,  $\varphi_n(\mathbf{r}_1)$ ,  $\varphi_n(\mathbf{r}_2)$  and  $\Psi_{\lambda L S}^{JM_J}(\mathbf{r}, \mathbf{R})$  are the WFs of  ${}^7\text{Li}$ , two neutrons, and the relative motion in the Jacobi coordinates. According to Table 5, the WF of relative motion in model 4 will consist of three components:

$$\begin{aligned} \Psi_{\lambda L S}^{JM_J}(\mathbf{r}, \mathbf{R}) &= \Psi_{0003/2}^{JM_J}(\mathbf{r}, \mathbf{R}) \\ &+ \Psi_{1113/2}^{JM_J}(\mathbf{r}, \mathbf{R}) + \Psi_{1111/2}^{JM_J}(\mathbf{r}, \mathbf{R}). \end{aligned} \quad (1.15)$$

**Table 9.** The interaction potentials, the considered WF configurations, and static characteristics of the  ${}^9\text{Li}$  nucleus in the  $\alpha-t-2n$  model obtained with them

Potential	Model 1	Model 2
$\alpha-t$	Gaussian potential, the same as in Table 4, model 1	Gaussian potential in the Buck form, the same as in Table 4, model 3
$\alpha-2n$	Potential, constructed on the basis of the Gaussian $\alpha-n$	The same as in model 1
$t-2n$	Potential, constructed on the basis of the Gaussian $t-n$	The same as in model 1
Configuration	Configuration weight ( $P$ )	
$\lambda \quad l \quad L \quad S$		
2 1 2 1/2	0.555	0.745
1 2 2 1/2	0.201	0.124
3 2 2 1/2	0.201	0.124
Static characteristics		
$R_m$ , fm	2.38	2.35
$E^b$ , MeV	-9.274	-8.998
$\mu, \mu_0$	3.38	3.50
$Q$ , mb	-16.75	-17.4

Note: <sup>b)</sup> The experimental binding energy in the channel in  $\alpha-t-2n$   $E_{\alpha-t-2n} = -8.563$  MeV [157].

The wave function in the  $\alpha-t-2n$  model

$$\Psi_{i,f}^{JM_J} = \Psi_{\alpha}(\mathbf{R}_{\alpha})\Psi_t(\mathbf{r}_1\mathbf{r}_2\mathbf{r}_3)\varphi_{2n}(\mathbf{r}_4\mathbf{r}_5) \sum_{\lambda L S} \Psi_{\lambda L S}^{JM_J}(\mathbf{r}, \mathbf{R}), \quad (1.16)$$

where  $\Psi_{\alpha}(\mathbf{R}_{\alpha})$ ,  $\Psi_t(\mathbf{r}_1\mathbf{r}_2\mathbf{r}_3)$ ,  $\varphi_{2n}(\mathbf{r}_4\mathbf{r}_5)$ ,  $\Psi_{\lambda L S}^{JM_J}(\mathbf{r}, \mathbf{R})$  are the WFs of the  $\alpha$ -particle, triton ( $t$ ), dineutron ( $2n$ ) and the relative motion in the Jacobi coordinates. According to Table 9, the contribution to  $\Psi_{\lambda L S}^{JM_J}(\mathbf{r}, \mathbf{R})$  will be made by the following components:

$$\begin{aligned} \Psi_{\lambda L S}^{JM_J}(\mathbf{r}, \mathbf{R}) &= \Psi_{2121/2}^{JM_J}(\mathbf{r}, \mathbf{R}) \\ &+ \Psi_{1221/2}^{JM_J}(\mathbf{r}, \mathbf{R}) + \Psi_{3221/2}^{JM_J}(\mathbf{r}, \mathbf{R}) \end{aligned} \quad (1.17)$$

## 2. MATHEMATICAL APPARATUS AND ANALYSIS OF RESULTS

### 2.1. The Calculation of Matrix Element of Elastic Scattering

In line with the Glauber multiple scattering diffraction theory, an amplitude of proton elastic scattering by a compound nucleus with mass  $A$  can be written,

according to [88], as an integral over the impact parameter  $\mathbf{c}_\perp$ :

$$M_{if}(\mathbf{q}_\perp) = \sum_{M_j} \frac{ik}{2\pi} \times \int d\mathbf{c}_\perp d\mathbf{R}_A \exp(i\mathbf{q}_\perp \mathbf{c}_\perp) \delta(\mathbf{R}_A) \langle \Psi_i^{JM_j} | \Omega | \Psi_f^{JM_j'} \rangle, \quad (2.1)$$

where the index “ $\perp$ ” denotes two-dimensional vectors lying in the plane perpendicular to the direction of the incident beam,  $\langle \Psi_i^{JM_j} | \Omega | \Psi_f^{JM_j'} \rangle$  is the matrix element of transfer from the initial state  $\Psi_i^{JM_j}$  to the final state of nucleus under action of the operator  $\Omega$ , in case of elastic scattering  $\Psi_i^{JM_j} = \Psi_f^{JM_j'}$ ;  $\mathbf{R}_A = \frac{1}{A} \sum_{n=1}^A \mathbf{r}_n$  is the coordinate of the nucleus center-of-mass;  $\mathbf{k}$  is the momentum of incident particles in the center-of-mass system;  $q = 2k \sin \frac{\theta}{2}$  is the momentum transferred in reaction;  $\theta$  is the scattering angle.

The operator  $\Omega$  is written as a series of multiple scattering:

$$\Omega = 1 - \prod_{v=1}^A (1 - \omega_v(\mathbf{c}_\perp - \mathbf{c}_{\perp v})) = \sum_{v=1}^A \omega_v - \sum_{v < \mu} \omega_v \omega_\mu + \sum_{v < \mu < \eta} \omega_v \omega_\mu \omega_\eta + \dots (-1)^{A-1} \omega_1 \omega_2 \dots \omega_A, \quad (2.2)$$

where  $\mathbf{c}_{\perp v}$  is the two-dimensional analog of three-dimensional one-body coordinates of nucleons  $\mathbf{r}_v$ . For definiteness, let us carry out the matrix element calculation for the  ${}^6\text{He}$  nucleus presented in the  $\alpha$ - $n$ - $n$  models. We rewrite operator (2.2) in the optional form based on the fact that the scattering takes place on  $\alpha$ -particle and two neutrons, composing the  ${}^6\text{He}$  nucleus:

$$\Omega = \Omega_\alpha + \Omega_n + \Omega_n - \Omega_\alpha \Omega_n - \Omega_\alpha \Omega_n - \Omega_n \Omega_n + \Omega_\alpha \Omega_n \Omega_n, \quad (2.3)$$

where each operator is expressed through the profile functions  $\omega_v$  as follows:

$$\Omega_\alpha = \omega_v(\mathbf{c}_\perp - \mathbf{R}_{\perp\alpha}) = \frac{1}{2\pi ik} \int d\mathbf{q}_\perp \exp(-i\mathbf{q}_\perp (\mathbf{c}_\perp - \mathbf{R}_{\perp\alpha})) f_{p\alpha}(q), \quad (2.4)$$

$$\Omega_n = \omega_n(\mathbf{c}_\perp - \mathbf{c}_v) = \frac{1}{2\pi ik} \int d\mathbf{q}_\perp \exp(-i\mathbf{q}_\perp (\mathbf{c}_\perp - \mathbf{c}_v)) f_{pn}(q). \quad (2.5)$$

As can be seen from Eqs. (2.3) and (2.4),  $\alpha$ -particle in our calculation is assumed structureless so the scattering is to be considered on one particle. The compound nature of  $\alpha$ -particle is taken into account dynamically when the potential with FSs is used in the

$\alpha$ - $n$  interaction. The central part of the elementary  $f_{pn}^c(q)$  amplitude is written down in a standard way:

$$f_{pn}^c(q) = \frac{k\sigma_{pn}^c}{4\pi} (i + \varepsilon_{pn}^c) \exp\left(-\frac{(\beta_{pn}^c q)^2}{2}\right), \quad (2.6)$$

$f_{p\alpha}^c(q)$  is written down analogously with the index substitution  $n \rightarrow \alpha$ . The parameters of the elementary procedure  $\sigma_{pn}^c$ ,  $\varepsilon_{pn}^c$ ,  $\beta_{pn}^c$  are the input parameters of the theory, but they are determined from independent experiments. Parameters of the  $pN$ -amplitude at  $E = 0.7$  and  $0.07$  GeV/nucleon are taken the same as in [113]. Parameters of the  $p\alpha$ -amplitude are borrowed from [158–160].

In order to calculate matrix element (2.1), one has to substitute WFs (1.7)–(1.10) and operator (2.3)–(2.5) in it and integrate over all variables, on which the integrand depends. However, it is necessary beforehand to pass in the operator  $\Omega$  and in the WFs from one-body coordinates (they are shown in Fig. 1 by dashed lines) to the relative, i.e., Jacobi coordinates (in Fig.1, they are shown by solid lines), on which  $\Psi^{JM_j}(\mathbf{r}, \mathbf{R})$  depends. The relation between the one-body and relative coordinates is as follows:

$$\begin{aligned} \mathbf{r}_1 &= \frac{2}{3}\mathbf{R} + \frac{1}{2}\mathbf{r} + \mathbf{R}_6, & \mathbf{r}_2 &= \frac{2}{3}\mathbf{R} - \frac{1}{2}\mathbf{r} + \mathbf{R}_6, \\ \mathbf{r}_3 &= \mathbf{R}_6 - \frac{1}{3}\mathbf{R}, & \mathbf{R}_6 &= \frac{1}{6} \sum_{i=1}^6 \mathbf{r}_i. \end{aligned} \quad (2.7)$$

Substituting in (2.5) elementary amplitude (2.6), we shall integrate over  $d\mathbf{q}_\perp$ :

$$\Omega_n = \omega_n(\mathbf{c}_\perp - \mathbf{c}_v) = F_n \exp(-(\mathbf{c} - \mathbf{c}_v)^2 \eta_n), \quad (2.8)$$

where

$$F_n = \frac{\sigma_{pN}^c}{4\pi(\beta_{pN}^c)^2} (1 - i\varepsilon_{pN}^c), \quad \eta_n = \frac{1}{2(\beta_{pN}^c)^2}. \quad (2.9)$$

Analogously for  $\Omega_\alpha$  with the index substitution  $n \rightarrow \alpha$ .

Then, changing over from the one-body coordinates to the relative ones and performing certain transformations, we can write down operator (2.3) as follows:

$$\begin{aligned} \Omega &= \sum_{k=1}^7 g_k \exp(-a_k \mathbf{c}_\perp^2 - b_k \mathbf{R}_\perp^2 \\ &\quad - c_k \mathbf{r}_\perp^2 d_k \mathbf{c}_\perp \mathbf{R}_\perp + e_k \mathbf{c}_\perp \mathbf{r}_\perp + h_k \mathbf{R}_\perp \mathbf{r}_\perp), \end{aligned} \quad (2.10)$$

the summation in  $k$  means summation by the scattering multiplicities:  $k = 1-3$  is the single collision,  $k = 4-6$  is the double collision,  $k = 7$  is the triple collision; the index “ $\perp$ ” denote two-dimensional vectors (lying

in the plane  $xy$ , perpendicular to the axis  $z$ , along which the impinging particles are moving). Here

$$g_k = (F_n, F_n, F_\alpha, -F_n F_n, -F_n F_\alpha, -F_n F_\alpha, F_n F_n F_\alpha),$$

$$a_k = (\eta_n, \eta_n, \eta_\alpha, 2\eta_n, (\eta_n + \eta_\alpha), (\eta_n + \eta_\alpha), (2\eta_n + \eta_\alpha)),$$

$$b_k = \left( \frac{4}{9}\eta_n, \frac{4}{9}\eta_n, \frac{1}{9}\eta_\alpha, \frac{8}{9}\eta_n, \left( \frac{4}{9}\eta_n + \frac{1}{9}\eta_\alpha \right), \right. \\ \left. \left( \frac{4}{9}\eta_n + \frac{1}{9}\eta_\alpha \right), \left( \frac{8}{9}\eta_n + \frac{1}{9}\eta_\alpha \right) \right),$$

$$c_k = \left( \frac{1}{4}\eta_n, \frac{1}{4}\eta_n, 0, \frac{1}{2}\eta_n, \frac{1}{4}\eta_n, \frac{1}{4}\eta_n, \frac{1}{2}\eta_n \right),$$

$$d_k = \left( \frac{4}{3}\eta_n, \frac{4}{3}\eta_n, -\frac{2}{3}\eta_\alpha, \frac{8}{3}\eta_n, \left( \frac{4}{3}\eta_n - \frac{2}{3}\eta_\alpha \right), \right. \\ \left. \left( \frac{4}{3}\eta_n - \frac{2}{3}\eta_\alpha \right), \left( \frac{8}{3}\eta_n - \frac{2}{3}\eta_\alpha \right) \right),$$

$$e_k = (\eta_n, -\eta_n, 0, 0, \eta_n, -\eta_n, 0),$$

$$h_k = \left( -\frac{2}{3}\eta_n, \frac{2}{3}\eta_n, 0, 0, -\frac{2}{3}\eta_n, \frac{2}{3}\eta_n, 0 \right),$$

where  $F_n, \eta_n$  are defined by Eq. (2.9) and depend on parameters of the elementary  $f_{pn}^c(q)$  amplitude,  $F_\alpha, \eta_\alpha$  are written down analogously, with substitution of  $\alpha$  for  $n$ , and depend on parameters of the elementary  $f_{p\alpha}^c(q)$  amplitude.

Substituting in (2.1) WFs (1.7) and (1.8), we write down the matrix element

$$M_{if}(\mathbf{q}_\perp) = M0_{if}(\mathbf{q}_\perp) + M1_{if}(\mathbf{q}_\perp) + M2_{if}(\mathbf{q}_\perp), \quad (2.11)$$

where

$$M0_{if}(\mathbf{q}_\perp) \quad (2.12)$$

$$= \sum_{M_s M'_s} \frac{ik}{2\pi} \int d\mathbf{c}_\perp d\mathbf{R}_6 \exp(i\mathbf{q}_\perp \mathbf{c}_\perp) \delta(\mathbf{R}_6) \langle \Psi_{000} | \Omega | \Psi_{000} \rangle,$$

$$M1_{if}(\mathbf{q}_\perp) \quad (2.13)$$

$$= \sum_{M_s M'_s} \frac{ik}{2\pi} \int d\mathbf{c}_\perp d\mathbf{R}_6 \exp(i\mathbf{q}_\perp \mathbf{c}_\perp) \delta(\mathbf{R}_6) \langle \Psi_{111} | \Omega | \Psi_{111} \rangle,$$

$$M2_{if}(\mathbf{q}_\perp) = \sum_{M_j M'_j} \frac{ik}{2\pi} \int d\mathbf{c}_\perp d\mathbf{R}_6 \exp(i\mathbf{q}_\perp \mathbf{c}_\perp) \delta(\mathbf{R}_6) \\ \times \{ \langle \Psi_{000} | \Omega | \Psi_{111} \rangle + \langle \Psi_{111} | \Omega | \Psi_{000} \rangle \}. \quad (2.14)$$

Using the explicit form of WFs (1.9) and (1.10), we can see that all matrix elements can be calculated analytically because WF and operator (2.10) are written down as expansions in Gaussians. Matrix elements (2.12)–(2.14) are calculated in the Cartesian coordinate system because the coordinates of the same name in WFs are three-dimensional, while in operator  $\Omega$  they are two-dimensional (denoted by the index “ $\perp$ ”).

Let us give the example of  $M1_{if}(\mathbf{q}_\perp)$  calculation. We shall substitute in (2.13) WF (1.9):

$$M1_{if}(\mathbf{q}_\perp) = \frac{ik}{6\pi} \sum_{ijj'} C_{ij}^{(11)} C_{ij'}^{(11)} \sum_{mm'\mu\mu'} (-1)^{M_L+M'_L} \langle 1m1\mu | 1M_L \rangle \\ \times \langle 1m'1\mu' | 1M'_L \rangle \int d\mathbf{c}_\perp \exp(i\mathbf{q}_\perp \mathbf{c}_\perp) \quad (2.15)$$

$$\times \langle (-\alpha_i r - \beta_j R) | \Omega | \exp(-\alpha_i r - \beta_j R) \rangle \langle RY_{1m}(\hat{\mathbf{R}}) | RY_{1m'}(\hat{\mathbf{R}}) \rangle \\ \times \langle rY_{1\mu}(\hat{\mathbf{r}}) | rY_{1\mu'}(\hat{\mathbf{r}}) \rangle.$$

Integration over  $d\mathbf{R}_6$  is performed using  $\delta$ -function in passing from the one-body coordinates in WF to the Jacobi coordinates using Eq. (2.7). In order to integrate this expression over coordinates  $\mathbf{r}$  and  $\mathbf{R}$  in the Cartesian coordinate system, we pass from the spatial spherical harmonics to polynomials using the formula [161]

$$R^l Y_{lm}(\hat{\mathbf{R}}) = \sqrt{\frac{2l+1}{4\pi}} (l+m)!(l-m)! \\ \times \sum_{u,v,w} \frac{1}{p!t!k!} \left( -\frac{R_x + iR_y}{2} \right)^p \left( \frac{R_x - iR_y}{2} \right)^t R_z^k, \quad (2.16)$$

where  $p, t, k$  are positive integers:  $p+t+k=l, p-t=m$ ;  $R_x, R_y, R_z$  are projections of vector  $\mathbf{R}$  onto axes of the Cartesian coordinate system.

Summing in (2.15) the terms depending on projections of momenta, with consideration for (2.16), we derive the following polynomial:

$$\sum_{mm'\mu\mu'} (-1)^{M_L+M'_L} \langle 1m1\mu | 1M_L \rangle \langle 1m'1\mu' | 1M'_L \rangle \\ \times \langle RY_{1m}(\hat{\mathbf{R}}) | RY_{1m'}(\hat{\mathbf{R}}) \rangle \langle rY_{1\mu}(\hat{\mathbf{r}}) | rY_{1\mu'}(\hat{\mathbf{r}}) \rangle \quad (2.17)$$

$$= R_x^2(r_y^2 + r_z^2) + R_y^2 r_x^2 - 2R_x r_x (R_y r_y - R_z r_z) + 2R_z^2 r_x^2.$$

Substituting in (2.15) operator  $\Omega$  (2.10) and polynomial (2.17) and separating the variables, we write down

$$M1_{if}(\mathbf{q}_\perp) = \frac{ik}{6\pi} \sum_{ijj'} C_{ij}^{(11)} C_{ij'}^{(11)} \sum_{k=1}^7 g_k \{ I_x^{(2)}(q_x) I_y(q_y) I_x(q_x) \\ \times I_y^{(2)}(q_y) I_z + I_x^{(2)}(q_x) I_y(q_y) I_x(q_x) I_y(q_y) I_z^{(2)} \\ + I_x(q_x) I_y(q_y) I_y^{(2)}(q_y) I_x^{(2)}(q_x) I_z \\ - 2I_x^{(11)}(q_x) I_y^{(11)}(q_y) I_z + 2I_x(q_x) I_y(q_y) I_x^{(2)}(q_x) I_y(q_y) I_z^{(2)} \}, \quad (2.18)$$

where the following designations are introduced:

$$I_z = \int_{-\infty}^{\infty} dR_z dr_z \exp(-\beta_{jj'} R_z^2 - \alpha_{ii'} r_z^2), \\ I_z^{(2)} = \int_{-\infty}^{\infty} dR_z dr_z R_z^2 \exp(-\beta_{jj'} R_z^2 - \alpha_{ii'} r_z^2),$$

$$I_x(q_x) = \int_{-\infty}^{\infty} d\rho_x dR_x dr_x \exp(-a_k \rho_x^2 - b_{kj} R_x^2 - c_{ki} r_x^2 + d_k \rho_x R_x + e_k \rho_x r_x + h_k R_x r_x + i q_x \rho_x),$$

$$I_x^{(n,m)}(q_x) = \int_{-\infty}^{\infty} d\rho_x dR_x dr_x R_x^n r_x^m \exp(-a_k \rho_x^2 - b_{kj} R_x^2 - c_{ki} r_x^2 + d_k \rho_x R_x + e_k \rho_x r_x + h_k R_x r_x + i q_x \rho_x),$$

where

$$\alpha_{ii'} = \alpha_i + \alpha_{i'}, \quad \beta_{jj'} = \beta_j + \beta_{j'},$$

$$b_{kj} = b_k + \beta_{jj'}, \quad c_{ki} = c_k + \alpha_{ii'}.$$

The variables  $r_x, r_y, R_x, R_y$  enter in matrix element (2.18) symmetrically, therefore integrals over  $y$  are written down analogously. These are integrals of the Euler–Poisson type, which are easily calculated analytically [162]. Here it is important to note that with this approach (writing down the WFs and operators as expansions in Gaussians) it is possible to calculate all matrix elements analytically without any simplifications and, consequently, without accuracy loss as well. The further calculation was carried out using a computer.

In order to calculate the polarization characteristics, it is necessary to take into account in the elementary amplitude not only the central term  $f_{px}^c(q)$  (2.6) but also the spin–orbit term  $f_{px}^s(q)$ , after which the amplitude will be written as

$$f_{px}(q) = f_{px}^c(q) + f_{px}^s(q) \mathbf{y} \cdot \mathbf{n}. \quad (2.19)$$

The spin part of the amplitude is parameterized as follows:

$$f_{px}^s = \frac{k\sigma_{px}^s}{4\pi} q D_s \left( i + \varepsilon_{px}^s \right) \exp\left( -\frac{(\beta_{px}^s q)^2}{2} \right), \quad (2.20)$$

where index  $x = n, \alpha$ . Parameters of spin–orbit amplitudes for  $f_{px}^s(q)$  were taken from [159, 160], for  $f_{px}^c(q)$  they were borrowed from [159, 163].

Now operator  $\Omega$  (2.10), which depends on elementary  $px$ -amplitudes according to the dividing each of them in the sum of the central and spin–orbit components, will also present a sum of two terms:

$$\Omega = \Omega^- + \Omega^s. \quad (2.21)$$

The matrix element of scattering with consideration for the spin dependence can be written as follows:

$$M_{if}(\mathbf{q}_\perp) = M_{if}^c(\mathbf{q}_\perp) + M_{if}^s(\mathbf{q}_\perp). \quad (2.22)$$

The differential cross section is a square of the matrix element modulus:

$$\frac{d\sigma}{d\Omega} = \frac{1}{2J+1} \sum_{M_f M_{f'}} \left[ \left| M_{if}^c(\mathbf{q}_\perp) \right|^2 + \left| M_{if}^s(\mathbf{q}_\perp) \right|^2 \right]. \quad (2.23)$$

It is known that a matrix element of the spin–orbit interaction is small and the main contribution to the DCS comes from the first term.

The analyzing power, characterizing the dependence of the scattering cross section on the direction of the spin of the incoming proton, is expressed through the matrix element as follows:

$$A_y = \frac{2 \operatorname{Re} \left[ M_{if}^c(\mathbf{q}_\perp) M_{if}^{s*}(\mathbf{q}_\perp) \right]}{d\sigma/d\Omega}, \quad (2.24)$$

and calculating it, we cannot manage without the spin–orbit matrix element.

## 2.2. The Analysis of Differential Cross Sections and Analyzing Powers

Using the WFs in three-body models, discussed in section 1, we calculated the characteristics (DCS and analyzing power  $A_y$ ) of the elastic  $p^6\text{He}$ ,  $p^8\text{Li}$ ,  $p^9\text{Li}$ , and  $p^9\text{C}$  scattering in inverse kinematics for two energies: 0.07 and 0.7 GeV/nucleon, within Glauber multiple scattering diffraction theory. While analyzing results, we emphasize two issues: (1) how the structure peculiarities of the considered nuclei influence the calculated characteristics; (2) what impact the mechanism of interaction exert on the investigated characteristics.

Calculating the DCS, it is sufficient to take into account the central part of the elementary  $pN$ -amplitude (see (2.6)), because the spin–orbit part makes the slight contribution to the cross section. While calculating the analyzing power, it is necessary to take into consideration the spin–orbit interaction in the elementary  $pN$ -amplitude (see (2.20)) and the spin dependence in WFs. Therefore the polarization characteristics are more sensitive to the calculation details (the WF structure and the interaction mechanism) than DCSs.

The following data were involved for comparison with experiment. The differential cross section of elastic scattering of protons by  $^6\text{He}$  in inverse kinematics at low energies was measured at facilities of the acceleration laboratory at RIKEN [31] at  $E = 0.071$  GeV/nucleon and at  $E = 0.041$  GeV/nucleon [164]. Elastic scattering of the  $^{4,6,8}\text{He}$  isotopes was measured at 0.70 GeV/nucleon by Alkhazov [110, 121] using the hydrogen-filled ionization chamber IKAR, which simultaneously was the gaseous target and recoil detector to  $|t| < 0.05$  (GeV/c)<sup>2</sup>, and further at the same facility at the GSI laboratory the measurements were extended up to  $|t| = 0.2$  (GeV/c)<sup>2</sup> [121]. The differential cross sections of  $p^8\text{Li}$  and  $p^9\text{Li}$  elastic scattering at an energy of 0.70 GeV/nucleon

were measured at GSI [122, 123] and at energy of 0.060 GeV/nucleon (for  $p^9\text{Li}$ ) the DCSs were measured at RIKEN [165].

The theoretical descriptions of elastic scattering of exotic (neutron- and proton-excess) nuclei by different targets (including the proton targets) were carried out by many authors (see Introduction) in different formalisms; with some of them we compare the results of our calculations.

**2.2.1. The dependence of the differential cross section and analyzing power on nuclear structure.** The dependence of DCS of  $p^6\text{He}$  scattering on model WFs calculated with different potentials of intercluster interactions (see Table 1) is shown in Fig. 10 for two energies:  $E = 0.071$  GeV/nucleon (panel a) and  $E = 0.717$  GeV/nucleon (panel b). Curves 1, 2, and 3 from [166] are calculated with WFs in models 1 and 2 and in the shell model. Experimental data in Fig. 10a are borrowed from [31]; those in Fig. 10b are taken from [110, 124].

The comparison of the calculation to the experiment in Fig. 10a indicates that at small scattering angles ( $\theta < 38^\circ$ ) the DCS with the three-body WFs is in good agreement with experimental data, while at large angles ( $\theta > 38^\circ$ ) the calculated curves lie above the experimental dots. The cross section, calculated with the shell WF [53], i.e.,  $\Psi^{JM_J} = 0.973 [2]^{31}S + 0.23 [11]^{33}P$ , deviates larger from the experiment at small angles than when calculated with the three-body WF, the experiment-theory agreement at large angles may be occasional. Differences in description of DCSs with different model WFs are related to their behavior inside the nucleus and on the periphery. In the case of small scattering angles, the transferred momentum is small (at  $\theta = 2^\circ$ ,  $q = 0.011$  GeV/c) and only the peripheral nuclear region can be probed (i.e., the WF asymptotics). It may be more extensive for the three-body WF than for the shell WF, where it drops rapidly and does not reproduce the real behavior of the nuclear WF. At large scattering angles, the transferred momentum increases (reaching the value  $q = 0.217$  GeV/c at  $\theta = 40^\circ$ ), the particles interact more in the inner region of the nucleus, where the particle correlation effects (which factually differ one model from the other) are more pronounced, and we observe different behavior of angular distributions. Therefore, at large angles, the DCS yields the important information regarding the contribution from the core, while at small angles, it provides data on the contribution from the skin (nuclear periphery).

For comparing to our results [166], we presented in Fig. 10a the results from [81, 82], in which the calculation was performed in the folding model in the context of HEA with three different densities of  $^6\text{He}$ : LSSM (the calculation in it is shown by curve 4), COSMA (the calculation in it is shown by curve 5), and the density used by Tanihata (it is close to COSMA and is not shown in the figure). The microscopic optical poten-

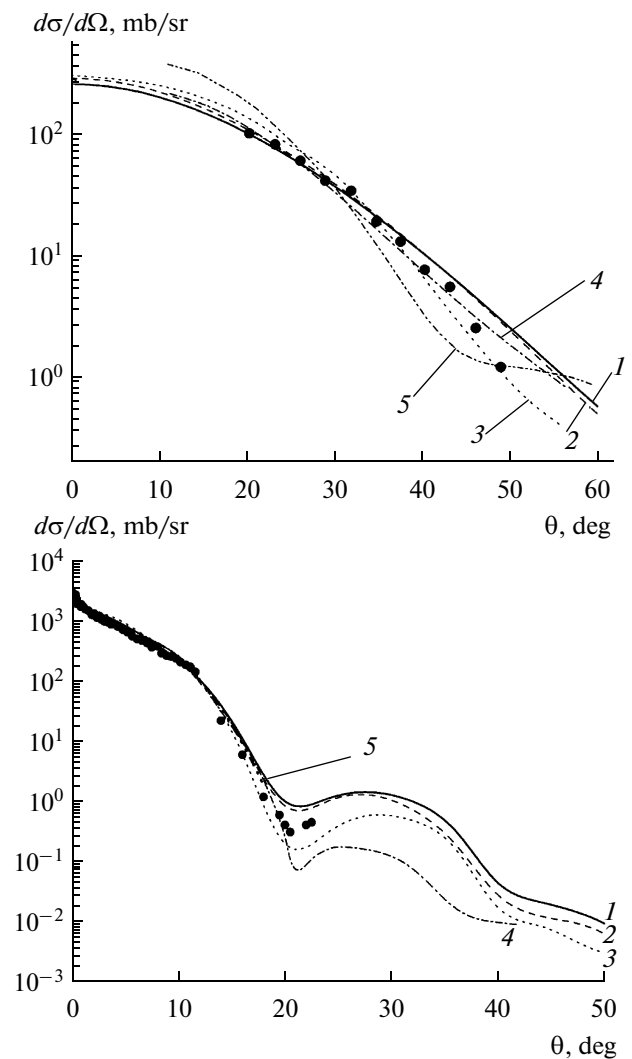


**Fig. 10.** Dependence of DCS of  $p^6\text{He}$  scattering on the model WFs calculated with different potentials of intercluster interactions for the energies (a)  $E = 0.071$  and (b)  $0.717$  GeV/nucleon. Curves 1, 2, and 3 are calculated with WFs in models 1, 2 (Table 1) and the shell model. The experimental data in this figure and in the other ones at  $E = 0.071$  GeV/nucleon are taken from [31], at  $E = 0.717$  GeV/nucleon are borrowed from [110, 124]. In panel a, curves 4 and 5 are taken from [81, 82], calculation with WFs of LSSM (curve 4) and COSMA (curve 5); in panel b, curve 4 is borrowed from [113], curve 5 is taken from [67].

tial in the context of HEA with the real and imaginary parts and with consideration for the spin-orbit interaction was applied in [81, 82]. It is seen from the figure that the best agreement with experiment is achieved in the calculation with the density in LSSM (this is the microscopically calculated density obtained in the complete  $4\hbar\omega$  shell model using the basis Woods-Saxon one-body WF with the realistic exponential asymptotic behavior), whereas the calculation with the COSMA density unsatisfactorily describes the experimental data at all angles. Physical reasons for

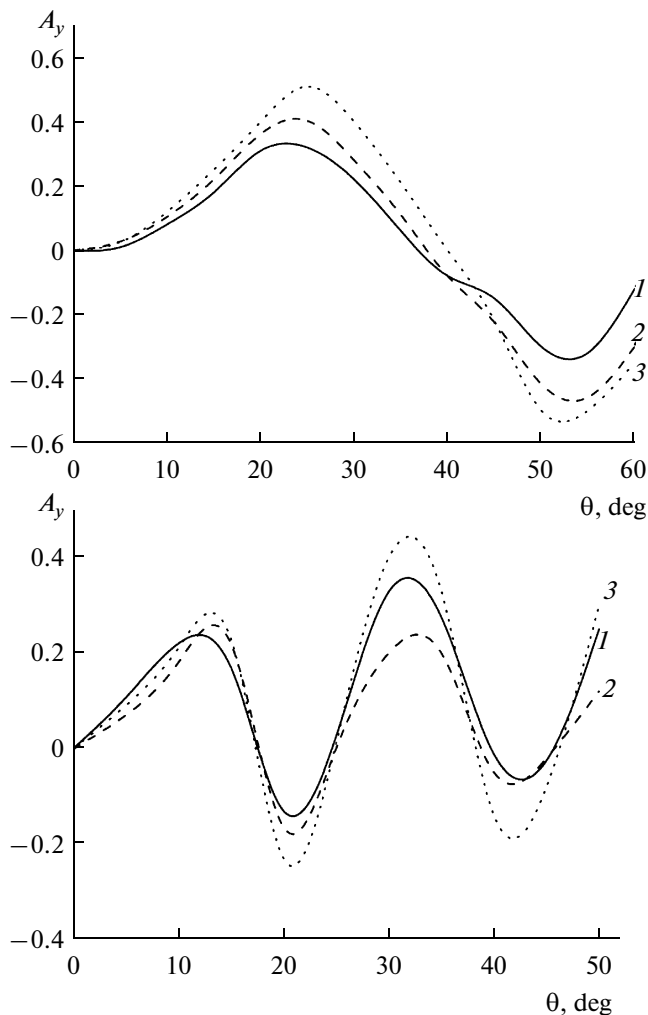


Fig. 11. The same as in Fig. 10 for  $A_y$ .

preference of the LSSM density are in its more extended exponential asymptotics as compared to the density based on Gaussians (COSMA).

It is seen in Fig.10b that the DCSs, calculated with the three-body WFs, describe adequately the experimental data at small angles and are very close to each other (curves 1 and 2), which is the evidence of WF small sensitivity to different potentials of intercluster interaction. The cross section with the shell WF (curve 3) differs from the first two, which is especially noticeable in the region of minimum and at large angles. For comparison to our results [166], we present the calculation from [113] (curve 4) and from [67] (curve 5). The DCS in these works is also calculated in Glauber approximation with total operator of multiple scattering with the microscopic three-body WF. In [113], the calculation had been performed before experimental data at  $\theta > 12^\circ$  had been obtained [124]; however, it is reasonable agreement with experiment at least  $\theta \sim 20^\circ$ . Curve 5 is calculated with the Faddeev's three-body WF, which leads to the correct static characteristics: the

energy of separation of two neutrons and the rms matter radius of  ${}^6\text{He}$ . Since the ideology of [67] is close to ours, then curves 1 and 5 merge in the figure. However, if at small angles  $\theta < 15^\circ$  there is not only qualitative, but also quantitative agreement of all calculated DCSs with experiment, then at  $\theta > 15^\circ$  the calculation and experiment diverge; none of the calculated curves is in agreement with experimental data in the region of the minimum of the cross section, though all of them (except for curve 5, which is calculated only to  $\theta \sim 18^\circ$ ) predict a minimum in the region  $\theta \sim 20^\circ$ . The divergence with experiment may be caused by both the WF inadequacy and the inapplicability of Glauber approximation for large angles.

Let us inspect how the analyzing power  $A_y$  behave for  $p^6\text{He}$  scattering depending on the same WFs, as in Fig. 10. In Fig. 11, it is seen that at small angles (for  $\theta < 15^\circ$ ) all curves are close to each other (like DCSs), but as the angle increases, their discrepancy grows. The fact that at small angles (corresponding to small transferred momenta) the calculated curves behave identically is an evidence of the weak influence of the peripheral region of the nucleus (scattering by neutron skin) on  $A_y$ . Although in comparison to the DCSs (for which all calculated curves merge at small angles), the polarization characteristics even in the region of forward angles somewhat differs from each other. The increase in the scatter of curves for larger angles (and for the increased transferred momentum) testifies to the different contribution of the high-momentum WF components. The spread in question shows the substantial sensitivity of the analyzing power to distribution of nucleons in the central region of the nucleus. Significantly differing from each other in the value of oscillations, all calculated curves reach maximal and minimal values at the same angles, and with the energy increase (from 0.07 to 0.7 GeV/nucleon) the number of oscillations increases. At  $E = 0.7$  GeV/nucleon, the correlations between the minima are observed in DCS and in  $A_y$  (Fig. 11b).

In [167], the DCSs and  $A_y$  of elastic scattering of the  ${}^{4,6,8}\text{He}$  isotopes by the polarized proton target are calculated at 297 MeV. The calculation is carried out in the optical model using the optical potential expansion into the series of multiple scattering in the KMT formulation (in the impulse approximation to the single scattering). In Fig. 12a, which is borrowed from [167], the DCSs of the  $p^4\text{He}$  (curve 1),  $p^6\text{He}$  (curves 2 and 3), and  $p^8\text{He}$  (curve 4) scatterings are shown. For  $p^6\text{He}$  scattering, the calculation is carried out with the three-body (curve 2) and oscillator (curve 3) WFs. The differential cross section of  $p^6\text{He}$  and  $p^8\text{He}$  is somewhat larger than that of  $p^4\text{He}$  at small angles, where the contribution of the valence neutrons is determinant. At large angles the decrease in DCS of  $p^4\text{He}$  occurs more slowly than that for  $p^6\text{He}$  and  $p^8\text{He}$ , because the distribution of the core matter density of  ${}^6\text{He}$  and  ${}^8\text{He}$

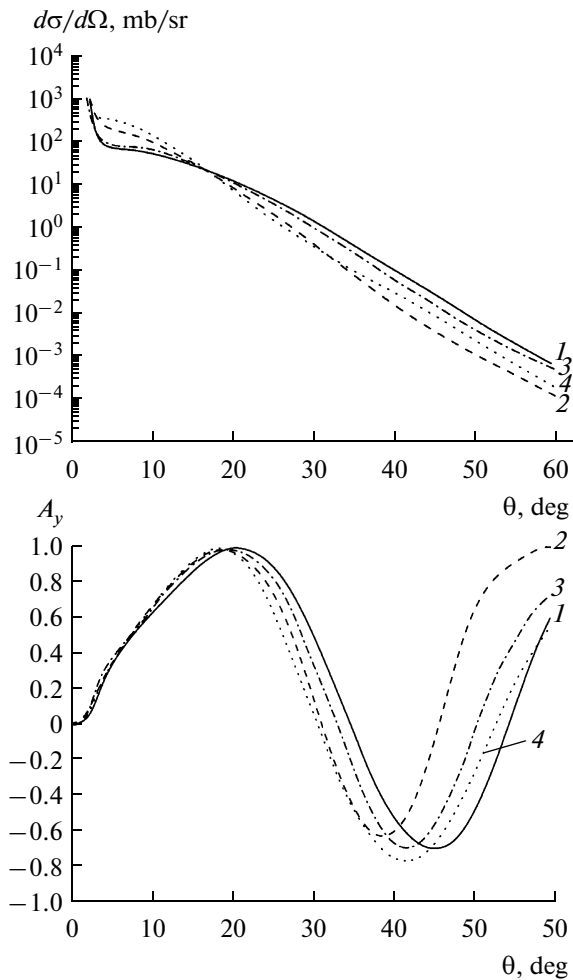


**Fig. 12.** (a) Differential cross sections and (b)  $A_y$  of  ${}^{4,6,8}\text{He}$  elastic scattering by the polarized proton target at 297 MeV from [167]. Curve 1 illustrates  $p^4\text{He}$  scattering, curves 2 and 3 refer to  $p^6\text{He}$  scattering with the three-body (2) and oscillator (3) WFs; curve 4 shows  $p^8\text{He}$  scattering.

in the momentum space has the shorter range than in  ${}^4\text{He}$  [167]. Therefore, at large angles the DCS yields the significant information on the contribution from the core in the optical model, which coincides with our conclusion.

Analyzing powers from [167] are given in Fig. 12b. The calculation at small angles demonstrates the identical behavior of  $A_y$  for all nuclei despite the fact that the matter density distribution of the valence nucleons is different (particularly for the three-body and oscillator WFs of  ${}^6\text{He}$ ). This is explained by the fact that the spin-orbit contribution from the valence neutrons halo is very small, because when the distribution of the matter density of valence neutrons (with short range) is folded with the spin-orbit component of the amplitude of the  $NN$  scattering, then for small transferred momenta this quantity is close to zero [167]. The role of the skin of valence neutrons of  $p^6\text{He}$  and  $p^8\text{He}$  is

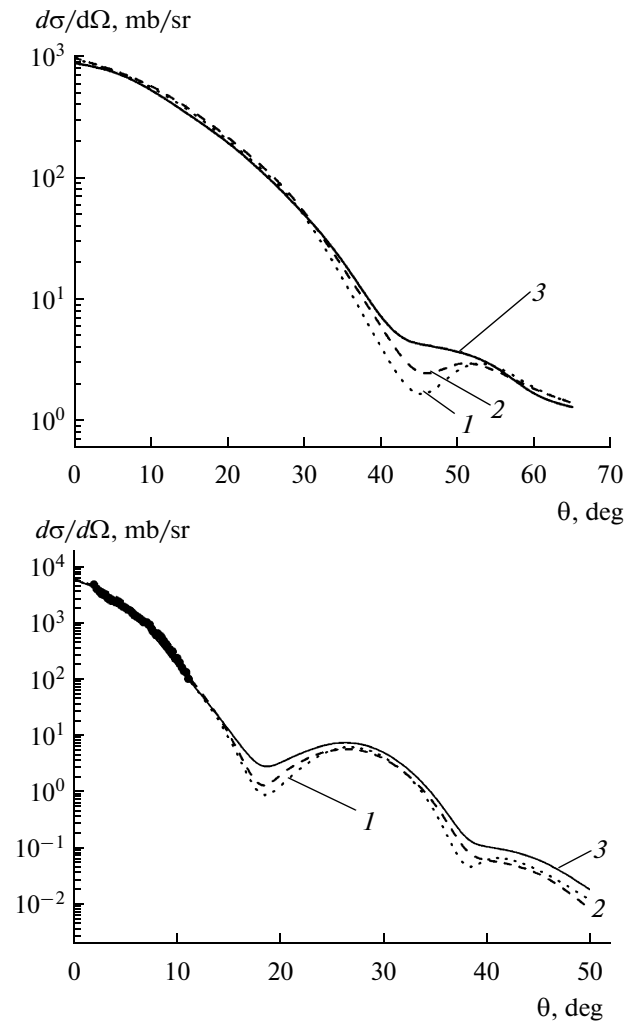


**Fig. 13.** Dependence of DCS of  $p^8\text{Li}$  scattering on the model WFs, calculated with different variants of potentials of the intercluster  $\alpha-t$ -interactions at (a)  $E = 0.060$  and (b)  $E = 0.698$  GeV/nucleon. Curves 1, 2, 3 present the calculation with the WFs of variant 1, 3, and 6 given in Table 4. The experimental data for this figure and the other ones at  $E = 0.698$  GeV/nucleon are taken from [122, 123].

shown in the fact that  $A_y$  is slightly displaced to the region of smaller angles as compared to  $p^4\text{He}$ . In spite of this, the analyzing powers for  $p^{4,6,8}\text{He}$  are very similar. This is not contradictory with our conclusions, though the complete coincidence of  $A_y$ , calculated with different WFs at small angles in our calculations is not observed.

Fig. 13. presents the result of the DCS calculation at  $E = 0.060$  (panel a) and  $E = 0.698$  GeV/nucleon (panel b) for  $p^8\text{Li}$  scattering with WF in the  $\alpha-t-n$  model [152] with different variants of potentials of intercluster interactions. Experimental data in Fig. 13a are taken from [122, 123]. Curves 1, 2, and 3 illustrate the calculation with WF of models 1, 3, and 6 given in Table 4. All three curves, identically describ-

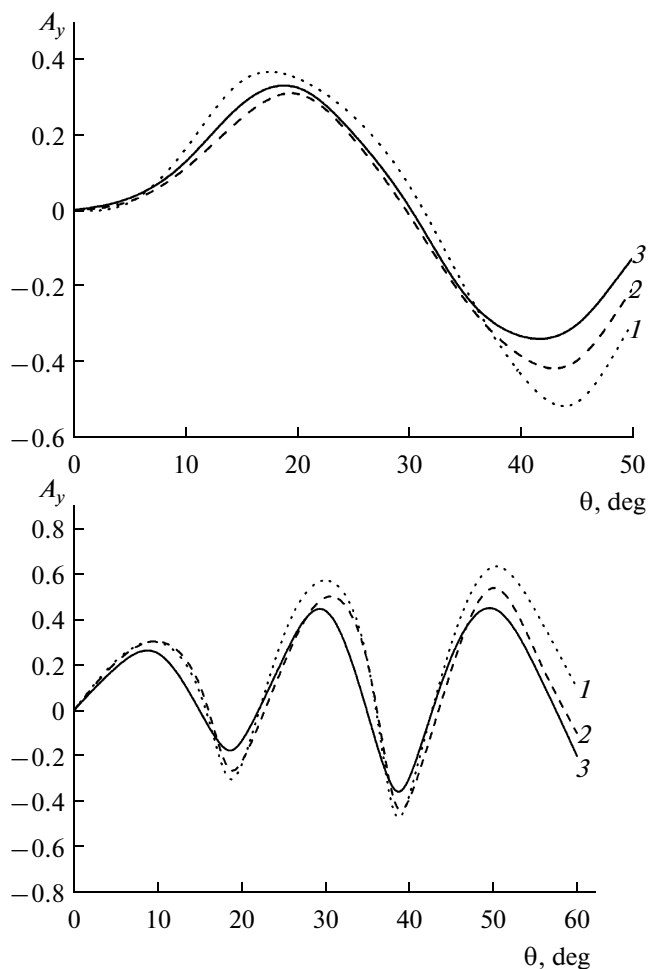


Fig. 14. The same as in Fig. 13 for  $A_y$ .

ing the DCS at small angles of scattering (it was explained in the analysis of  $p^6\text{He}$  scattering), differ essentially only in the region of maxima. As is seen in Table 4, different behavior of the displayed curves in the region of the minimum that is most characteristic both for the DCS and for  $A_y$  is associated with differences in the  $\alpha-t$  potential. In model 6, the  $\alpha-t$  potential takes into account the tensor interaction, which substantially increases the weight of components with  $L = 2$  (which is seen from the comparison of their weights in Table 4). Contribution from these components leads to an increase in quadrupole moment to the value  $Q = 30.36$  mb, close to experimental data, and to filling the minimum in the DCS, as it is seen from comparison of curve 3 with two others. It is known [168, 169] that scattering by nuclei with large values of quadrupole moments, such as  ${}^7\text{Li}$  ( $Q = -40$  mb),  ${}^9\text{Be}$  ( $Q = 53$  mb), demonstrates the DCS with the substantially less pronounced diffraction pattern than by spherically symmetric nuclei. This is explained by the fact that the electrostatic potential of a nucleus can be represented in the form of the monopole and quadrupole

terms, the latter (though it is weaker) fills minima in the diffraction pattern, caused by the monopole scattering, and does not make any substantial contribution to maxima. In our case, the WF components with  $L = 2$  precisely make the contribution to filling of the cross section minimum, and to the quadrupole moment, as is seen from Table 4. The comparison with the available experimental data at  $E = 0.698$  GeV/nucleon is shown in Fig. 13b. In the region of small scattering angles below  $\theta \sim 11.3^\circ$  (which corresponds to  $|t| = 0.049$  (GeV/c) $^2$ ), the agreement with experiment is observed for all variants of calculation, which, as in case of  $p^6\text{He}$  scattering, is evidence that the DCS is less sensitive to the contribution from the peripheral region of a nucleus, i.e., to scattering by the single valence nucleon. At large angles, the DCS becomes more sensitive to the structure peculiarities of different WFs, which is particularly noticeable in regions of minima at  $\theta \sim 18^\circ$  and  $38^\circ$ .

Let us consider how the analyzing power changes depending on different model WF in Fig. 14 at  $E = 0.060$  (panel a) and  $E = 0.698$  GeV/nucleon (panel b). Curves 1, 2, and 3 present the calculation with the WF of models 1, 3, and 6 from Table 4. The regularities of its behavior are the same as was noted for  $p^6\text{He}$  scattering: at small angles ( $\theta < 15^\circ$ ) for both energy values the analyzing powers are close to each other; as the angle increases their behavior differs more, with energy growth the number of oscillations increases, minima of  $A_y$  correlate with minima of DCS. The greatest oscillations are observed for curve 1, calculated with WF in model 1 (Table 4). From comparison of DCS (in Fig. 13) and  $A_y$  it is seen that the latter is more sensitive to the WF structure peculiarities.

Measuring the polarization characteristics is a difficult experimental problem even for stable targets, and for our nuclei they are not performed until now. Figure 15 illustrates the comparison of  $A_y$  for scattering of 0.2 GeV-protons: by  ${}^6\text{Li}$  nuclei (solid curve), experimental data from [170] are denoted by open circles; by  ${}^7\text{Li}$  nuclei (dashed curve), experimental data from [169] are denoted by black dots; by  ${}^8\text{Li}$  nuclei (dash-dotted curve). The calculation is carried out in Glauber approximation [171] with the WF in the  $\alpha-n-p$  [68–70] and  $\alpha-t$  [139] models for  ${}^{6,7}\text{Li}$  and with the WF of  ${}^8\text{Li}$  in model 6. For the  ${}^{7,6}\text{Li}$  nuclei, our curves almost identically describe  $A_y$  in the first maximum, but for angles exceeding  $35^\circ$  the substantial discrepancies are observed. None of the performed calculations describes satisfactorily the minimum of  $A_y$ . In [169, 170], the calculations of DCS and  $A_y$  were carried out in the optical model, whose first variant used the Woods–Saxon standard potential and in its second variant the microscopic folding-potential was employed. However, the calculations from [169, 170] (not given in our figure) match with the experiment only to  $\theta < 35^\circ$ , but they are incorrect in reproducing the negative slope and the position of minimum of

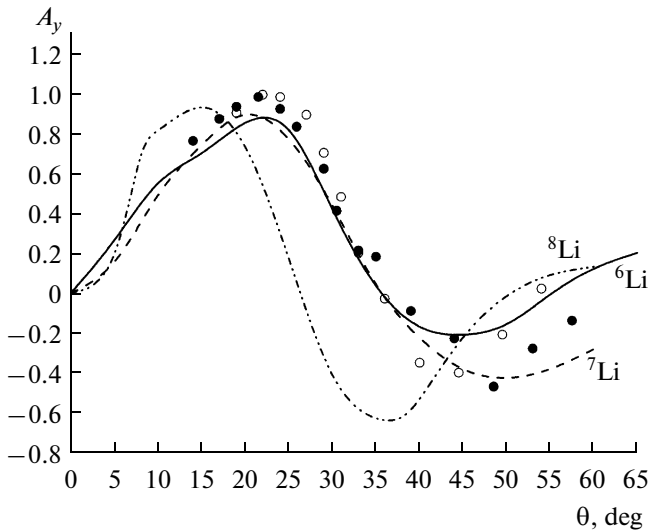


**Fig. 15.** Comparison of analyzing powers of the  $p^6\text{Li}$  (solid curve),  $p^7\text{Li}$  (dotted curve), and  $p^8\text{Li}$  (dash-dotted curve) scattering at  $E = 0.2$  GeV. The experimental data are marked as follows: relates to  $^6\text{Li}$  from [170], relates to  $^7\text{Li}$  from [169].

experimental data in the region of  $\theta > 35^\circ$ , which, in the authors' opinion, must be assigned to the insufficiency of the single scattering model and low quality of determination of the nuclear density. From comparison of all curves it is seen that values of  $A_y$  for  $p^6\text{Li}$  and  $p^7\text{Li}$  scatterings are close to each other for  $\theta \leq 35^\circ$ , whereas for  $p^8\text{Li}$  zeros of  $A_y$  are displaced by approximately  $10^\circ$  to the region of the smaller angles, which demonstrates the peculiarity of the structure for this nucleus.

Let us consider scattering by  $^9\text{Li}$  and  $^9\text{C}$  nuclei. In Fig. 16 and 17 the results of the DCS and  $A_y$  calculation for  $p^9\text{Li}$  and  $p^9\text{C}$  scatterings at the energies  $E = 0.060$  (Fig. 16a, 17a) and  $0.703$  GeV/nucleon (Fig. 16b, 17b) with the WF in the  $^7\text{Li}-n-n$  and  $^7\text{Be}-p-p$  models are shown. Curves 1 and 2 illustrate our calculation [153, 172] with WF in the  $^7\text{Li}-n-n$  model with different variants (3 and 4) of intercluster interactions from Table 5, curve 3 presents the calculation for  $^9\text{C}$  with the WF in the  $^7\text{Be}-p-p$  model from Table 6. Experimental data from [165] for  $E = 0.06$  and from [122, 123] for  $E = 0.703$  GeV/nucleon.

Since the  $^9\text{C}$  nucleus in the  $^7\text{Be}-p-p$  model is the mirror analog  $^9\text{Li}$  in  $^7\text{Li}-n-n$  model, then the difference in the calculation of DCS and  $A_y$  is that where in operator  $\Omega$  for  $^9\text{Li}$  the elementary  $pn$ -amplitude is used, it is substituted by the  $pp$ -amplitude for  $^9\text{C}$  there. Differences in parameters of these amplitudes are small: at  $E = 0.2$  GeV  $\sigma_{pn} = 4.2$  fm $^2$ ,  $\sigma_{pp} = 2.36$  fm $^2$ ,  $\varepsilon_{pn} = 0.71$ ,  $\varepsilon_{pp} = 1.15$ ,  $\beta_{pn} = 0.68$ ,  $\beta_{pp} = 0.65$  [158]; at

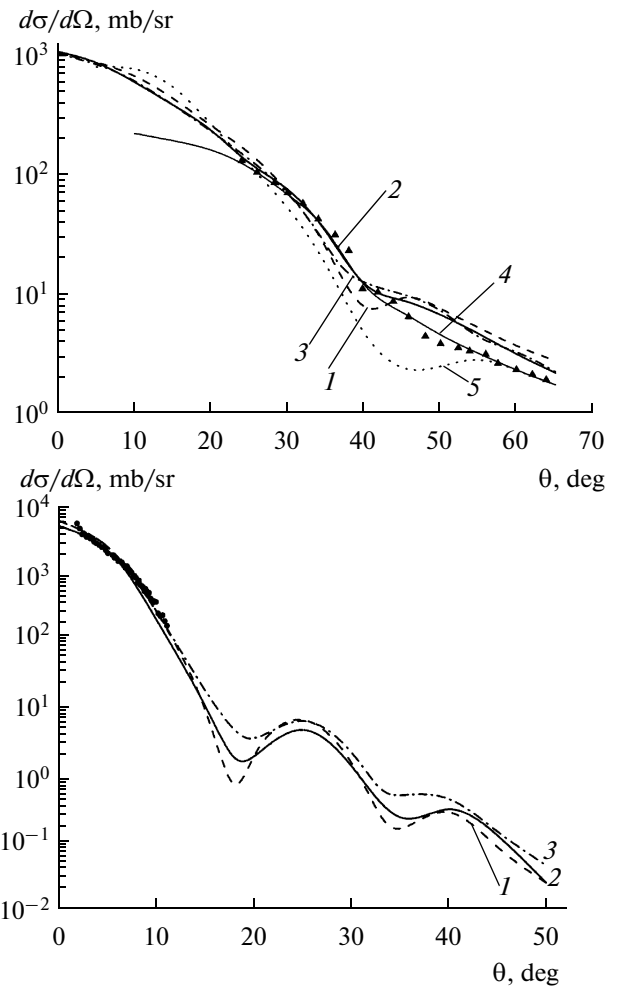


**Fig. 16.** Dependence of DCS of  $p^9\text{Li}$  scattering on the WFs calculated with different potentials of intercluster interactions for the energies (a)  $E = 0.06$  and (b)  $0.717$  GeV/nucleon. Curves 1 and 2 present the calculation with the WFs in models 3 and 4 from Table 5; curve 3, the calculation for  $p^9\text{C}$  with the WF in  $^7\text{Be}-p-p$  model from Table 6. The experimental data in this figure and in the other ones at  $E = 0.06$  GeV/nucleon are taken from [165]; at  $E = 0.717$  GeV/nucleon, from [122, 123]. The results of calculation within the optical model which are taken from [173] (curve 4) and from [174] (curve 5) are shown in panel a.

$$E = 1.0 \text{ GeV } \sigma_{pn} = 4.04 \text{ fm}^2, \sigma_{pp} = 4.75 \text{ fm}^2, \\ \varepsilon_{pn} = -0.5, \varepsilon_{pp} = -0.1, \beta_{pn} = 0.21, \beta_{pp} = 0.21 \text{ [159].}$$

Comparing our calculation [152, 153, 172] with experiment [165] in Fig. 16a, we shall note that calculations performed in Glauber approximation with the WF in models 3 and 4 (see Table 5) are in quantitative agreement with the experimental data only in the forward region of angles to  $\theta < 30^\circ$ , then to  $\theta < 40^\circ$  the calculated cross sections lie below the experimental data points, while at  $\theta > 45^\circ$  they are above the experimental data points. This can be explained by two circumstances: inapplicability of Glauber formalism for the medium and large scattering angles and not quite

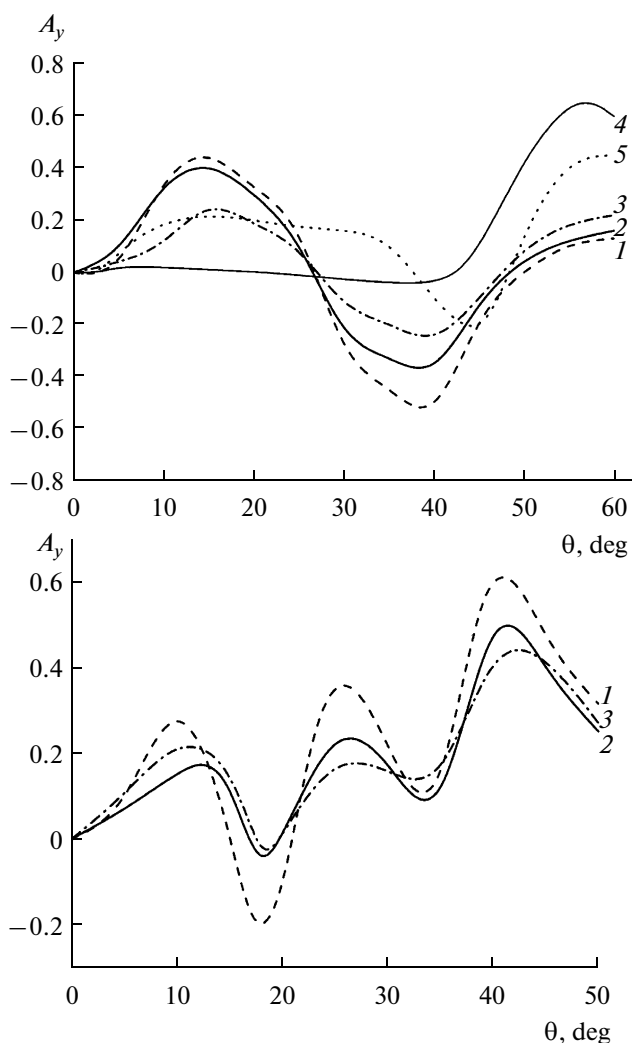


Fig. 17. The same as in Fig. 16 for  $A_y$ .

adequate description of the inner region of the nucleus. For comparison with our results, the results of the calculations in the optical model from [173] (curve 4) and [174] (curve 5) are given in the figure. In [173], the DCSs are calculated in the optical model with the complex folding-potential and with the density, taking into account the effects of the nuclear medium. The effective  $NN$  potential is obtained from solving the Bethe–Brueckner–Goldstone equation in the infinite nuclear matter. This curve correctly reproduces the experimental data in the entire angular range, because the calculation is performed in the optical model that is not connected with limitation for large scattering angles (like in Glauber theory). On the contrary, curve 5 from [174], in which the calculations are also carried out in the optical model with the Paris–Hamburg nonlocal potential, lies below experimental data almost in the entire angular range, except for several data points in the range of angles  $\theta > 55^\circ$ .

In Fig. 16b, in the region of forward angles to  $\theta < 15^\circ$  all curves identically reproduce DCS, agreeing with experimental data. There are differences in regions of diffraction minima and at large scattering angles. The degree of filling minima correlates with the value of quadrupole moment  $Q$ :  $|Q| = 23.98$  mb corresponds to the cross section with the deepest minimum (curve 1);  $|Q| = 27.9$  mb (Table 5) corresponds to the cross section whose minimum is less pronounced (curve 2),  $|Q| = 31.5$  mb (Table 8) corresponds to the shallowest cross section (curve 3 for  ${}^9\text{C}$ ). Filling of minima in the DCS, as well as the increase in quadrupole moment, are associated with the consideration of exchange terms with strong spin dependence in the  ${}^7\text{Li}-n$  potential, which leads to the WF components with  $L = 1$  with appreciable weights (Table 5). As is shown in [175], the consideration for the spin–orbit components in the optical potential provides the substantial smoothing of minima in the DCS. The result of calculation for the  ${}^9\text{C}$  nucleus (curve 3) for both energies is close to the result for  ${}^9\text{Li}$  (particularly to curve 2), which is naturally explained by the similarity of their WFs, calculated in the identical potentials.

Let us turn to the consideration of the analyzing power. Figure 17a presents  $A_y$  at  $E = 0.06$  GeV/nucleon. (Designations of curves are the same as in Fig. 16a.) Curves 1 and 2 differ in absolute values but are similar to each other in location of maxima and minima. Curve 1 has the greatest oscillations (its minima in the DCS are deeper than those in curve 2). The analyzing power for  ${}^9\text{C}$  (curve 3) is close to  $A_y$  for  ${}^9\text{Li}$  (curve 2), which, like for the DCS, is explained by the similarity of their WFs.

Predictions for this characteristic, performed in [173, 174] (within the same above described formalisms as for the DCS), differ qualitatively and quantitatively from both our predictions and each other. For example,  $A_y$  from [173] (curve 4) is close to zero in the full range of forward angles to  $\theta < 42^\circ$  and reaches the maximum (+0.6) at  $\theta \approx 57^\circ$ , whereas  $A_y$  from [174] (curve 5) has a small positive value (+0.2) at  $\theta < 38^\circ$ , reaches the minimum (–0.2) at  $\theta \approx 45^\circ$ , and then increases to 0.45 at  $\theta \approx 60^\circ$ . Comparing  $A_y$ , predicted in [174] with three different densities of  ${}^9\text{Li}$  (calculated with different interaction potentials, not shown in our figure), we can see that all of them differ from each other, to the extent that they are in antiphase at certain angles: one curve reaches maximum while another reaches minimum. Thus, even with relatively small variations of the calculation the polarization characteristics can cardinally differ from each other.

Figure 17b shows  $A_y$  for  $E = 0.703$  GeV/nucleon. Curves 1, 2, and 3 are designated the same as in Fig. 16b. Maxima and minima of the analyzing power are localized at the same scattering angles, though their amplitudes are substantially different. Curve 1

has the greatest oscillation amplitude (the respective DCS in Fig. 16b has the deepest minima), curve 3 is the most smoothed (for the  ${}^9\text{C}$  nucleus, the respective DCS in Fig. 16b has also the most filled minima). As compared with Fig. 17a, at an energy of 0.703 GeV/nucleon,  $A_y$  oscillates stronger, and it has three maxima and two minima which correlate with the DCS minima in Fig. 16b.

Regarding the aggregate of data presented in Fig. 16 and in Table 5, we may conclude that the best description of the DCS and static characteristics is achieved with the WF in model 4, calculated in the Buck potential with the exchange terms with strong spin dependence.

Figure 18 presents the results of the calculation of the DCS of  $p^9\text{Li}$  scattering with the WF of the  ${}^9\text{Li}$  nucleus in the  $\alpha-t-2n$  model from Table 9 (curves 1 and 2) and for comparison in the  ${}^7\text{Li}-n-n$  model (curve 3, the same as curve 2 in Fig. 16) at  $E=0.06$  GeV/nucleon (panel a) and  $E=0.703$  GeV/nucleon (panel b). The calculation with both variants of  $\alpha-t$  potentials (curve 1 corresponds to model 1, curve 2 corresponds to model 2) leads to an approximately identical result in the DCS description; a difference is only observed in the region of minima of cross sections. More substantial differences are observed between calculations with WF in different models: the cross section with the  $\alpha-t-2n$  WF at both energies has more pronounced diffraction structure than that with the  ${}^7\text{Li}-n-n$  WF. Curve 3 lies above curves 1 and 2 in the entire range of angles, moreover, the discrepancy in the absolute value of cross sections increases as the scattering angle grows. Why does the DCS with the  ${}^7\text{Li}-n-n$  WF have the smoother structure, without deep minima, which are observed in the cross section with  $\alpha-t-2n$  WF? It follows from the different description of the inner structure of the nucleus, to which the value of quadrupole moment  $Q$  also testifies. The theoretical value of quadrupole moment, calculated with the  $\alpha-t-2n$  WF of  ${}^9\text{Li}$  is  $Q_{\text{theor}} = -16.75$  mb in model 1 and  $-17.4$  mb in model 2 (Table 9); with the  ${}^7\text{Li}-n-n$  WF the quadrupole moment value  $Q_{\text{theor}} = -27.93$  mb, while the measured value  $Q_{\text{exp}} = -27.4$  mb. This is an important characteristic, determining the quadrupole deformation of the nucleus. For the WF used in the  $\alpha-t-2n$  model, it diverges from the experimental data by 40%. As it was already said, the filling of diffraction minima occurs only in the strongly deformed nuclei with spin  $J > 1$ , so that the presence of deep minima in curves 1 and 2 may be connected with the underestimation of the quadrupole deformation of nucleus in this model.

At  $E = 0.7$  GeV/nucleon, the experiment is carried out only for forward scattering angles and the most interesting region (of interference) is outside its limits, which does not allow one to draw the well-justified conclusion on the suitability of different model WF.

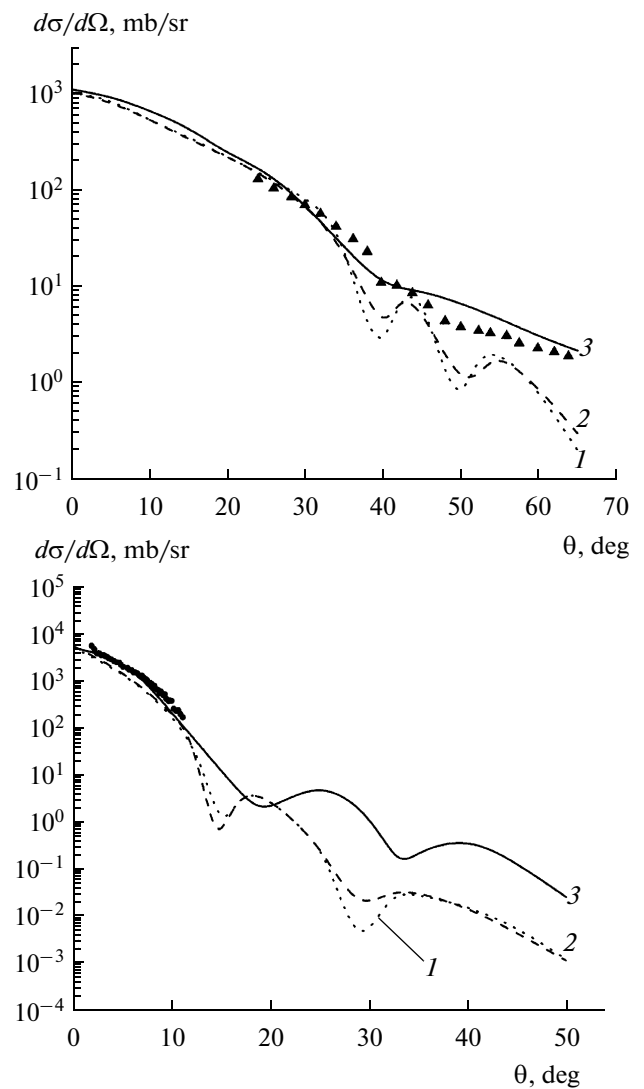


**Fig. 18.** The DCS of  $p^9\text{Li}$  scattering at the energies (a)  $E = 0.06$  and (b)  $E = 0.703$  GeV/nucleon with the WFs of the  ${}^9\text{Li}$  nucleus in the  $\alpha-t-2n$  model. Curves 1 and 2 display the calculation with the WFs in models 1 and 2 from Table 9; curve 3 (the same as curve 2 in Fig. 16, i.e., the calculation with WFs within the  ${}^7\text{Li}-n-n$  model).

However, the fact that curves 1 and 2 (with the WF in the  $\alpha-t-2n$  model) are in poorer agreement than curve 3 with experiment, and also the comparison of static characteristics in Tables 5 and 9, assure us that the  ${}^7\text{Li}-n-n$  model of  ${}^9\text{Li}$  nucleus is preferable.

The comparison of the DCSs in Fig. 18, calculated with the WFs in the  $\alpha-t-2n$  and  ${}^7\text{Li}-n-n$  models (curves 1, 2, and 3), shows that they are very different from each other, whereas the DCS with the WF, calculated in the common model but with different potentials of intercluster interactions (curves 1 and 2 in Figs. 18 and 16), are similar to each other. Obviously, this means that the correctly chosen cluster structure for description of both static and dynamic characteris-

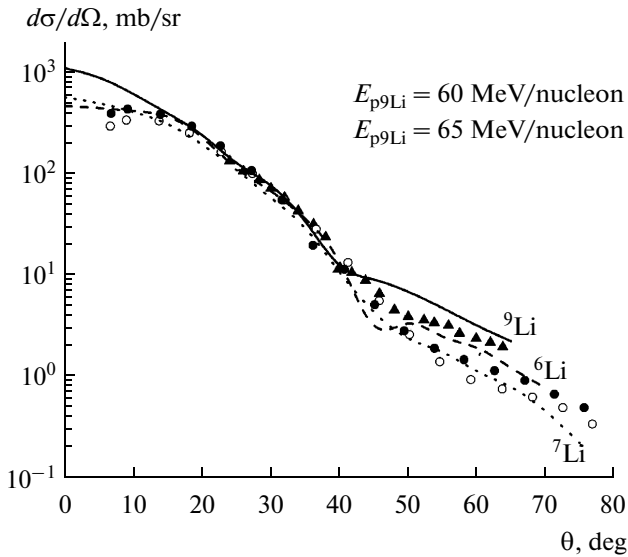


**Fig. 19.** The DSCs of scattering by the  ${}^6\text{Li}$ ,  ${}^7\text{Li}$ ,  ${}^8\text{Li}$ , and  ${}^9\text{Li}$  nuclei at  $E = 60$  and  $65$  MeV/nucleon. The dashed, dotted, and solid curves illustrate the calculation for the  ${}^6\text{Li}$ ,  ${}^7\text{Li}$ , and  ${}^9\text{Li}$  nuclei. The experimental data are marked as follows: relates to  ${}^9\text{Li}$  from [165], relates to  ${}^7\text{Li}$  from [173], is associated with  ${}^6\text{Li}$  from [173].

tics is more important than one or other type of inter-cluster potentials. The fact that the WF in the  ${}^7\text{Li}-n-n$  model better describes the experimental data at all energies supports the dominating two-component structure of  ${}^9\text{Li}$  in the form of the  ${}^7\text{Li}$  core and the skin of two neutrons.

Let us compare the experimental data and theoretical calculations of the DCS for the  ${}^6\text{Li}$ ,  ${}^7\text{Li}$ , and  ${}^9\text{Li}$  nuclei given in Fig. 19 at the close energies  $E = 0.060$  and  $0.065$  GeV/nucleon. The experimental data are taken from [165] for  $p^9\text{Li}$  (triangles) and from [173] for  $p^6\text{Li}$  (light circles) and  $p^7\text{Li}$  (black dots). The experimental cross sections for all nuclei are close to each other (to  $\theta \sim 48^\circ$ ), they decrease monotonously as the scattering angle increases and have the implicitly pronounced minimum (rather a bend in the cross section) at  $\theta \approx 45^\circ$ . However, at large angles the experimental cross section for  $p^9\text{Li}$  scattering diminishes slower than for  $p^6\text{Li}$  and  $p^7\text{Li}$ . Theoretical DCSs are calculated within Glauber theory [176] with the WF in the  $\alpha-n-p$  (for  ${}^6\text{Li}$ , dashed curve),  $\alpha-t$  (for  ${}^7\text{Li}$ , dotted curve), and  ${}^7\text{Li}-n-n$  (for  ${}^9\text{Li}$ , solid curve) models. All curves almost identically describe cross sections in the region of forward angles, but at large angles they start to deviate. The differential cross section for the  ${}^7\text{Li}$  nucleus is in better agreement with experimental data than other cross sections, which we attribute to the well fitted  $\alpha-t$ -WF of this nucleus [139, 140] (in particular, it correctly describes the quadrupole moment).

Thus, it is shown that the DCSs depend on the WF structure; however, at small scattering angles (where

the WF asymptotic behavior plays the appreciable role), this dependence is very weak: all curves equally describe the cross section to the angles  $\theta < 20^\circ$ . If the contradictory conclusion is made in some works (about the strong dependence of the cross section on asymptotic behavior of density), while studying the few-body correlations in  $p^6\text{He}$  scattering, as in [111], then, as Alkhazov showed in [121], this takes place not due to the strong sensitivity of DCS to the WF asymptotics, but because the calculations use the density distributions which differ not only at large distances ( $r > 6$  fm), but at small ( $r < 5$  fm) distances too. And this is the reason why DCSs with different densities can significantly differ from each other. The small sensitivity of the DCS of elastic scattering to different density distributions at small scattering angles is mentioned in [177], where the DCS of  $p^8\text{He}$  elastic scattering at  $E = 26, 45$  and  $72$  MeV/nucleon is calculated using two different methods: DWBA with JLM-potential and in the eikonal approximation. At small scattering angles the DCSs with different density distributions (for total matter and neutron skin), obtained in COSMA, equally describe experimental data, whereas at large angles the calculated curves differ from each other, from which a difference between the core and the skin may be revealed. However, the authors emphasize that the difference in the density distribution in the core and on the periphery is not very noticeable, is model-dependent, and in order to use it for measuring the density distribution, the accurate measurements of the cross section at large angles are required, which is a difficult problem due to low DCS.

The analogous conclusion is drawn in [22, 122, 167]: “contribution from the core nucleons has maximum at the larger angles than from the neutron halo” [22].

**2.2.2. The dependence of a differential cross section on the structure constituents of wave functions.** Let us consider in more detail which contribution to a DCS comes from the WF components. A WF of relative motion for  $p^6\text{He}$  scattering can be written down as a sum of two components (see (1.8)). Substituting it in amplitude (2.1) and then in DCS (2.23), it is possible to calculate, which contribution to the cross section comes from each component:

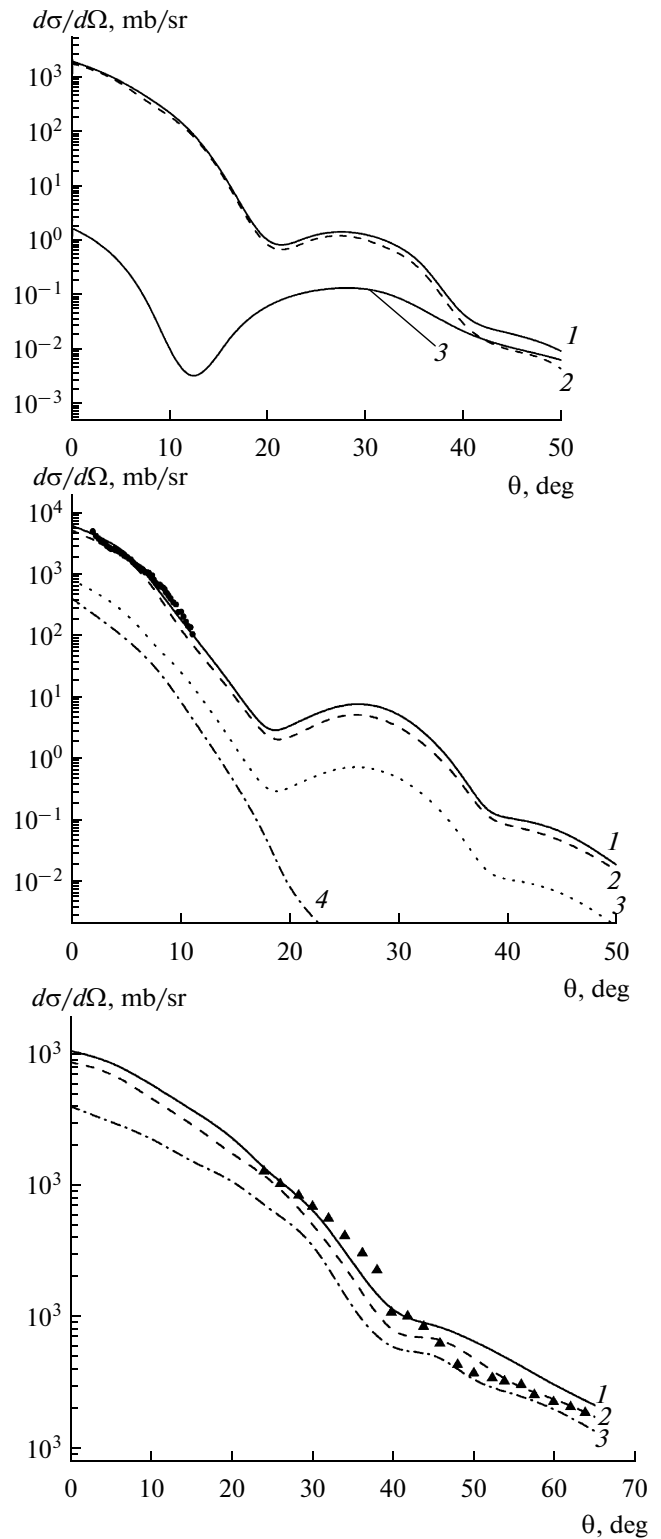
$$\frac{d\sigma}{d\Omega} = \frac{1}{2J+1} \frac{|ik|}{2\pi} \sum_{M_s, M_s'} \int d\mathbf{c}_\perp d\mathbf{R}_{6\text{He}} \exp(i\mathbf{q}_\perp \mathbf{c}_\perp) \delta(\mathbf{R}_{6\text{He}}) \times \left\{ \langle \Psi_{0000}^{JM_J} | \Omega | \Psi_{0000}^{JM_J} \rangle + \langle \Psi_{1111}^{JM_J} | \Omega | \Psi_{1111}^{JM_J} \rangle \right\}^2. \quad (2.25)$$

Figure 20a illustrates the contribution to the DCS (curve 1, the same as curve 1 in Fig. 10b) from  $S$ -wave (curve 2), which is due to consideration of the first term in Eq. (2.25), and  $P$ -wave (curve 3), due to consideration of the second term in Eq. (2.25) at  $E = 0.717$  GeV/nucleon. In order to explain the cross section behavior, we shall turn to the geometric shape of different nuclear states. As is seen from Fig. 2,  $S$ -state of the WF includes two geometric configurations: the

**Fig. 20.** Dependence of DCS on contribution of different components of WF. In panel a, the  $p^6\text{He}$  scattering at  $E = 0.717$  GeV/nucleon is presented. Curve 2 displays the contribution from  $S$ -wave ( $\Psi_{0000}^{JM_J}$ ) corresponding to the consideration of the first term in Eq. (2.25); curve 3, from  $P$ -wave ( $\Psi_{1111}^{JM_J}$ ) corresponding to the consideration for the second term in Eq. (2.25); curve 1 presents their total contribution (the same as curve 1 in Fig. 10b). In panel b, the  $p^8\text{Li}$  scattering at  $E = 0.7$  GeV/nucleon is shown. Curves 2, 3, and 4 display contributions from the first ( $\lambda/LS = 1111$ ), second ( $\lambda/LS = 1121$ ), and the third ( $\lambda/LS = 3121$ ) terms of Eq. (2.26). Curve 1 presents the sum of all components (the same as curve 3 in Fig. 13b). In panel c, the  $p^9\text{Li}$  scattering at  $E = 0.060$  GeV/nucleon is illustrated. Curve 2 displays the contribution from the first ( $\lambda/LS = 0003/2$ ) term of Eq. (2.27), curve 3 presents those from the second ( $\lambda/LS = 1113/2$ ) and third ( $\lambda/LS = 1111/2$ ) terms of Eq. (2.27), and curve 1 is the sum of all three components (the same as curve 1 in Fig. 16a).

dineutron one  $\alpha-(2n)$  with maximum at the point  $r \approx 1.7$  fm,  $R \approx 3$  fm; and the cigar-like one  $(n-\alpha-n)$  with maximum at  $r \approx 4$  fm,  $R \approx 1$  fm, where  $r$  is the mean distance between two neutrons, and  $R$  is the mean distance between the center-of-mass of two neutrons and the  $\alpha$ -particle. From the fact that in the  $\alpha-(2n)$  configuration  $r \approx 1.7$  fm it follows that the dineutron cluster in the nucleus is strongly compressed because the size of a free deuteron is 4.3 fm. It is seen in Fig. 20a that the cross section calculated with  $S$ -wave, according to its weight (more 95% in model 1) makes the main contribution and completely dominates at small scattering angles. The cross section with this component has rather a monotonous form with two minima: at  $\theta \approx 20^\circ$  and  $40^\circ$ . The configuration of  $P$ -wave (Fig. 3) is close to the isosceles triangle with  $r \approx 2.5$  fm,  $R \approx 1.7$  fm, which rotates about the common center-of-mass. This configuration makes a small contribution to the cross section, noticeable only at the scattering angles  $\theta > 40^\circ$ . In the cross section with  $D$ -wave, the sharp minimum is observed at  $\theta \approx 12^\circ$ ; this has no impact, however, on the total cross section, because the DCS with  $S$ -wave in this region is larger by 4 orders of magnitude.

This behavior of partial cross sections, calculated with different WF components, can be understood, if not only their weights but also relative distances between the  $\alpha$ -cluster and nucleons are taken into account. These distances in  $S$ -component are fairly large, and the component spreads to  $r \sim 8$  fm and  $R \sim 7$  fm and includes the nucleus periphery together with its central part. The peripheral region of the nucleus in the momentum space corresponds to small transferred momenta (and small scattering angles); therefore, the contribution from this component to the cross section is particularly large at small angles. The  $D$ -wave maximum is located closer to the nucleus center (than that of  $S$ -wave), and the  $D$ -wave extends to a shorter distance than  $S$ -wave, this configuration is as if com-



pletely drawn into the inner region of the nucleus, its contribution to the periphery is negligibly small. The inner region of the nucleus in the momentum space corresponds to large transferred momenta (i.e., to large scattering angles), therefore the contribution to the cross section from  $P$ -component at forward angles

is small (because of its small weight), while at large angles it is comparable with the contribution of  $S$ -wave and even exceeds it (which cannot be explained by the small weight of  $P$ -wave).

A DCS for  $p^8\text{Li}$  scattering which takes into account three WF components from Table 4 is recorded following Eq. (1.13) as

$$\begin{aligned} \frac{d\sigma}{d\Omega} = & \frac{1}{2J+1} \frac{ik}{2\pi} \sum_{M_s, M'_s} \int d\mathbf{c}_\perp d\mathbf{R}_9 \exp(i\mathbf{q}_\perp \mathbf{c}_\perp) \delta(\mathbf{R}_9) \\ & \times \left\{ \langle \Psi_{1111}^{JM_J} | \Omega | \Psi_{1111}^{JM'_J} \rangle + \langle \Psi_{1121}^{JM_J} | \Omega | \Psi_{1121}^{JM'_J} \rangle \right. \\ & \left. + \langle \Psi_{3121}^{JM_J} | \Omega | \Psi_{3121}^{JM'_J} \rangle \right\}^2. \end{aligned} \quad (2.26)$$

Contributions from different WF components in model 6 (Table 4) to the DCS are presented in Fig. 20b at  $E = 0.7$  GeV/nucleon. Curves 2, 3, and 4 show the contributions from the first, second, and third terms of Eq. (2.26). Curve 1 is the sum of all three components (the same as curve 3 in Fig. 13b). Let us compare the partial contribution of the components with their geometric configuration presented in Figs. 4–6. The configuration  $\lambda/LS = 1111$  (Fig. 4) has a maximal weight of 0.88 (Table 4) and two peaks at the points  $r = 1$  fm,  $R \approx 2.5$  fm and  $r \approx 3$  fm,  $R \approx 2.5$  fm. Here  $r$  is the distance between the  $\alpha$  and  $t$  clusters,  $R$  is the distance between the center-of-mass of  $\alpha-t$  and  $n$ . The neutron in this configuration is at an equal distance of 2.5 fm from the center-of-mass of  $\alpha-t$ . The  $\alpha$  and  $t$  clusters in the first maximum are three times closer to each other than those in the second maximum. The WF extension in both coordinates reaches 6 fm, and it completely determines the contribution to the DCS at both small and large angles. The component  $\lambda/LS = 1121$  is very similar to the first one by its form. It is seen in Fig. 5 that two maxima are localized at the points  $r \approx 1$  fm,  $R \approx 2.0$  fm and  $r \approx 3$  fm,  $R \approx 2.0$  fm. The small difference from the first configuration is that the neutron is 0.5 fm closer the center-of-mass of  $\alpha-t$ . The extension of the WF also reaches 6 fm, therefore we can see in Fig. 20b the analogous behavior of curves 2 and 3 with the contributions comparable with their weights (see Table 4). The component  $\lambda/LS = 3121$  (Fig. 6) has one peak at the point  $r \approx 2.5$  fm,  $R \approx 2.0$  fm, its maximal extension is 5.5 fm. The WF in the central region of the nucleus is equal to zero, therefore the corresponding DCS sharply decreases and already at  $\theta \sim 20^\circ$  becomes smaller by three orders of magnitude than the cross section with the dominating component. Therefore, we see in Fig. 20b that the DCS is completely determined by the contributions of the first and second components of WF according to their weights.

There is a somewhat different situation for  $p^9\text{Li}$  scattering. A differential cross section with consider-

ation of three components of WF of  $^9\text{Li}$  (see Eq. (1.14)) can be written as

$$\begin{aligned} \frac{d\sigma}{d\Omega} = & \frac{1}{2J+1} \frac{ik}{2\pi} \sum_{M_s, M'_s} \int d\mathbf{c}_\perp d\mathbf{R}_9 \exp(i\mathbf{q}_\perp \mathbf{c}_\perp) \delta(\mathbf{R}_9) \\ & \times \left\{ \langle \Psi_{0003/2}^{JM_J} | \Omega | \Psi_{0003/2}^{JM'_J} \rangle + \langle \Psi_{1113/2}^{JM_J} | \Omega | \Psi_{1113/2}^{JM'_J} \rangle \right. \\ & \left. + \langle \Psi_{1111/2}^{JM_J} | \Omega | \Psi_{1111/2}^{JM'_J} \rangle \right\}^2, \end{aligned} \quad (2.27)$$

where the first, second, and third terms in braces determine the contribution of the WF components with the quantum numbers  $\lambda/LS = 0003/2, 1113/2, 1111/2$  respectively. The calculation, performed using this formula, is illustrated in Fig. 20c at  $E = 0.060$  GeV/nucleon: curve 2 shows the contribution from the first term of Eq. (2.27), curve 3 displays the contribution from the second and third terms of (2.27), and, as is seen from the figure, these curves are similar in form and differ only in absolute values. Curve 1 is the sum of all three components (the same as curve 1 in Fig. 16a). An absolute value of the contribution from the components to the DCS is determined by their weight (see Table 5): the first WF component (curve 2) makes the determining contribution to the cross section, because its weight is 0.654, the weight of two other components is 0.167, therefore their contribution is smaller (curve 3). However, these components make the contribution in all angular range, and we cannot neglect it. Let us examine the geometric configurations of these WF components (Fig. 7, 8). As is seen from the figures and discussion, conducted in section 1 (see 1.3), the geometric shapes of all three configurations are almost identical, therefore their contributions in the DCS are similar.

**2.2.3. The dependence of a differential cross section on the scattering mechanism.** Within our approach, Glauber operator  $\Omega$  (Eq. (2.3)) is expanded into the series of scattering in the subsystems (clusters) composing the nucleus. Substituting it in the DCS, we derive

$$\frac{d\sigma}{d\Omega} = \frac{1}{2J+1} \left| M_{ij}^{(1)}(\mathbf{q}_\perp) - M_{ij}^{(2)}(\mathbf{q}_\perp) + M_{ij}^{(3)}(\mathbf{q}_\perp) \right|^2, \quad (2.28)$$

where

$$\begin{aligned} M_{ij}^{(1)}(\mathbf{q}_\perp) = & \frac{ik}{2\pi} \sum_{M_s, M'_s} \int d\mathbf{c}_\perp d\mathbf{R}_A \exp(i\mathbf{q}_\perp \mathbf{c}_\perp) \delta(\mathbf{R}_A) \\ & \times \left\{ \langle \Psi_{\lambda/LS}^{JM_J} | \Omega_1 + \Omega_2 + \Omega_3 | \Psi_{\lambda/LS}^{JM'_J} \rangle \right\}. \end{aligned} \quad (2.29)$$

$$\begin{aligned} M_{ij}^{(2)}(\mathbf{q}_\perp) = & \frac{ik}{2\pi} \sum_{M_s, M'_s} \int d\mathbf{c}_\perp d\mathbf{R}_A \exp(i\mathbf{q}_\perp \mathbf{c}_\perp) \delta(\mathbf{R}_A) \\ & \times \left\{ \langle \Psi_{\lambda/LS}^{JM_J} | \Omega_1 \Omega_2 + \Omega_1 \Omega_3 + \Omega_2 \Omega_3 | \Psi_{\lambda/LS}^{JM'_J} \rangle \right\}. \end{aligned} \quad (2.30)$$

$$M_{if}^{(3)}(\mathbf{q}_\perp) = \frac{ik}{2\pi} \sum_{M_s M_s'} \int d\mathbf{c}_\perp d\mathbf{R}_A \exp(i\mathbf{q}_\perp \cdot \mathbf{c}_\perp) \delta(\mathbf{R}_A) \times \left\langle \left\langle \Psi_{\lambda L S}^{JM_f} \left| \Omega_1 \Omega_2 \Omega_3 \right| \Psi_{\lambda L S}^{JM_f} \right\rangle \right\rangle. \quad (2.31)$$

Here  $M_{if}^{(1)}(\mathbf{q}_\perp)$ ,  $M_{if}^{(2)}(\mathbf{q}_\perp)$ ,  $M_{if}^{(3)}(\mathbf{q}_\perp)$  are the partial amplitudes of the single-, double-, and triple-collisions. The designation of subscripts 1, 2, and 3 is given in the explication to Eq. (1.1).

Figure 21a displays the partial DCSs for  $p^6\text{He}$  scattering ( $\Omega_1 = \Omega_\alpha$ ,  $\Omega_2 = \Omega_{n1}$ ,  $\Omega_3 = \Omega_{n2}$ ), in which the first (curve 1), second (curve 2), and third (curve 3) terms of Eq. (2.28) are taken into account separately, as well as their sum with consideration for interference (curve 4). It is seen from the figure that the main contribution at small scattering angles ( $\theta < 20^\circ$ ) is due to collisions with the  $\alpha$  cluster and two valence neutrons; however, their amplitude rapidly drops and higher-order multiple collisions start dominating with the increasing of the scattering-angle. It is also seen that at small scattering angles curve 1 lies above total curve 4, because in series (2.28) the double scattering term is subtracted from the single scattering one and the total cross section decreases, which improves the agreement with experiment. At the point where the curves of the single and double cross sections intersect, there is a minimum in total curve 4 arising due to the destructive interference upon squaring the matrix elements in (2.28). After the interferential minimum, the double collisions begin dominating and, at  $\theta \approx 50^\circ$ , the triple collisions are nearing them. Expansion (2.28) provides a convenient approach to finding the significance of terms of the single and higher-order scatterings. It is seen from the figure that, for the correct description of the DCS in the wide angular range (to  $\theta \sim 50^\circ - 60^\circ$ ), it is necessary to take into account the contributions from higher-order multiple collisions. This conclusion is also confirmed in a number of other works [67, 91, 173], in which the contribution to the cross section from the higher order terms of the series of multiple scattering was analyzed with scattering of protons by the  $^6\text{He}$ ,  $^{11}\text{Li}$ , and  $^{11}\text{Be}$  nuclei in inverse kinematics. Let us dwell upon [67]. Here the DCSs were calculated in three approximations: FIA (Factorized Impulse Approximation), FSA (Fixed Scatter Approximation), and Glauber approximation, and all of them proved to be very close. The differential cross section of single scattering from this work in Glauber approximation is shown by curve 5. It is calculated only to  $\theta \sim 18^\circ$  and does not reach the region of minimum; however, it is seen that as the scattering angle increases, the discrepancy from the experimental data grows. The consideration of higher-order multiple scattering reduces the DCS, bringing it closer to experimental data, which is seen both from our calculations (curve 4) and from [67] (DCS from this work

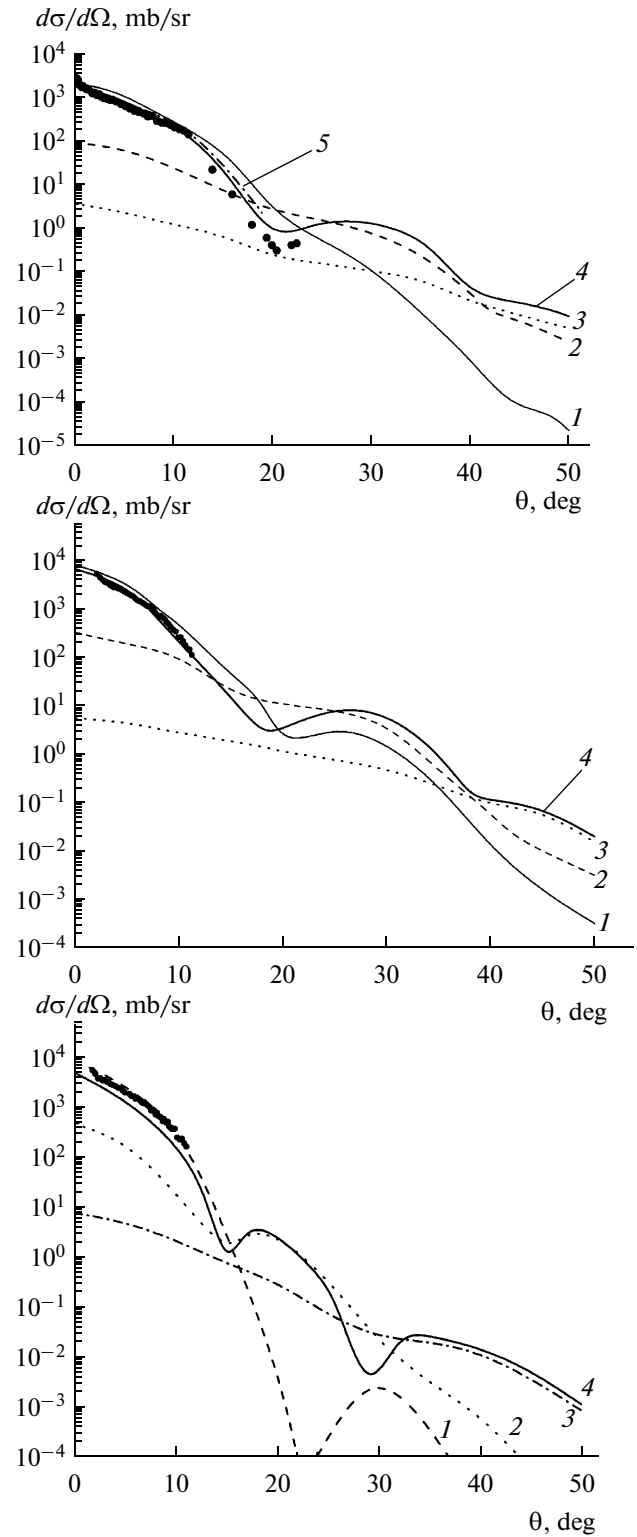


**Fig. 21.** Contribution to DCS from different multiplicities of scattering in operator  $\Omega$ . Curves 1, 2, 3, and 4 display the contributions from single-, double-, triple scatterings and their total contribution with allowance for interference. In panel a, the  $p^6\text{He}$  scattering is presented at  $E = 0.717$  GeV/nucleon; in panel b, the  $p^8\text{Li}$  scattering at  $E = 0.7$  GeV/nucleon is shown; in panel c, the  $p^9\text{Li}$  scattering at  $E = 0.7$  GeV/nucleon is illustrated.

taking into account all multiplicities of scattering is given in Fig. 10b, curve 5).

In Fig. 21b, the contribution from different multiplicities of scattering is calculated for  $p^8\text{Li}$  scattering ( $\Omega_1 = \Omega_\alpha$ ,  $\Omega_2 = \Omega_t$ ,  $\Omega_3 = \Omega_n$ ). Lines 1, 2, and 3 display the contribution separately from the first, second, and third terms of Eq. (2.28), and we see the result almost analogous to the previous, with the single difference that the cross section of single scattering has a small minimum in the region with  $\theta \sim 18^\circ$ .

A spectacular picture of the contribution from collisions of different multiplicities is observed in  $p^9\text{Li}$  scattering in Fig. 21c at  $E = 0.703$  GeV/nucleon for the WF in the  $\alpha-t-2n$  model. It is seen from the figure that at small scattering angles  $\theta < 14^\circ$ , the main contribution comes from single scattering by the  $\alpha$ ,  $t$ , and  $2n$  clusters (curve 1). It rapidly falls at large angles and in the region of  $30^\circ > \theta > 15^\circ$ , the terms of double scattering dominate (curve 2), at the angles  $\theta > 30^\circ$  the contribution comes from triple scattering (curve 3). Curve 4 presents the total contribution (the same as curve 1 in Fig. 18b). In the regions where the curves intersect, minima are observed in the total cross section, which are caused by interference of the scattering with different orders of collisions. In the regions of minima ( $\theta \approx 14^\circ$  and  $30^\circ$ ), another peculiarity is observed: the first minimum in both figures could be deeper if the triple scattering was not taken into account, the second minimum is not very deep due to the single scattering, which fills it partially.

Let us note that in all cases, the cross section of single scattering exceeds the experimental data in the small-angle region, the contribution from the double scattering decreases the DCS at small angles and after the first interferential minimum becomes dominating, after the second minimum the triple scattering begins to dominate. From the considered examples we can conclude that, for scattering by all investigated nuclei at high transferred momenta, the dynamic contributions from higher orders are substantial and must be taken into consideration.

**2.2.4. The differential cross section in optical limit (limit of single scattering).** Many formalisms (HEA, FIA, FSA, etc.) are restricted by single collisions only. As it was shown in the previous subsection, this is not always the justified approximation. For example, the following is said in [178] about it: “the formula of optical limit does not take into account the multiple scattering terms and it is the main reason, why.. the optical limit approximation overestimates the cross section of reactions”.

Since the single-collision operator is a sum of operators, acting at each structure constituents of the nucleus (see Eq. (2.29)) not mixing them (as in collisions of higher orders), this allows one to calculate the contribution to the DCS from each of them. One of the operator component acts on the core ( $\Omega_1 = \Omega_\alpha$  for

${}^6\text{He}$ ,  $\Omega_1 + \Omega_2 = \Omega_\alpha + \Omega_t$  for  ${}^8\text{Li}$ ,  $\Omega_1 = \Omega_{7\text{Li}}$  for  ${}^9\text{Li}$ ), another, the valence component, acts on neutrons ( $\Omega_2 + \Omega_3 = \Omega_{n1} + \Omega_{n2}$  for  ${}^6\text{He}$  and  ${}^9\text{Li}$ ,  $\Omega_3 = \Omega_n$  for  ${}^8\text{Li}$ ). Thus, the single scattering contains essential information on the structure of both the core and the skin.

A cross section of single scattering can be written as

$$\frac{d\sigma}{d\Omega} = \frac{1}{2J+1} \left| M_{ij}^{(1)}(\Omega_1) + M_{ij}^{(1)}(\Omega_2) + M_{ij}^{(1)}(\Omega_3) \right|^2, \quad (2.32)$$

where

$$M_{ij}^{(1)}(\Omega_n) = \frac{ik}{2\pi} \sum_{M_s, M_s'} \int d\mathbf{c}_\perp d\mathbf{R}_A \exp(i\mathbf{q}_\perp \mathbf{c}_\perp) \delta(\mathbf{R}_A) \times \left\langle \Psi_{\lambda_1 L_1}^{J M_1} \left| \Omega_n \right| \Psi_{\lambda_2 L_2}^{J M_2} \right\rangle, \quad (2.33)$$

index  $n = 1, 2, 3$ .

The result of such a calculation is shown for  $p^6\text{He}$  scattering at  $E = 0.717$  GeV/nucleon is shown in Fig. 22a. Curve 2 displays scattering by  $\alpha$ -particle, corresponding to consideration of the first term in Eq. (2.32), curve 3 presents scattering by two valence nucleons, corresponding to consideration of the second and third terms in Eq. (2.32), curve 1 gives the contribution from all terms in Eq. (2.32) (the same as curve 1 in Fig. 21a). It is seen from the figure that for all scattering angles the main contribution to the cross section comes from scattering by  $\alpha$ -particle; scattering by nucleons makes a certain contribution in the region of forward scattering angles (which in the coordinate space corresponds to the WF asymptotics). It is clear that the excess neutrons are localized in the surface region, therefore, their contribution to DCS is noticeable at small angles, but already at  $\theta > 10^\circ$  the DCS of scattering by nucleons becomes one order of magnitude smaller than the DCS of scattering by the core and then it rapidly drops, so that scattering for large angles is completely determined by the core. At zero angle ( $\theta = 0^\circ$ ), according to the optical theorem, the cross section is determined by the imaginary part of the amplitude at zero, which is directly connected with the total cross section  $\sigma_{tot}$  in the elementary amplitude of  $pn$  and  $p\alpha$  scattering; for  $E = 0.7$  GeV,  $\sigma^{pn} = 3.92$  fm<sup>2</sup> [179],  $\sigma^{p\alpha} = 12.5$  fm<sup>2</sup> [158], the first one is three times smaller than the second one; therefore, at zero angle the DCS of scattering by  $\alpha$ -particle is higher than that by neutrons.

Calculating the total cross section of  $p^6\text{He}$  scattering at the same energy by the optical theorem:

$$\sigma = \frac{4\pi}{k} \text{Im}(M_{ij}(0)), \quad (2.34)$$

we obtained  $\sigma = 17.8$  fm<sup>2</sup>. This value is somewhat larger than in [112], where the calculation of the cross section is performed with three Faddeev WFs which yielded  $\sigma = 15.3\text{--}16.1$  fm<sup>2</sup> depending on the radius of

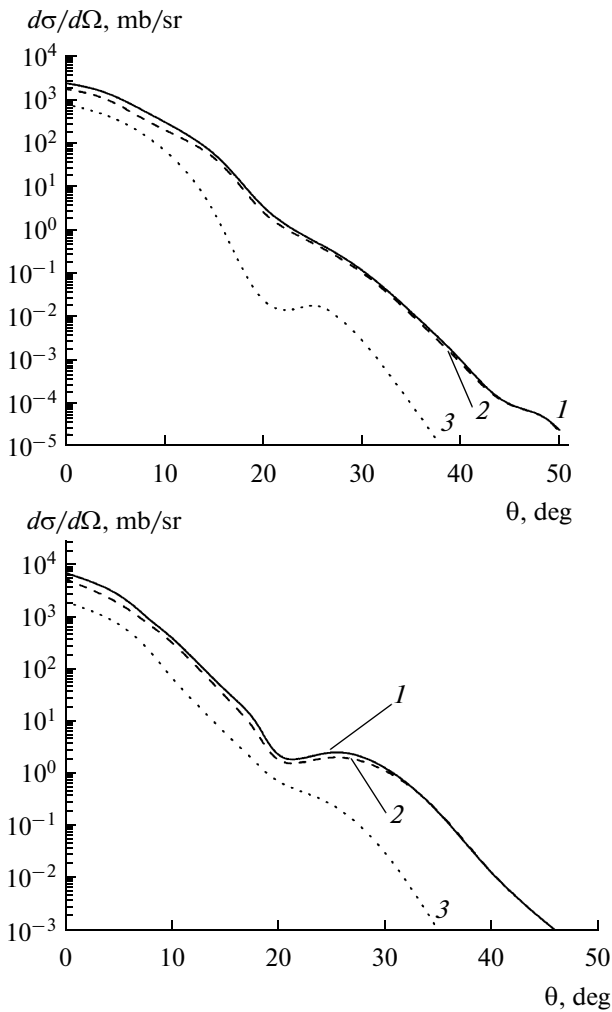


**Fig. 22.** Contribution to DCS of the single scattering (curve 1, the same as curve 1 in Fig. 21a) from scattering by the core, corresponding to the consideration of the first term in (2.32) (curve 2), and from scattering by the skin, corresponding to the consideration for the second and third terms in (2.32) (curve 3). In panels, there are presented (a) the  $p^6\text{He}$  scattering at  $E = 0.717$  GeV/nucleon; (b) the  $p^8\text{Li}$  scattering at  $E = 0.70$  GeV/nucleon.

$^6\text{He}$ , which is varied from 2.33 to 2.77 fm. The cross section of the reaction at this energy is calculated in [65]: in the optical limit approximation (OLA)  $\sigma = 16.6$  fm $^2$ , using the variational Monte Carlo method  $\sigma = 16.3$  fm $^2$  ( $R_m = 2.56$  fm), and using Green's function Monte Carlo method  $\sigma = 17.2$  fm $^2$  ( $R_m = 2.61$  fm), the latter value is most close to ours. The calculation with WF in the simple shell model also yields close values of the cross section:  $\sigma = 16.0$  fm $^2$  ( $R_m = 2.3$  fm) and  $\sigma = 16.3$  fm $^2$  ( $R_m = 2.6$  fm).

The total cross section of  $p^9\text{Li}$  scattering calculated by Eq. (2.34) at  $E = 0.065$  GeV/nucleon results in the value  $\sigma = 25.8$  fm $^2$ . Comparing it with the values, obtained in [173],  $\sigma = 28.8$  fm $^2$  (in the  $g$ -folding model with effective interaction, including the cen-

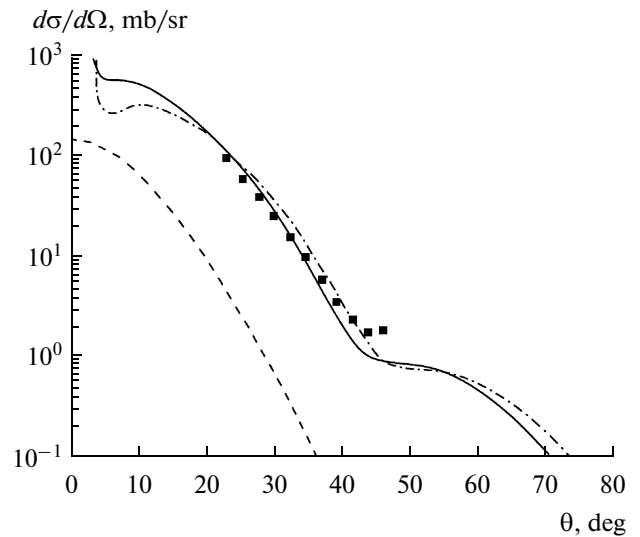


**Fig. 23.** Contribution to DCS of the  $p^{11}\text{Li}$  elastic scattering [22]. The dash-dotted curve corresponds to the scattering by the core, the dashed curve illustrates the scattering by halo nucleons, the solid curve displays the total contribution. The experimental data are taken from [165].

tral, two-body spin-orbit and tensor forces) and  $\sigma = 38.8$  fm $^2$  (in the  $t$ -folding model), we see that our value is smaller; however it is close to the value  $\sigma = 26.3$  fm $^2$ , obtained in [180] in the Born approximation.

The pattern, similar to  $p^6\text{He}$  scattering in Fig. 22a, is also observed for the DCS of  $p^8\text{Li}$  single scattering in Fig. 22b. Here, curve 2 presents the total scattering by  $\alpha$  and  $t$  (contribution from two first terms of Eq. (2.32)), curve 3 displays the scattering by nucleon (contribution of the last term of Eq. (2.32)), curve 1 is the sum of all three terms of Eq. (2.32) (the same as curve 1 in Fig. 21b). The scattering by the core dominates even more in the entire angular range and has the more complicated structure with a small minimum at  $\theta = 20^\circ$ , whereas scattering by a single nucleon has the form of monotonously decreasing function, which already at  $\theta = 30^\circ$  is smaller by almost two orders of magnitude than the cross section of scattering by the core.

In [107], while discussing different mechanisms of reactions with halo nuclei and the issues on the information which can be extracted from the measured characteristics, the authors conclude that the core size plays a more important role than halo in the DCS description. This statement also can be found in other works, in which the role of the core and valence neutrons in description of observables is analyzed [22, 87, 94, 177].

Figure 23 presents the calculation of angular distribution of elastic scattering by proton of  $^{11}\text{Li}$  nucleus from [22]. The DCSs for scattering on two parts of optical potential  $U_{core}$  and  $U_{halo}$  are shown by dash-dotted and dashed curves, the solid curve displays their total contribution. It is seen from the figure that scat-

tering by nucleons of the core dominates at all angles. Scattering on the neutron halo makes a small contribution only at small angles; “therefore, for studying the spatial structure of nuclei with halo, it is important to measure the differential cross section of scattering of protons at small transfer of momenta” [22].

## CONCLUSIONS

Significant progress in studying exotic neutron- and proton-excess nuclei has been achieved for the recent decade. Accelerators with new radioactive beams (not only light but also isotopes of heavy nuclei) have been commissioned, technologies of the polarized targets construction are used and polarization characteristics are measured. The kinematically complete experiments are conducted for two- and three-body breakup of the neutron-excess nuclei and for study of different correlations in motion of fragments. The laser-spectroscopic measurements made it possible to determine most accurately the rms charge radii of light nuclei. The experimental achievements stimulate theoretical studies in this field.

A description of the nuclear structure the nuclear density is seldom used (because it is impossible to calculate with them the effects of nuclear correlations); more often WFs are employed, which are calculated in the many-body (three-, four-, five-body) models. The earlier models are improved: the shell model with large basis (LSSM), and the shell model for continuous spectrum (SMEC). The comparison of characteristics, calculated on the basis of few-body and Faddeev WFs is conducted.

Methods of calculations are modified and improved. For example, the Monte Carlo calculations of Glauber amplitude of multiple scattering are conducted, in which the WFs of any intricacy can be used and there is no need for truncating the operator of multiple scattering [64]. The  $NN$  and  $N$ -cluster potentials are improved, in particular; the complete consideration for spin-orbit interactions the elementary amplitude directly from the phase shift analysis is already performed for  $pd$  scattering [98]. For energies of hundreds MeV/nucleon, the calculations are carried out in the relativistic impulse approximation (RIA) [76]. The modern computing codes FRESCO, DWUCK4 are used.

In addition to complication of calculations, another tendency takes place: the development of qualitative methods, the optical limit approximation, eikonal approximation, FIA, FSA, reducing the number of fitting parameters (as in works by Lukianov, where only two parameters of the potential can be used in HEA for quantitative description of experimental cross section). As is said in [22]: “Under certain physical conditions, the simplification of the reaction mechanism occurs, which makes it possible to develop

realistic models for description of processes of nucleus–nucleus collisions.”

At present, more and more works appear, in which the complex study takes place, along with elastic and inelastic scattering the additional channels of reaction: breakup, excitation, dynamic polarization of the core, etc. The simultaneous analysis of different observables within one theory shows that they are sensitive to different details of the interaction mechanism and the structure of the nucleus and their global description allows one to reduce the uncertainties connected with approximations of the applied formalism.

The review presents the calculation of characteristics of elastic  $p^6\text{He}$ ,  $p^8\text{Li}$ ,  $p^9\text{Li}$ , and  $p^9\text{C}$  scatterings within Glauber multiple-scattering diffraction theory. The essential feature of the calculation is that we used realistic three-body WFs, calculated in the context of modern nuclear models. From the particular calculations, the relation of the DCS and  $A_y$ , with the structure of the investigated nuclei and with the scattering mechanism, is found.

Analyzing the DCSs, calculated with the different model WFs (both in Glauber approximation and in comparison with other formalisms), we showed that a DCS weakly depends on the WF behavior on asymptotics (which corresponds to small transferred momenta, i.e., scattering with small angles), and dependence on the inner part of WF (which corresponds to large transferred momenta, i.e., scattering with large angles) is much stronger. This conclusion is confirmed by the calculation of the contribution from different components to the cross section of single scattering. Separating it depending on scattering by the core and by the skin, we demonstrated that the DCS of elastic scattering by the  $^6\text{He}$ ,  $^{8,9}\text{Li}$  neutron-excess nuclei in the entire angular range is determined mainly by scattering by the core. Scattering by neutrons located on the periphery makes a small contribution to the cross section only at small scattering angles, because the low-density skin cannot deflect the particle by a large angle. As is said in [177], “at large angles, the contribution from the core dominates. The described tendency confirms that the large transfer of momenta in scattering occurs during the interaction with the more massive  $\alpha$ -core.”

After an expansion of the Glauber operator of multiple scattering into a series of scattering on nucleons and clusters involved in the nuclear structure, we calculated the DCS while taking into account all multiplicities of collisions and partial (single-, double- and triple) cross sections and showed that, though the main contribution to the DCS at small transferred momenta comes from single collisions, at large transferred momenta the dynamic contributions from higher orders are considerable and must be taken into account.

The relation is found between the observed quantities and intercluster potentials, in which the WFs of

nuclei are calculated, and conclusions are drawn on the question of which potentials reproduce all experimental data most realistically. It is shown that the deep attractive potentials with FSs more reliably describe the nuclear structure than the oscillator potential does. By calculating the DCS of elastic scattering of protons with the WFs, presented in the same models but with different potentials of intercluster interactions:  $\alpha-t$ ,  $\alpha-n$  and  $t-n$  for  ${}^8\text{Li}$  and  ${}^7\text{Li}-n$ ,  $n-n$  for  ${}^9\text{Li}$ , we have shown that cross sections are less sensitive to variations of the intercluster interactions than to the WFs, constructed in different models. For example, the WF of the  ${}^9\text{Li}$  nucleus in the  $\alpha-t-2n$  model is less successful than the WF in the  ${}^7\text{Li}-n-n$  model for describing the DCS at all energies, which may be the consequence of the inadequate cluster separation. Too rapid (as compared with experiment) decrease of the DCS with the WF in the  $\alpha-t-2n$  model at large transferred momenta is evidence of the deficit of the WF high-momentum components.

The consideration for tensor interaction in the intercluster potentials results in the mixing of configurations and occurrence of additional WF components with different quantum numbers. The contribution of small components of WF, connected with consideration for tensor interaction in the intercluster potentials, allows one to correctly describe the quadrupole and magnetic moments of nuclei and improve the DCS description. Thus, the addition of the tensor interaction to the  $\alpha-t$  (or to  $n-t$ ) alone, potential allows one to calculate the WF of  ${}^8\text{Li}$ , in which the total weight of configurations with  $LS = 21$  increases to 10% which brings into agreement the quadrupole and magnetic moments with experimental values. With the  ${}^7\text{Li}-n$  potential, which has the strong spin dependence, the WF is calculated, which reproduces the quadrupole moment of  ${}^9\text{Li}$ . There is a correlation between the filling of the DCS minimum and the contribution from the WF small components:  $\lambda/LS = 1121; 3121$  for  ${}^8\text{Li}$  and  $\lambda/LS = 1113/2 \ 1111/2$  for  ${}^9\text{Li}$ . The calculation has shown for  $p$ - ${}^6\text{He}$  scattering that  $P$ -wave in the WF of  ${}^6\text{He}$  (with a weight of 4.3%) makes the appreciable contribution to the cross section at the angles  $\theta > 45^\circ$ .

From the calculation of polarization characteristics, it is possible to draw the general conclusion that they are substantially stronger (than the DCS and the total cross section), depending on the selection of both the WF of the target-nucleus and parameters of the spin-orbit nucleon-nucleon interaction; however, in the region of small scattering angles they like the DCS, they depend weakly on the selection of the model WFs of the nucleus.

The comparison with results of calculations, performed in the other approximations (HEA, optical model, FIA, FSA) and with different model WFs, has demonstrated a good accuracy of the Glauber approx-

imation and noncontradictory description of experimental data. This assigns the confidence that the description of experimental data to be obtained in the future can be carried out within the approved Glauber formalism.

## ACKNOWLEDGMENTS

We thank N.S. Zelenskaya and V.K. Lukianov for valuable consultations during the discussion of results.

The work was partially supported by the grant FI 12.2/09 of the Ministry for Education and Science of the Republic of Kazakhstan.

## REFERENCES

1. I. Tanihata et al., Phys. Rev. Lett. **55**, 2676 (1985).
2. I. Tanihata et al., Phys. Lett. B **160**, 380 (1985).
3. I. Tanihata et al., Phys. Lett. B **206**, 582 (1988).
4. I. Tanihata et al., Phys. Lett. B **289**, 261 (1992).
5. *Technical Proposal for the Design, Construction, Commissioning and Operation of the ELISE Setup*, Spokesperson Haik Simon, GSI Internal Report (GSI, Dec. 2005); Acta Phys. Polon. B **41**, 229–536 (2009); www.fair.gsi.de
6. T. Suda and M. Wakasugi, Prog. Part. Nucl. Phys. **55**, 1417 (2005).
7. Memorandum to Members of the National Science Board, Arden, Bement, NSB-2006-71, July 10, 2006. www.nsl.msu.edu
8. I. Slaus, Nucl. Phys. A **790**, 199 (2007). www.ganil-spiral2.eu
9. T. Baumann, A. M. Amthor, and D. Bazin, Nature **449**, 1022 (2007).
10. S. K. Patra and R. N. Panda, nucl-th/0906.3797.
11. O. M. Knyaz'kov, I. N. Kukhtina, and S. A. Fayans, Phys. Part. Nucl. **30**, 369 (1999).
12. A. Ozawa, T. Suzuki, and I. Tanihata, Nucl. Phys. A **693**, 32 (2001).
13. R. Kolpakchieva, Yu. É. Peniozhkevich, and Kh. G. Bolen, Phys. Part. Nucl. **29**, 341 (1998).
14. R. Kolpakchieva, Yu. É. Peniozhkevich, and Kh. G. Bolen, Phys. Part. Nucl. **30**, 627 (1999).
15. R. Kolpakchieva and Yu. É. Peniozhkevich, Phys. Part. Nucl. **33**, 629 (2002).
16. S. K. Patra et al., Phys. Rev. C **80**, 064602 (2009).
17. G. Audi et al., Nucl. Phys. A **729**, 337 (2003).
18. G. Ewald et al., Phys. Rev. Lett. **93**, 113002 (2004).
19. P. Moller et al., Phys. Rev. Lett. **99**, 252501 (2007).
20. R. Sanches et al., Phys. Rev. Lett. **96**, 033002 (2006).
21. C. W. de Jager et al., At. Data Nucl. Data Tables **14**, 479 (1974).
22. S. N. Ershov and B. V. Danilin, Phys. Part. Nucl. **39**, 835 (2008).
23. M. Goeppert-Mayer and J. Jensen, *Elementary Theory of Nuclear Shell Structure* (Wiley, New York, 1955; Inostr. Liter., Moscow, 1958).
24. P. Navratil and B. R. Barrett, Phys. Rev. C **54**, 2986 (1996); Phys. Rev. C **57**, 3119 (1998).

25. S. Karataglidis et al., Phys. Rev. C **55**, 2826 (1997).
26. S. Karataglidis et al., Phys. Rev. C **61**, 024319 (2000).
27. P. Navratil and W. E. Ormand, Phys. Rev. Lett. **88**, 152502 (2002).
28. M. V. Zhukov et al., Phys. Rep. **231**, 151 (1993).
29. M. V. Zhukov et al., Phys. Rev. C **50**, R1 (1994).
30. A. A. Korshennikov et al., Nucl. Phys. A **616**, 189 (1997).
31. A. A. Korshennikov et al., Nucl. Phys. A **617**, 45 (1997).
32. V. G. Neudatchin and Yu. F. Smirnov, *Nucleon Clusters in Light Nuclei* (Nauka, Moscow, 1969) [in Russian].
33. N. F. Golovanova, I. M. Ill'in, V. G. Neudatchin, et al., Nucl. Phys. A **262**, 444 (1976).
34. N. F. Golovanova, V. G. Neudatchin, and E. T. Ibraeva, Progr. Theor. Phys. **59**, 127 (1978).
35. M. A. Zhusupov and Yu. N. Uzikov, Sov. J. Part. Nucl. **18**, 136 (1987).
36. Y. Kanada-En'yo, H. Horiuchi, and A. Ono, Phys. Rev. C **52**, 628 (1995).
37. H. Horiuchi and Y. Kanada-En'yo, Nucl. Phys. A **616**, 394 (1997).
38. Y. Kanada-En'yo, Y. Taniguchi, and M. Kimura, Nucl. Phys. A **805**, 392 (2008).
39. S. Saito, Progr. Theor. Phys. Suppl. **62**, 11 (1977).
40. K. Arai, Y. Suzuki, and K. Varga, Phys. Rev. C **51**, 2488 (1995).
41. H. Kanada, T. Kaneko, and Y. C. Tang, Phys. Rev. C **34**, 107 (1996).
42. R. S. Mackintosh and S. G. Cooper, Nucl. Phys. A **589**, 377 (1995).
43. V. S. Vasilevskii et al., Sci. Papers Inst. Nucl. Res., No. 2 (8), 512 (2002).
44. Yu. A. Lashko and G. F. Filippov, Nucl. Phys. A **806**, 124 (2008); Nucl. Phys. A **826**, 24 (2009).
45. D. Baye, Y. Suzuki, and P. Descouvemont, Progr. Theor. Phys. **91**, 271 (1994).
46. V. I. Kukulin and V. M. Krasnopolsky, Sov. J. Nucl. Phys. **22**, 578 (1975).
47. V. I. Kukulin and V. M. Krasnopolsky, J. Phys. G **34**, 795 (1977).
48. K. Varga and Y. Suzuki, Phys. Rev. C **52**, 1598 (1995).
49. K. Varga, Y. Suzuki, and I. Tanihata, Phys. Rev. C **52**, 3013 (1995); Nucl. Phys. A **588**, 157 (1995).
50. Y. Suzuki, K. Varga, and J. Ushikara, Nucl. Phys. A **631**, 91 (1998).
51. K. Varga, Y. Suzuki, and R. G. Lovas, Phys. Rev. C **66**, 041302(R) (2002).
52. Y. Suzuki, R. G. Lovas, and K. Varga, Progr. Theor. Phys. Suppl. **146**, 413 (2002).
53. A. N. Boyarkina, *Structure of Nuclei with Ir-Shell* (Mosc. Gos. Univ., Moscow, 1973) [in Russian].
54. V. I. Kukulin, V. G. Neudachin, and V. N. Pomerantsev, Sov. J. Nucl. Phys. **24**, 155 (1976).
55. V. G. Neudachin, B. G. Struzhko, and V. M. Lebedev, Phys. Part. Nucl. **36**, 468 (2005).
56. E. V. Inopin, V. S. Kinchakov, V. K. Lukyanov, and Yu. S. Pol', Sov. J. Nucl. Phys. **19**, 507 (1974).
57. E. V. Inopin, V. S. Kinchakov, V. K. Lukyanov, and Yu. S. Pol', Izv. AN SSSR, Ser. Fiz. **39**, 55 (1975).
58. E. V. Inopin, V. S. Kinchakov, V. K. Lukyanov, and Yu. S. Pol', Ann. Phys. **118**, 307 (1979).
59. Yu. A. Berezhnoy et al., J. Phys. G **10**, 63 (1984).
60. Yu. A. Berezhnoy and V. P. Mikhailyuk, Phys. At. Nucl. **67**, 1448 (2004).
61. Yu. A. Berezhnoy and V. P. Mikhailyuk, Phys. Part. Nucl. **39**, 221 (2008).
62. K. A. Gridnev and S. Yu. Torilov, Phys. At. Nucl. **69**, 1204 (2006); Int. Mod. Phys. E **14**, 635 (2005).
63. B. S. Pudliner et al., Phys. Rev. C **56**, 1720 (1997).
64. S. C. Pieper, K. Varga, and R. B. Wiringa, Phys. Rev. C **66**, 044310 (2002).
65. K. Varga, S. C. Pieper, Y. Suzuki, and R. B. Wiringa, Phys. Rev. C **66**, 034611 (2002).
66. S. C. Pieper, nucl-th/0410115.
67. S. Al-Khalili, R. Crespo, R. C. Johnson, et al., Phys. Rev. C **75**, 024608 (2007).
68. V. I. Kukulin, V. M. Krasnopolski, V. T. Voronchev et al., Nucl. Phys. A **453**, 365 (1986).
69. V. I. Kukulin, V. T. Voronchev, T. D. Kaipov, and R. A. Eramzhyan, Nucl. Phys. A **517**, 221 (1990).
70. G. G. Ryzhikh, R. A. Eramzhyan, V. I. Kukulin, and Yu. M. Tchuvil'sky, Nucl. Phys. A **563**, 247 (1993).
71. V. I. Kukulin, V. N. Pomerantsev, and Kh. D. Rasikov, Nucl. Phys. A **586**, 151 (1995).
72. V. T. Voronchev, V. I. Kukulin, and V. N. Pomerantsev, Few-Body Syst. **18**, 191 (1995).
73. R. A. Eramzhyan, G. G. Ryzhikh, and Yu. M. Tchuvil'sky, Phys. At. Nucl. **62**, 37 (1999).
74. S. Ritt et al., Phys. Rev. C **43**, 745 (1991); Phys. Rev. C **49**, 3117 (1994).
75. Y. Sakuragi et al., Progr. Theor. Phys. **70**, 1047 (1983).
76. E. Baldini-Neto et al., nucl-th/0212010.
77. E. V. Zemlyanaya, V. K. Lukyanov, K. V. Lukyanov, et al., Izv. RAN, Ser. Fiz. **69**, 1649 (2005).
78. A. N. Antonov, V. K. Lukyanov, et al., Phys. Rev. C **72**, 044307 (2005).
79. V. K. Lukyanov, Phys. At. Nucl. **69**, 1033 (2006).
80. K. V. Lukyanov, E. V. Zemlyanaya, and V. K. Lukyanov, Phys. At. Nucl. **69**, 240 (2006).
81. K. V. Lukyanov, V. K. Lukyanov, E. V. Zemlyanaya, et al., Eur. Phys. J. A **33**, 389 (2007).
82. K. V. Lukyanov, E. V. Zemlyanaya, V. K. Lukyanov, et al., Izv. RAN, Ser. Fiz. **72**, 903 (2008).
83. V. K. Lukyanov, E. V. Zemlyanaya, K. V. Lukyanov, et al., Phys. Rev. C **80**, 024609 (2009).
84. P. Roussel-Chomas et al., Nucl. Phys. A **477**, 345 (1988).
85. S. P. Weppner et al., nucl-th/0001029v1.
86. S. Karataglidis, Y. J. Kim, and K. Amos, Nucl. Phys. A **793**, 40 (2007).
87. D. Gupta, C. Samanta, and R. Kanungo, Nucl. Phys. A **674**, 77 (2000).
88. R. J. Glauber, *Lectures in Theoretical Physics* (Interscience, New York, 1959), p. 315.
89. A. G. Sitenko Ukr. Fiz. Zh. **4**, 152 (1959).

90. R. Crespo, A. M. Moro, and I. J. Thompson, *Phys. At. Nucl.* **69**, 1254 (2006).
91. R. Crespo and R. C. Johnson, *Phys. Rev. C* **60**, 034007 (1999).
92. G. Bertsch et al., *Nucl. Phys. A* **284**, 399 (1977).
93. J.-P. Jeukenne, A. Lejeune, and C. Mahaux, *Phys. Rev. C* **16**, 80 (1977).
94. W. Mitting and P. Roussel-Chomas, *Nucl. Phys. A* **693**, 495 (2001).
95. A. A. Korshennikov et al., *Phys. Rev. C* **53**, R537 (1996).
96. A. A. Andrianov, K. A. Gridnev, T. V. Tarutina, and M. A. Yulgaldin, *Izv. RAN, Ser. Fiz.* **62**, 89 (1998).
97. K. A. Gridnev and T. V. Tarutina, *Izv. RAN, Ser. Fiz.* **63**, 910 (1999).
98. M. N. Platonova and V. I. Kukulín, *Phys. Rev. C* **81**, 014004 (2010).
99. Ch. Elster et al., *Phys. Rev. C* **78**, 034002 (2008).
100. L. I. Galanina and N. S. Zelenskaya, *Phys. At. Nucl.* **70**, 283 (2007).
101. L. I. Galanina and N. S. Zelenskaya, *Phys. At. Nucl.* **72**, 1695 (2009).
102. L. D. Blokhintsev, A. V. Lado, and Yu. N. Uzikov, *Nucl. Phys. A* **597**, 487 (1996).
103. Yu. N. Uzikov et al., *Nucl. Phys. A* **644**, 321 (1998).
104. Yu. Ts. Oganessian and V. I. Zagrebaev, *Phys. Rev. Lett.* **82**, 4996 (1999).
105. Yu. Ts. Oganessian, V. I. Zagrebaev, and J. S. Vaagen, *Phys. Rev. C* **60**, 034007 (1999).
106. G. V. Ter-Akopian et al., *Phys. Lett. B* **426**, 251 (1998).
107. M. V. Zhukov, Yu. L. Parfenova, and J. Z. Vaagen, *Phys. At. Nucl.* **65**, 746 (2002).
108. S. I. Sidorchuk, R. Vol'ski, M. S. Golovkov, et al., *Izv. RAN, Ser. Fiz.* **74**, 473 (2010).
109. L. Giot et al., *Phys. Rev. C* **71**, 064311 (2005).
110. G. D. Alkhasov et al., *Phys. Rev. Lett.* **78**, 2313 (1997).
111. J. S. Al-Khalili, and J. A. Tostevin, *Phys. Rev. C* **57**, 1846 (1998).
112. J. A. Tostevin, J. S. Al-Khalili, J. M. Brooke, and J. A. Christley, *J. Phys. G* **24**, 1589 (1998).
113. B. Abu-Ibrahim, K. Fujimura, and Y. Suzuki, *Nucl. Phys. A* **657**, 391 (1999).
114. K. Arai et al., *Phys. Rev. C* **59**, 1432 (1999).
115. S. Sack, L. C. Biedenharn, and G. Breit, *Phys. Rev.* **93**, 321 (1954).
116. R. V. Reid, *Ann. Phys.* **50**, 411 (1968).
117. S. A. Bertulani and M. S. Hussein, *Phys. Rev. C* **76**, 051602(R) (2007).
118. I. Sick, *Phys. Lett. B* **116**, 212 (1982).
119. L.-B. Wang et al., *Phys. Rev. Lett.* **93**, 142501 (2004).
120. P. Mueller, I. A. Sulai, A. C. Villary et al., *Phys. Rev. Lett.* **99**, 252501 (2007).
121. S. B. Neumaier, G. D. Alkhasov, M. N. Andronenko et al., *Nucl. Phys. A* **712**, 247 (2002).
122. G. D. Alkhasov, A. V. Dobrovolsky, and A. A. Lobodenko, *Phys. At. Nucl.* **69**, 1124 (2006).
123. A. V. Dobrovolsky, G. D. Alkhasov, A. A. Lobodenko et al., *Nucl. Phys. A* **766**, 1 (2006).
124. F. Aksouh et al., in *Proceedings of the 10th International Conference on Nuclear Reaction Mechanisms, Varenna, 2003*, Ricerca. Sci. Educ. Permanente, No. 122 (Suppl.), 157 (2003).
125. B. V. Danilin, I. J. Thompson, M. V. Zhukov, et al., *Phys. At. Nucl.* **64**, 1215 (2001).
126. W. Horiuchi et al., *Phys. Rev. C* **76**, 024311 (2007).
127. D. R. Tilley et al., *Nucl. Phys. A* **708**, 3 (2002).
128. N. K. Timofeyuk and I. J. Thompson, *Phys. Rev. C* **61**, 044608 (2000).
129. M. A. Zhusupov and Sh. Sh. Sagindykov, *Izv. RAN, Ser. Fiz.* **65**, 714 (2001).
130. M. A. Zhusupov and Sh. Sh. Sagindykov, *Izv. RAN, Ser. Fiz.* **66**, 392 (2002).
131. A. Csoto, nucl-th/9908081.
132. M. A. Zhusupov, K. A. Zhusupova, and E. T. Ibraeva, *Phys. At. Nucl.* **63**, 170 (2000).
133. Y. Stowe and W. Zahn, *Nucl. Phys. A* **289**, 317 (1977).
134. S. A. Badalov and G. F. Filippov, *Sov. J. Nucl. Phys.* **43**, 45 (1986).
135. P. Descouvemont and D. Baye, *Nucl. Phys. A* **487**, 420 (1988).
136. A. Csoto, *Phys. Rev. C* **61**, 024311 (2000).
137. K. Bennaceur et al., *Nucl. Phys. A* **651**, 289 (1999).
138. L. V. Grigorenko et al., *Phys. Rev. C* **57**, 2099 (1998).
139. S. B. Dubovichenko and A. V. Dzhazairov-Kakhramanov, *Phys. At. Nucl.* **58**, 579 (1995).
140. S. B. Dubovichenko and A. V. Dzhazairov-Kakhramanov, *Phys. Part. Nucl.* **28**, 615 (1997).
141. B. Buck and A. C. Merchant, *J. Phys. G* **14**, L211 (1988).
142. N. A. Burkova and M. A. Zhusupov, *Phys. Lett. B* **223**, 136 (1989).
143. V. G. Neudachin and Yu. F. Smirnov, in *Modern Problems of Optics and Nuclear Physics* (Gos. Univ., Kiev, 1974), p. 225 [in Russian].
144. F. Ajzenberg-Selove, *Nucl. Phys. A* **490**, 1 (1988).
145. J. H. Kelley, J. L. Godwin, X. Hu, et al., "Energy Levels of Light Nuclei  $A = 8$ ," Preprint of Triangle Univ. (Triangle Univ., Durham, 2002).
146. T. Minamisono et al., *Phys. Rev. Lett.* **69**, 2058 (1992); K. Matsuta et al., *Nucl. Phys. A* **588**, 153 (1995).
147. M. A. Zhusupov, Sh. Sh. Sagindykov, and C. B. Sakhiev, *Izv. RAN, Ser. Fiz.* **70**, 240 (2006).
148. G. Ewald et al., *Phys. Rev. Lett.* **94**, 039901 (2005).
149. S. K. Sakhiev, Doctoral Dissertation in Physics and Mathematics (Almaty, 2008).
150. I. J. Thompson and M. V. Zhukov, *Phys. Rev. C* **49**, 1904 (1994).
151. R. Crespo, J. A. Tostevin, and I. J. Thompson, *Phys. Rev. C* **54**, 1867 (1996).
152. E. T. Ibraeva, M. A. Zhusupov, O. Imambekov, and Sh. Sh. Sagindykov, *Phys. At. Nucl.* **71**, 1272 (2008); *Izv. RAN, Ser. Fiz.* **72**, 1072 (2008).
153. M. A. Zhusupov, E. T. Ibraeva, A. Yu. Zaykin, and Sh. Sh. Sagindykov, *Phys. At. Nucl.* **72**, 1719 (2009).
154. A. V. Volkov, *Nucl. Phys.* **74**, 33 (1965).
155. A. Hasegawa and S. Nagata, *Progr. Theor. Phys.* **45**, 1786 (1971).

156. I. R. Afnan and Y. C. Tang, *Phys. Rev.* **175**, 1337 (1968).
157. D. R. Tilley et al., *Nucl. Phys. A* **745**, 155 (2004); D. R. Tilley et al., "Energy Levels of Light Nuclei  $A = 9$ ," Preprint of Triangle Univ. (Triangle Univ., Durham, 2001).
158. I. M. A. Tag Eldin et al., *J. Phys. G* **16**, 1051 (1990).
159. G. D. Alkhasov et al., *Phys. Lett. B* **85**, 43 (1979).
160. Yu. A. Berezhnoy et al., *Sov. J. Nucl. Phys.* **55**, 1044 (1992).
161. D. A. Varshalovich, A. N. Moskalev, and V. K. Khersonskii, *Quantum Theory of Angular Momentum* (Nauka, Leningrad, 1975; World Scientific, Singapore, 1988).
162. I. S. Gradshteyn and I. M. Ryzhik, *Tables of Integrals, Series and Products* (Academic, New York, 2000; Fizmatgiz, Moscow, 1962).
163. P. Osland and R. G. Glauber, *Nucl. Phys. A* **326**, 255 (1979).
164. A. A. Korshennikov et al., *Phys. Lett. B* **316**, 38 (1993).
165. C. B. Moon et al., *Phys. Lett. B* **297**, 39 (1992).
166. M. A. Zhusupov, E. T. Ibraeva, and A. Yu. Zaykin, *Izv. RAN, Ser. Fiz.* **69**, 714 (2005).
167. R. Crespo et al., *Phys. Rev. C* **76**, 054607 (2007).
168. J. J. Kelly, *Phys. Rev. C* **38**, 1490 (1988).
169. C. W. Glower et al., *Phys. Rev. C* **43**, 1664 (1991).
170. C. W. Glower et al., *Phys. Rev. C* **41**, 2487 (1990).
171. M. A. Zhusupov, E. T. Ibraeva, and O. Imambekov, *Phys. At. Nucl.* **68**, 131 (2005).
172. M. A. Zhusupov, E. T. Ibraeva, A. Yu. Zaykin, and Sh. Sh. Sagindykov, *Izv. RAN, Ser. Fiz.* **71**, 804 (2007); *Izv. RAN, Ser. Fiz.* **73**, 213 (2009).
173. P. J. Dortmans, K. Amos, S. Karataglidis, and J. Raynal, *Phys. Rev. C* **58**, 2249 (1998).
174. J. A. Carr, *Phys. Rev. C* **56**, 324 (1997).
175. R. Crespo, J. A. Tostevin, and R. C. Johnson, *Phys. Rev. C* **51**, 3283 (1995).
176. M. A. Zhusupov, A. Yu. Za@kin, E. T. Ibraeva, and Sh. Sh. Sagindykov, *Izv. RAN, Ser. Fiz.* **71**, 811 (2007).
177. R. Wolski, A. Pakou, and N. Alamanos, *Phys. At. Nucl.* **65**, 736 (2002).
178. G. D. Alkhazov and A. A. Lobodenko, *Phys. At. Nucl.* **70**, 93 (2007).
179. D. K. Hasell et al., *Phys. Rev. C* **34**, 236 (1986).
180. S. Herenzaki, H. Toki, and I. Tanihata, *Nucl. Phys. A* **552**, 57 (1993).

SPELL: 1. ok